MUONIUM KINETICS AND INTRAMOLECULAR MOTION OF MUONIUM-SUBSTITUTED FREE RADICALS

by

Dake Yu

B.Sc., Shandong University, Shandong, China, 1982
M.Sc., Shandong University, Shandong, China, 1985

THESIS SUBMITTED IN PARTIAL FULFILLMENT OF
THE REQUIREMENTS FOR THE DEGREE OF
DOCTOR OF PHILOSOPHY
in the Department
of
Chemistry

SIMON FRASER UNIVERSITY

December 1989

APPROVAL

Name: Dake Yu

Degree: DOCTOR OF PHILOSOPHY

Title of thesis: MUONIUM KINETICS AND INTRAMOLECULAR MOTION OF MUONIUM-SUBSTITUTED FREE RADICALS

Examining Committee:

Chair: Dr. F. W. B. Einstein

Dr. P. W. Percival
Senior Supervisor

Dr. T. N. Bell

Dr. R. G. Korteling

Dr. E. J. Wells
Internal Examiner

Dr. R. H. Schuler
External Examiner
Professor, Department of Chemistry
Director, Radiation Laboratory
University of Notre Dame

Date Approved: November 28, 1989

PARTIAL COPYRIGHT LICENSE

Title of Thesis/Project/Extended Essay

Muonium Kinetics and Intramolecular Motion of Muonium-Substituted

Free Radicals

Author: ______________________

(signature)

Dake Yu

(name)

December 13, 1989

(date)

ABSTRACT

Muonium is a single electron hydrogen-like atom with a positive muon as its nucleus. Its Bohr radius and ionization potential are virtually the same as ^1H but it has only one-ninth of the mass. The radioactive character of the positive muon enables one to study muonium reactions and muonated molecules by μSR (muon spin rotation) and μLCR (muon level-crossing resonance) techniques.

The rate constants k_M for reaction (1) Mu + NO_3^- (an activation controlled reaction) and (2) Mu + MnO_4^- (a diffusion controlled reaction) in aqueous solution were determined from the decay rates of the muonium signal as a function of pressure. The activation volumes were determined to be -7.1 cm^3/mol and 3.1 cm^3/mol for reactions (1) and (2), respectively. This is the first application of high pressure measurements in muonium chemistry.

Kinetic isotope effects were calculated for the reactions of H and Mu with H_2O_2 using semiempirical quantum chemistry methods, including approximate tunnelling corrections based on an Eckart potential. The calculations were carried out for two specific mechanisms: (1) the attack of Mu or H on O, and (2) the attack on H. The calculated values of k_M/k_H are 91.5 for (1) and 354 for (2).

μSR and μLCR techniques were used to study various alkyl and cyclohexadienyl radicals: CH_2CH_2Mu, $^{13}CH_2{}^{13}CH_2Mu$, CD_2CD_2Mu, $(CH_3)_2CCH_2Mu$, $(CH_3)_2{}^{13}CCH_2Mu$, C_6H_6Mu, $^{13}C_6H_6Mu$, C_6D_6Mu and C_6F_6Mu. The measurements of hyperfine coupling constants for these radicals covered a wide temperature range, including the gas, liquid and solid phases. By fitting the theoretical models to the experimental data, it was found that (1) At the minimum energy configuration Mu eclipses the p_z orbital of C_α in CH_2CH_2Mu. The rotation barrier between the staggered and eclipsed configuration is 3.1 kJ/mol; (2) The barriers for methyl rotation in $(CH_3)_2CCH_2Mu$ are 2.1 and 3.4 kJ/mol for liquid and solid phase, respectively; (3) The out-of-plane angle for $(CH_3)_2CCH_2Mu$ is 19^0 with an inversion barrier of 1.8 kJ/mol; (4) Cyclohexadienyl has a planar structure and the variation of hyperfine coupling constants with temperature are mainly due to the local motions within the methylene group; (5) Increased C-Mu bond length in muonium-substituted radicals provides the key role for the isotope shifts in hyperfine coupling constants.

To my family

ACKNOWLEDGMENTS

I wish to express my gratitude to Dr. P. W. Percival, my senior supervisor, for his continual encouragement and guidance during the course of this study.

I would like to thank the other members of my supervisory committee, Drs. T. N. Bell and R. G. Korteling for the time and attention they devoted me.

I am grateful for the expert technical assistance provided by Dr. J. C. Brodovitch and help from Ms. J. Bartlett, Mr. S. K. Leung and Mrs. S. Sun-Mack. I acknowledge C. Ballard, K. Hoyle and J. Worden for technical assistance.

To Drs. R. F. Kiefl, G. L. Malli, K. E. Newman, E. Roduner, E. J. Wells and the members of the SFU chemistry department and TRIUMF's μSR group, who were always available for help, I express appreciation.

The generous financial support from Simon Fraser University and Dr. P. W. Percival is gratefully acknowledged.

This work was performed during a leave of absence from Shandong University, Shandong, People's Republic of China.

TABLE OF CONTENTS

LIST OF TABLES

Table

LIST OF FIGURES

Figure

LIST OF ABBREVIATIONS

hf	hyperfine
hfcc	hyperfine coupling constant
HRR	harmonic rate ratio
INDO	intermediate neglect of differential overlap
KEK	National Laboratory of High Energy Physics
KIE	kinetic isotope effect
LCAO	linear combination of atomic orbitals
LF	longitudinal field
MINDO	modified intermediate neglect of differential overlap
PSI	Paul Scherrer Institute
QCPE	Quantum Chemistry Program Exchange
RAL	Rutherford Appleton Laboratory
SCF	self-consistent-field
SFU	Simon Fraser University
TRIUMF	Tri-University Meson Facility
TF	transverse field
TS	transition state
UBC	University of British Columbia
ZPE	zero point energy
μSR	muon spin rotation
μLCR	muon level-crossing resonance
1-D	one-dimension

CHAPTER ONE

Introduction

1.1. Muonium chemistry

The positive muon, μ^+ is an elementary particle with a mass equal to one ninth that of a proton and has the same spin and charge as a proton. It was first observed as a component of cosmic rays by Anderson and Neddermeyer in 1937 [1] and is now artificially produced with high energy (500-800 MeV) particle accelerators available at several places in the world (*e.g.* TRIUMF, Canada; PSI, Switzerland; KEK, Japan; RAL, England). The muon behaves in matter as if it were a very light proton, but its parity-violating decay [2] gives the experimenter easy access to the interaction of its spin. Some of the properties of μ^+ are summarized in table 1-1 [3].

It was in 1957 that Friedman and Telegdi proposed that the positive muon could form a bound state with an electron [4]. This one-electron atom was named muonium (Mu = μ^+e^-). In most gases, liquids and solids, the μ^+ captures an electron from the medium during the final stages of its thermalization process to form muonium [5,6,7]. Some of the properties of Mu are given in table 1-2 [3].

Table 1-1

Properties of positive muons [3]

Charge	+e	
Spin	$\frac{1}{2}$	
Mass	105.6595 MeV/c^2	= 206.76835 m_e
		= 0.1126096 m_p
		= 0.7570 m_{π^+}
Magnetic moment	4.49048 x 10^{-23} erg/G	
		= 3.1833452 μ_p
		= 0.004834 μ_e
g-factor	2.002331848	= 1.000006 g_e
Mean lifetime	2.19714 μs	
Gyromagnetic ratio	13.5534 kHz/G	

Table 1-2

Properties of muonium [3]

Mass	207.8 m_e
	= 0.1131 m_H
Reduced mass	0.9956 μ_H
First Bohr radius	0.5315 x 10^{-8} cm
	= 1.0044 a_0
First ionization potential	13.54 eV
	= 0.9956 I.P. of H
Thermal de Broglie wavelength (300K)	2.979 x 10^{-8} cm
	= 2.967 of H
Hyperfine frequency	2.8044 x 10^{10} rad/s
Mean thermal velocity (300K)	0.75 x 10^6 cm/s
	= 2.967 v_H

Although muonium has only one ninth the rest mass of a hydrogen atom, its reduced mass is 0.996 that of hydrogen, and consequently the Bohr radius and ionization potentials of H and Mu are essentially the same. Therefore, for chemists, muonium is a light isotope of hydrogen. Its radioactive character enables one to observe it under conditions where H would be obscured, and as a light isotope the substantial mass difference makes Mu an exceptionally sensitive probe for study of H.

Techniques for monitoring the muon's behaviour in matter are known as "Muon Spin Rotation" (μSR) [3,8,9] since the vast majority of experiments in this field have relied upon measurement of the precession of the muon's magnetic moment in a transverse magnetic field. In μSR experiments, a beam of polarized positive muons is stopped in a target mounted in a uniform magnetic field perpendicular to the muon spin polarization direction, and the time evolution of muon spin polarization as a function of magnetic field is monitored. The details of the technique will be described later.

In 1963 Brodskii [10] suggested that muonated free radicals should be formed by addition of Mu to unsaturated molecules. Roduner *et al* first observed muonated radicals in the liquid phase in 1978 [11]. The muon-electron hyperfine coupling constants (hfcc) in many muonated free radicals have been measured by μSR spectroscopy [11,12]. In 1984, Abragam pointed out the possibility of using muon level-crossing resonance (μLCR) spectroscopy in μSR experiments [13]. The μLCR effect occurs at specific applied magnetic fields where a muon transition frequency is matched to that of some other nucleus in the coupled spin system. At such a field, a pair of nearly degenerate levels having different spin orientations for the muon and another nucleus are mixed by the hf interaction, resulting in a resonant-like change in the μSR spectrum as the magnetic field is swept. The μLCR technique makes it possible to measure the nuclear hfcc other than those of the muon, and μLCR studies on muonated free radicals have been carried out since the middle of 1985 [14,15].

1.2. Organization of the dissertation

The original topic of this thesis, as proposed in 1986 [16], was investigation of the kinetic behaviour of muonium in aqueous solutions by determining the transition state parameters from the pressure and temperature dependence of the rate constant for reactions involving muonium. After the initial series of high pressure μSR experiments [17], the newly developed μLCR technique became routinely available at TRIUMF, and the study of muonated radicals using μLCR spectroscopy became the main project of the SFU (Simon Fraser University) μSR group [18]. Consequently, the study of intramolecular motion for muonated alkyl and cyclohexadienyl radicals forms a major part of this dissertation.

This thesis is composed of three parts. In the first part, the remainder of chapter one describes the theoretical background and the principles of the μSR and μLCR spectroscopies. Chapter two details how these techniques are applied to the measurement of muonium reaction rates and determination of hfcc of muonium-substituted free radicals. Included are descriptions of the muon channels at TRIUMF, target apparatus, counting procedures, electronic logic and data acquisition, and methods of data analysis.

Chapters three and four deal with studies of muonium kinetics. Chapter three reports the first application of high pressure measurements in muonium chemistry. The rate constants for reactions Mu + NO_3^- (an activation-controlled reaction) and Mu + MnO_4^- (a diffusion controlled reaction) were measured as functions of pressure and the activation volumes were then determined from the pressure dependence of rate constants. Chapter four reports theoretical studies of the kinetic isotope effects for the reactions H + H_2O_2 and Mu + H_2O_2, including harmonic rate ratio calculations and tunnelling corrections, mainly performed with the semiempirical QCPE program MINDO/3 [19].

The last part of the thesis gives the results of μSR, μLCR and theoretical studies on structures, conformations and intramolecular motion of muonium-substituted alkyl and cyclohexadienyl radicals. The preferred conformations at low temperature and barriers for rotation and inversion in Mu-ethyl and Mu-t-butyl are discussed in chapter five. Chapter six reports a thorough study of C_6H_6Mu, C_6D_6Mu and C_6F_6Mu. Procedures of analysing the temperature dependence of hfcc are developed and some semiempirical calculations are carried out. The equilibrium structures and the vibrational modes of muonium-substituted cyclohexadienyls are discussed.

1.3. Production and decay of positive muons and the μSR technique

Muons are decay products of pions, which in turn are produced in the nuclear interactions that take place when a nucleus is bombarded with high energy particles such as protons. Typical nuclei used for pion production at accelerators are copper and beryllium, *e.g.*,

$$^{9}\mathrm{Be} + \mathrm{p} \rightarrow {}^{10}\mathrm{Be} + \pi^{+} \qquad (1.1)$$

The minimum proton kinetic energy required for pion production in such a nucleus is about 180 MeV. Positive pions (π^+) decay with a mean lifetime of 26 ns to give a positive muon and a neutrino [20]:

$$\pi^+ \rightarrow \mu^+ + \nu_\mu \tag{1.2}$$

The decay process of (1.2) is parity violated, exoergic by about 34 MeV and produces 4.1 MeV μ^+. The pion is a spin-zero particle but the muon neutrino, ν_μ, is a spin-$\frac{1}{2}$ particle with zero rest mass and 100% negative helicity (the helicity operator is defined as the dot product of the spin and momentum direction, *i.e.* $\mathbf{h} = \sigma\cdot\mathbf{p}/\mathrm{p}$, and has eigenvalues of +1 corresponding to the case in which the spin is parallel to the momentum, and -1 corresponding to the opposite case). Because of the conservation of linear and angular momentum, the muons emitted from the decay process (1.2) at the surface of the production target are 100% polarized (negative helicity), nearly monochromatic, and have very high stopping density [21].

While in the sample the muon decays, emitting a positron, a neutrino, and an antineutrino [22],

$$\mu^+ \rightarrow e^+ + \nu_e + \bar{\nu}_\mu \tag{1.3}$$

The decay process (1.3) also violates parity. The electron neutrino has negative helicity while the positron and the muon antineutrino have positive helicities. As a consequence of the conservation of energy, momentum and angular momentum, this three-body decay of the muon is spatially anisotropic with respect to positron emission. As a result, the positron is preferentially emitted along the direction of the muon spin. This anisotropy was first observed experimentally by Garwin *et al* [23]. Besides demonstrating an important property of the muon, this experiment represented the first use of the technique of μSR. After integrating over the momenta of neutrinos, the theoretical positron decay spectrum is given by [24]:

$$\begin{aligned} dR(w,\theta)/dwd\omega &= w^2[(3-2w)-P(1-2w)\cos\theta]/2\pi \\ &= C(1 + D\cos\theta)/2\pi \qquad (1.4) \end{aligned}$$

where $w = E/E_{max}$ is the positron energy in units of the maximal possible energy, $E_{max} = \frac{1}{2}m_\mu = 52.3$ MeV, θ is the angle between the spin of the decaying muon and the momentum of the positron, and P is the degree of spin polarization of the decaying muons. The positron energy spectrum, C, and the asymmetry parameter, D, for P =1 is shown in figure 1-1.

In practice, the positrons are detected with an efficiency $\epsilon(w)$ which is not constant over their energy range. The observed probability distribution then becomes:

$$\begin{aligned} dR/d\omega &= \int dR(w,\theta)/dwd\omega \; \epsilon(w)dw \\ &= \bar{\epsilon}(1 + A\cos\theta)/4\pi \qquad (1.5) \end{aligned}$$

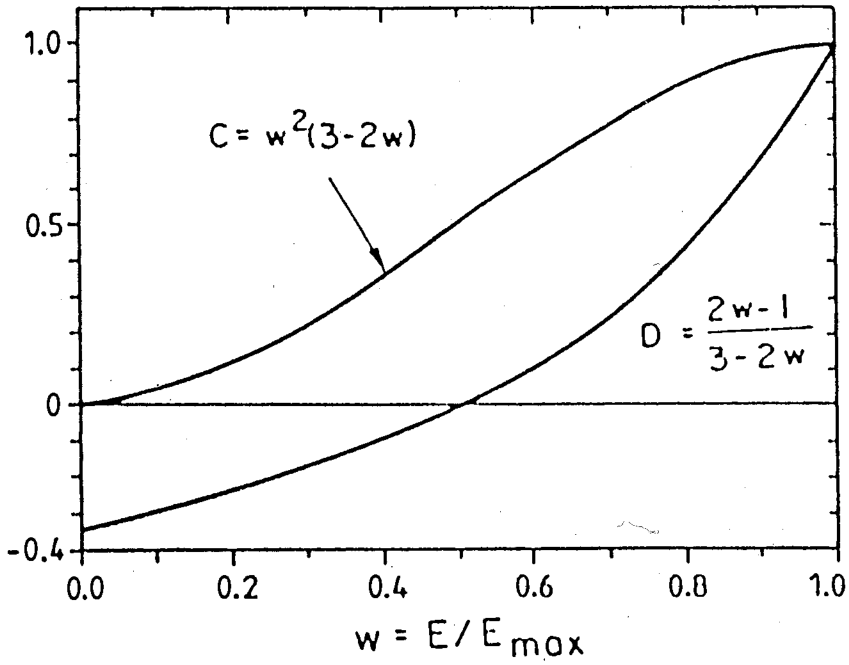

Figure 1-1. Energy spectrum of positrons from muon decay C (upper curve) and energy dependence of the asymmetry parameter D with P = 1 (lower curve) [24].

If positrons of all energies were detected with the same efficiency, the observed average asymmetry A would be $\frac{1}{3}P$. In practice, the detection efficiency of low energy positrons is reduced and the lowest energy positrons are absorbed by matter before reaching the detectors. In most muon experiments, an empirical muon asymmetry A_μ is used, which satisfies the expression:

$$R(\theta) = 1 + A_\mu \cos\theta \qquad (1.6)$$

The time-differential measurement of the asymmetric decay of a spin-polarized ensemble of positive muons precessing in a transverse magnetic field forms the basis of the μSR technique. In a μSR experiment, a longitudinally spin-polarized muon passes from the beam channel through a scintillator counter array and thermalizes in the target material of interest. The counters are arranged to identify any muon which stops in the target; when such an event occurs, an electronic pulse is generated which starts a high precision clock (the clock will be stopped when a positron is detected from the muon decay or reset after a certain time interval since it is started). The muon precesses in the target at a frequency $\omega_\mu = \gamma_\mu B$, where γ_μ is the muon gyromagnetic ratio and B is the transverse magnetic field experienced by the muon. By substituting $\theta = \omega_\mu t$, the positron decay equation (1.6) can be written as:

$$R(t) = 1 + A_\mu \cos\omega_\mu t \tag{1.7}$$

The polarized beam ensures that all muons have the same initial precession phase. For μSR studies, transverse magnetic fields from a few gauss to several kilogauss have been used. A positron counter array placed in the plane of muon precession at an angle ϕ to the initial muon beam monitors the μ^+ decay and generates an electronic pulse to stop the clock previously started by the muon entering the target. The measured time interval is incrementally binned in a time histogram, the clock is reset, and the process is repeated, typically 10^6 to 10^7 times.

Since muon decay is spatially asymmetric, the probability of detecting the decay positron rises and falls as the precessing muon spin swings past the fixed positron detectors. Because the solid angle subtended by the positron counters is usually small, many muon decays are not detected, in which case the clock is reset after some arbitrary 'time out' period of several muon lifetimes. The resultant μSR time histogram has the form [25]:

$$N(t) = N_0(B_g + e^{-t/\tau})[1 + A(t)] \tag{1.8}$$

where $N(t)$ is the number of counts in a histogram time bin, N_0 is a normalization factor, τ is the muon lifetime of 2.2 μs and B_g is a time-independent background due to accidental events.

A(t) is the asymmetry usually given by the summation of the diamagnetic signal $A_D(t)$ and the muonium signal $A_M(t)$. The diamagnetic signal fits ($A_M(t)$ will be given in section 1.4.):

$$A_D(t) = A_\mu e^{-\lambda t}\cos(\omega_\mu t + \phi_\mu) \tag{1.9}$$

where the amplitude A_μ contains information on the fraction of muon polarization of this particular muonic species, λ is the decay rate (usually negligible for diamagnetic species) and ω_μ is the muon precession frequency from which various chemical states of the muon can be characterized. A typical μSR time spectrum is shown in figure 1-2, its most dominant features are the exponential muon lifetime upon which is superimposed the oscillating muon asymmetry.

1.4. Muonium

In muonium, the muon spin is not only coupled to an external magnetic field but also to the electron spin *via* the hyperfine (hf) interaction [26]. Since the muons are polarized while the captured electrons are unpolarized, the initial spin states of Mu are assumed to be 50% $|\alpha_\mu\ \alpha_e>$ and 50% $|\alpha_\mu\ \beta_e>$, where the muon polarization direction is the quantization axis. The spin Hamiltonian

$$\hat{H}(\mathrm{Mu}) = \nu^e S_z - \nu^\mu I_{\mu z} + A_\mu \mathbf{S}\cdot\mathbf{I}_\mu \tag{1.10}$$

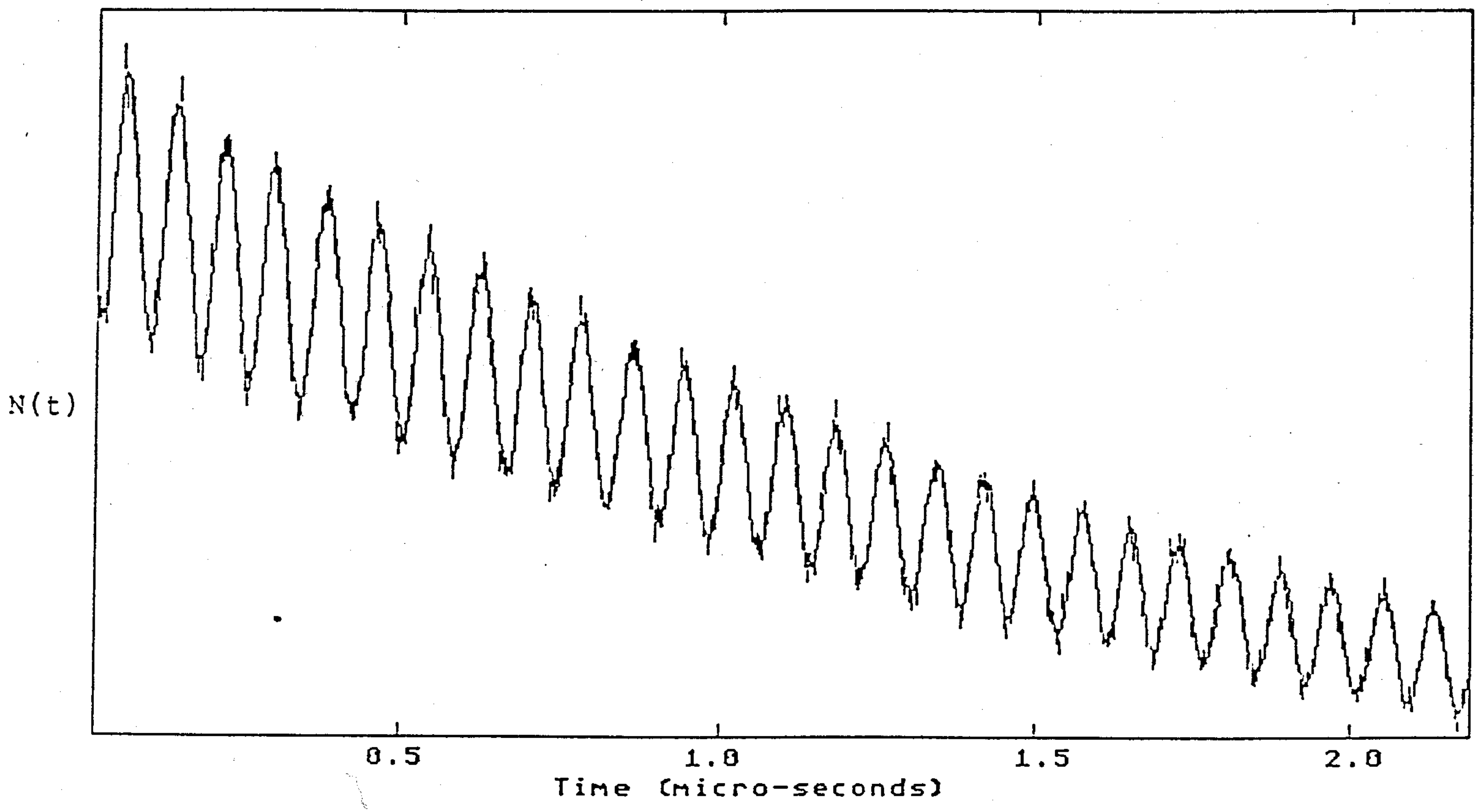

Figure 1-2. μSR time histogram of diamagnetic signal of water.

has four spin states for muonium, a singlet and a triplet at zero magnetic field. If a magnetic field is applied to muonium, the degeneracy of the triplet state is lifted. Figure 1-3 describes the variation of the energy levels of the four spin states as a function of the strength of the applied field (Breit-Rabi diagram). In general, in a transverse magnetic field, the time evolution of the μ^+ spin polarization in Mu is quite complicated, but it is much simpler in the weak-field limit (≤ 10 gauss). In the latter case, half of the spins precess at the muonium Larmor frequency, $\omega_{Mu} = 103\omega_\mu$, in the sense opposite to free muon precession; the remainder of the muon polarization oscillates at the hf frequency, $\omega_0 = 2.8\text{x}10^{10}$ rad/s. Since the experimental time resolution of μSR is about 2 nanoseconds for conventional apparatus, the hf oscillation is not observable and this half of the muonium ensemble appears to be totally depolarized [27].

Monitoring the time evolution of the μ^+ spin in Mu in weak transverse magnetic field *via* the asymmetric muon decay forms the basis for studying muonium. The method is identical with that for the muon with the exceptions that the muon precession frequency in Mu is 103 times that for the free muon, and that the muon asymmetry in Mu is reduced by half. The muonium signal $A_M(t)$ takes the form:

$$A_M(t) = A_{Mu}e^{-\lambda_M t}\cos(\omega_{Mu}t + \phi_i) \qquad (1.11)$$

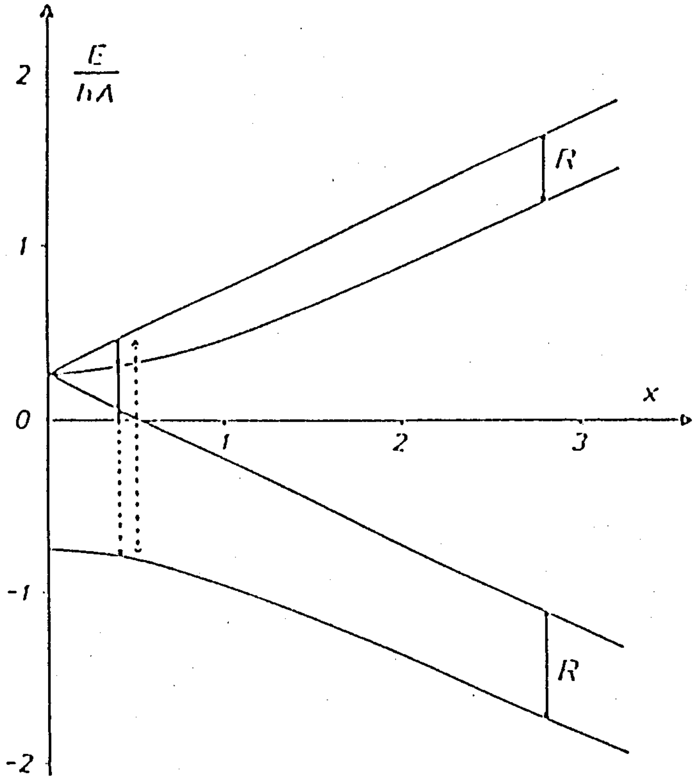

Figure 1-3. Breit-Rabi diagram for a two spin-$\frac{1}{2}$ system [12]. The magnetic field parameter x = field/x_0 and x_0 = 1590 gauss is the ratio of hf frequency of Mu (A = 4463 MHz), to the gyromagnetic ratio of electron (γ_e = 2.80 MHz/G). Of the four allowed transitions, only the two denoted by full lines are resolvable in a low transverse field μSR experiment.

Equation (1.11) is similar to expression (1.9) and the parameters have similar meanings except that in (1.11) they refer to muonium instead of the muon.

From the muonium decay rate λ_M, the pseudo-first order decay rates for chemical reactions of muonium can be determined. This will be further discussed in chapter three.

1.5. Muonium-substituted free radicals

1.5.1. Muonium-substituted free radicals in transverse magnetic field

Radicals are molecular species which are paramagnetic by virtue of a single unpaired electron. The majority of radicals are reactive species. Measurements of electron-nuclear hf couplings not only serve to identify the species, but also provide detailed information on the nature of the singly occupied molecular orbital and hence on molecular structure and dynamics. The temperature dependence of the hfcc can give information on radical conformations and intramolecular potentials.

In muonium-substituted radicals containing magnetic nuclei besides the muon, the electron spin is coupled to these nuclei, as well as to the muon. The spin Hamiltonian for such a multispin system is (in gas and liquid phase, where the anisotropic parts of the hf tensors are averaged out due to the rapid tumbling motion of the molecule):

$$\hat{H} = \nu^e S_z - \nu^\mu I_{\mu z} - \sum_k \nu^k I_{zk} + A_\mu \mathbf{S}\cdot\mathbf{I}_\mu + \sum_k A_k \mathbf{S}\cdot\mathbf{I}_k \qquad (1.12)$$

where ν^e, ν^μ and ν^k (k stands for nuclei) are the Zeeman frequencies, and A_μ and A_k are the Fermi contact hfcc [22] for muon and other nuclei, respectively. For N nuclei with quantum numbers I_n this hamiltonian leads to $4\Pi_n^N(2I_n+1)$ eigenstates. From quantum mechanics, the selection rule for the transitions between these states is $\Delta M = \pm 1$ with $M = m_\mu + m_e + \sum_k \nu^k m_k$ (m's have the usual meanings as magnetic quantum numbers) [28], and the system generally oscillates between many of these eigenstates. Consequently, the muon polarization is distributed over many frequencies. For low fields, in particular, this renders the detection of muonium-substituted radicals difficult or even impossible. However, in higher fields satisfying the condition ν^e much greater than A_μ and A_k for all k, the frequency spectrum is considerably simplified. Under such conditions, the simple product spin states are usually good approximations to the eigenstates of the spin Hamiltonian (1.12), and the selection rule becomes $\Delta m_\mu = \pm 1$, $\Delta m_e = 0$ and $\Delta m_k = 0$. Under this condition, there are only two frequencies in the radical spectra at [28]

$$\nu^{+} = |\nu_M + \tfrac{1}{2}A_\mu|,$$

$$\nu^{-} = |\nu_M - \tfrac{1}{2}A_\mu| \qquad (1.13)$$

where $\nu_M = \frac{1}{2}\{[A_\mu^2 + (\nu^e + \nu^\mu)^2]^{\frac{1}{2}} - \nu^e + \nu^\mu\}$ is the muon Larmor frequency ν^μ, shifted by a small amount dependent on the relative magnitudes of the electron Larmor frequency and the muon hfcc.

The μSR signals of muonium-substituted radicals are usually analysed in frequency space rather than in time space [29]. Figure 1-4 shows a typical μSR Fourier transform spectrum for a muonium-substituted radical.

Using the conventional μSR technique, the vast majority of free radical experiments must be carried out in strong magnetic fields in order to avoid the spread of the initial muon spin polarization over a multitude of frequencies. The muon frequency spectrum is insensitive to nuclear hf interactions in high transverse field and is too complicated to resolve in low field. As a consequence, the information concerning nuclear hf couplings is lost and the identification of the radicals has to rely on a comparison of the muon hfcc with the proton hfcc of the analogous hydrogen radicals. Moreover, in transverse

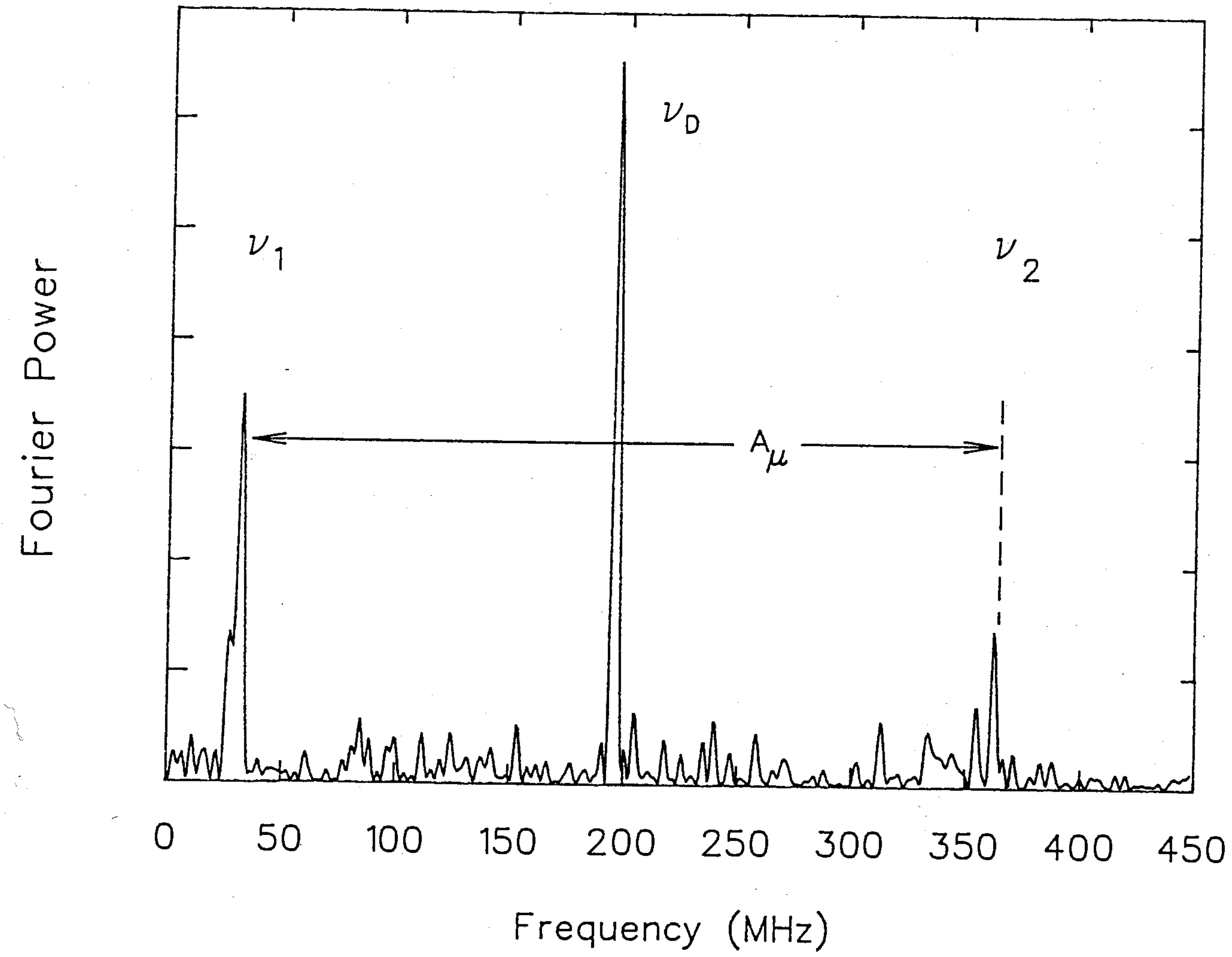

Figure 1-4. Fourier transformed spectrum of muonium-substituted ethyl radical.

magnetic fields, muonated radicals can only be observed if the radical formation rate is large compared with the muon spin precession frequency of the precursor. With muonium as precursor, this imposes a low limit of about 10^9–10^{10} s^{-1} [15]. As a consequence, samples to be studied by μSR must have large radical formation rates or be in high concentrations, *i.e.* even for concentrations in the molar range the rate constant must be larger than 10^9 M^{-1} s^{-1}.

1.5.2. μLCR spectroscopy

In the gas and liquid phases, the spin Hamiltonian for a muonium-substituted free radical with N magnetic nuclei besides the muon is given by equation (1.12), in frequency units. In the high field limit, where the electronic Zeeman frequency is much larger than the hf frequencies, the eigenstates of a multiple spin system |m> can be written in the basis of the product spin states,

$$|m\rangle = \sum_i c_{im}|x_{ei}\rangle|x_{\mu i}\rangle\prod_k|x_{ki}\rangle \qquad (1.14)$$

For a three-spin-$\frac{1}{2}$ system with an electron, a muon and one nucleus with spin $\frac{1}{2}$, there are eight spin states, *i.e.* $|\frac{1}{2},\frac{1}{2},\frac{1}{2}\rangle$, $|\frac{1}{2},\frac{1}{2},-\frac{1}{2}\rangle$, $|\frac{1}{2},-\frac{1}{2},\frac{1}{2}\rangle$, $|\frac{1}{2},-\frac{1}{2},-\frac{1}{2}\rangle$, $|-\frac{1}{2},\frac{1}{2},\frac{1}{2}\rangle$, $|-\frac{1}{2},\frac{1}{2},-\frac{1}{2}\rangle$, $|-\frac{1}{2},-\frac{1}{2},\frac{1}{2}\rangle$ and $|-\frac{1}{2},-\frac{1}{2},-\frac{1}{2}\rangle$. Due to the dominance of the electron Zeeman term in the Hamiltonian (1.12), the energy levels form two well separated groups according to the sign of m_s (The gap caused by the electron Zeeman term is about 10^4 MHz per tesla. For protons, the hf energy level gap is typically 2 or 3 orders less). Practically, the transitions to be observed are between the states with same m_s. The 2x2 sub-secular determinant in this basis set after block-diagonalization is [30],

$$\begin{vmatrix} E_{11}+(A_\mu^2/4\nu^e)+(b^2A_k^2/4\nu^e)-E & cA_\mu A_k/4\nu^e \\ cA_\mu A_k/4\nu^e & E_{22}+(c^2A_k^2/4\nu^e)-E \end{vmatrix} \qquad (1.15)$$

where $E_{ii}=m_s\nu^e-m_\mu\nu^\mu-m_k\nu^k+m_sm_\mu A_\mu+m_sm_kA_k$, $b^2=I_k(I_k+1)-M(M+1)$, and $c^2=I_k(I_k+1)-M(M-1)$.

By solving the eigen problem (1.15) and then integrating the muon polarization over t (from zero to infinity with weight $\lambda e^{-\lambda t}$), the time-integrated signal of μLCR can be obtained. The general expression for the muon polarization in a multi-spin system at the high field limit is [30],

$$P_z(B) = 1 - 2\sum_i \omega_{0i}^2/N\{\lambda^2 + \omega_{0i}^2 + [2\pi(B-B_{0i})(\gamma_\mu-\gamma_k)]^2\} \qquad (1.16)$$

where N is the dimension of the Hamiltonian matrix and γ_i's are the magnetogyric ratios. $\omega_0 = \pi cA_\mu A_k/B_0\gamma_e$ represents the transition frequency at the resonance and λ is the damping rate, which describes all processes that take the muons out of resonance, usually the physical muon decay and chemical reactions. B_0 is the resonance field given by:

$$B_0 = \tfrac{1}{2}[(A_\mu - A_k)/(\gamma_\mu - \gamma_k) - (A_\mu^2 - 2MA_k^2)/\gamma_e(A_\mu - A_k)] \qquad (1.17)$$

Near this field the off-diagonal terms of the spin Hamiltonian are no longer negligible, as they serve to mix the two states. The result is actually a non-crossing of the energy levels. Measurement of the field at resonance leads to accurate determination of the magnitude and sign of the nuclear hf frequency relative to that of the muon. Figure 1-5 shows a schematic diagram of energy levels and the calculated muon polarization curve for a μ^+–e^-–p system.

The selection rule of μLCR for isotropic spin systems is $\Delta(m_\mu + m_k) = 0$. The situation in the solid is different. The anisotropy of the hf interactions gives rise to an additional μLCR for which $\Delta(m_\mu + m_k) = 1$ (only m_μ changes) [31]. This type of μLCR was observed from frozen isobutene and it will be discussed in chapter five.

One of the most remarkable features of the μLCR's in high field is that the position and magnitude of each resonance are insensitive to the number of nuclei off resonance. This characteristic makes the μLCR technique suitable to measure

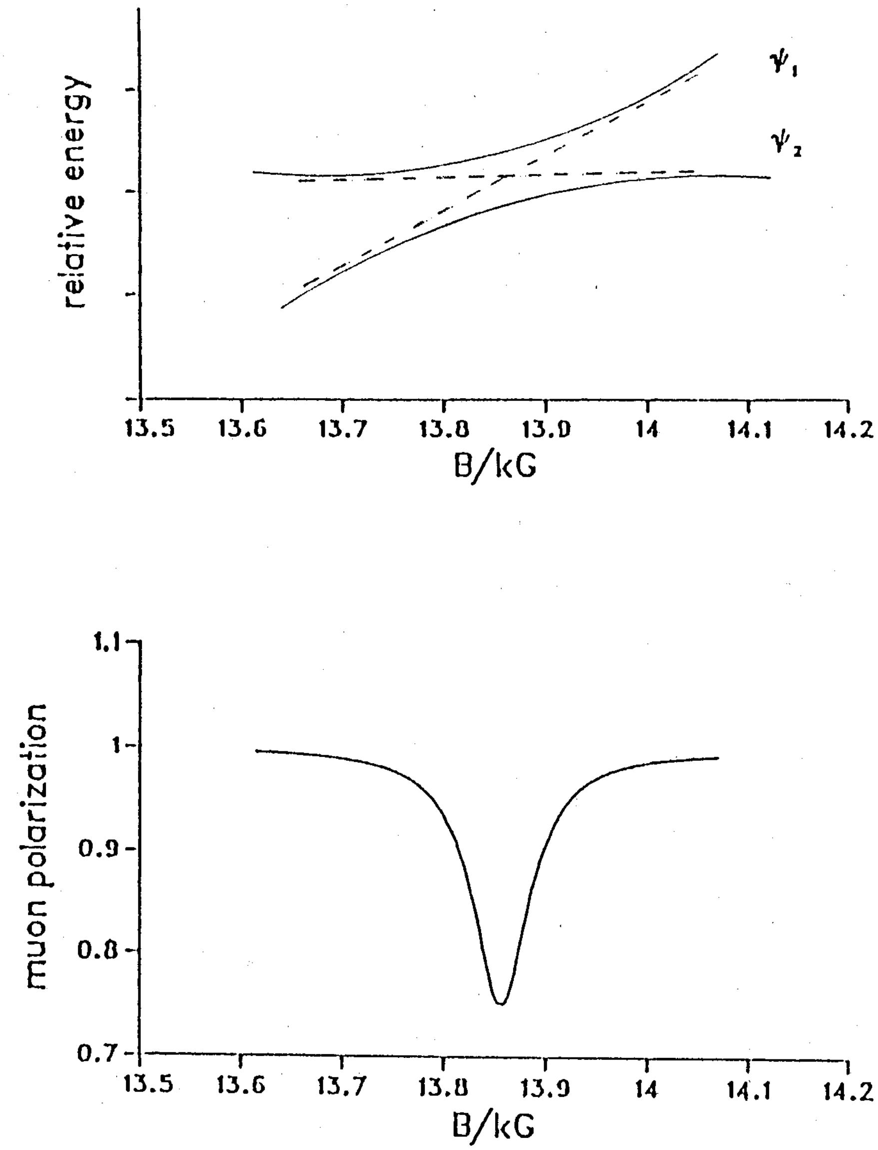

Figure 1-5. Top: A schematic diagram of energy levels for states $|m_e\ m_\mu\ m_p\rangle = |\frac{1}{2}\ -\frac{1}{2}\ \frac{1}{2}\rangle$ and $|\frac{1}{2}\ \frac{1}{2}\ -\frac{1}{2}\rangle$ for the μ^+–e^-–p system; Bottom: muon polarization curve calculated from (1.16) with A_μ=355.9 MHz and A_p=98.4 MHz for the same system.

nuclear hf parameters in complicated spin systems. The μLCR technique is also sensitive to the relative signs of the muon hf frequency and that of the coupled nucleus. Another advantage of μLCR is the high resolution obtainable. The errors in the resonance position are due primarily to uncertainty in the field calibration. A few gauss uncertainty in the resonance position leads to hf frequencies precise to about 0.05 MHz.

The μLCR technique also provides the possibility to detect slowing forming radicals, including those which are evolving from a radical reaction. Radicals will be observed even when a Mu precursor has a lifetime of a microsecond, as long as the transition frequency ω_0 is high enough to produce a significant μLCR signal in the remaining muon lifetime. The loss of polarization during the precursor stage is negligible in high longitudinal magnetic fields.

μLCR studies on muonated radicals show that μLCR is a powerful spectroscopic technique. Its spectra can give extra information about non-muon spin interactions which can be readily used to determine nuclear hf structure in paramagnetic spin systems involving muons. μLCR complements conventional μSR by providing additional information which should be useful in identifying radicals and exploring electron spin distributions and intramolecular motion of muonated radicals. Figure 1-6 is a typical μLCR spectrum obtained at TRIUMF.

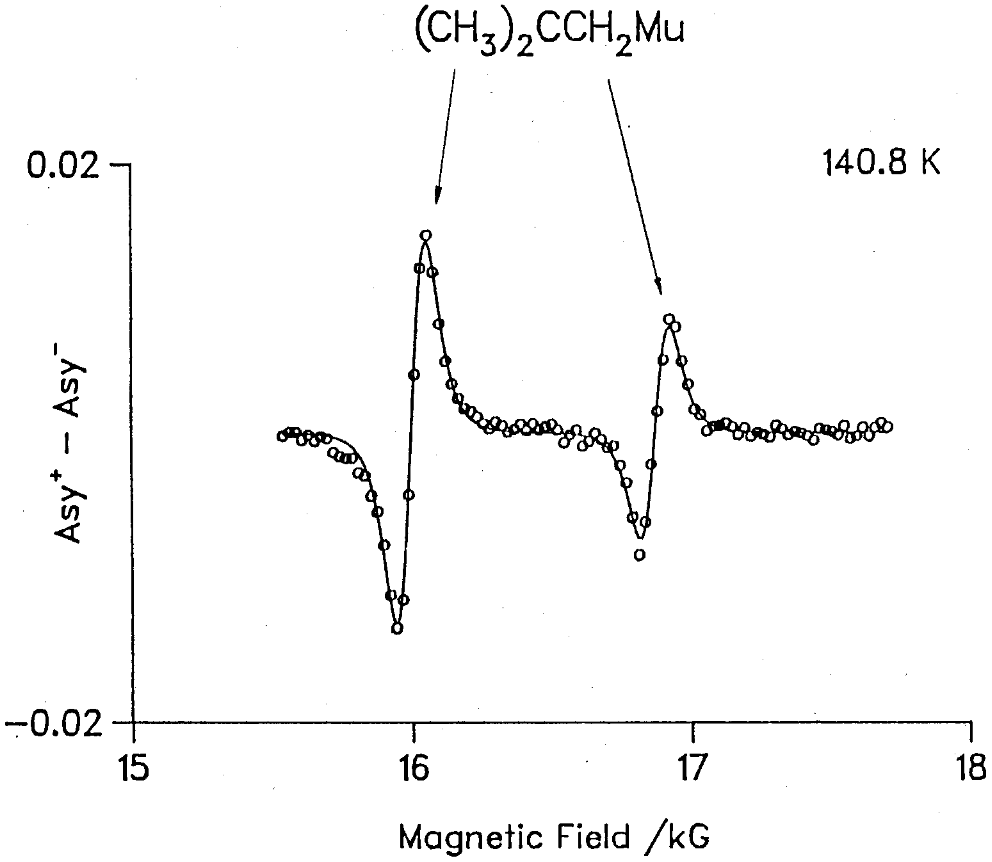

Figure 1-6. Muon level-crossing spectrum of muonium-substituted t-butyl radical at 104.8 K, showing experimental data (o) and the best fit line.

CHAPTER TWO

Experimental and Instrumentation

2.1. TRIUMF and its μSR channels [32,33]

2.1.1. TRIUMF

TRIUMF is Canada's national meson facility. It is managed jointly by four universities (the University of Alberta, Simon Fraser University, the University of Victoria and the University of British Columbia) and operated under a contribution provided by the National Research Council of Canada. The experimental program is based on a cyclotron capable of producing simultaneously several beams of protons, individually variable in energy, from 183 to 520 MeV. The high-current capability of the cyclotron — 150 μA at 500 MeV — qualifies TRIUMF as a "meson factory". Figure 2-1 shows the layout of the TRIUMF cyclotron and experimental areas.

From the viewpoint of an experimenter, one of the most important features of the TRIUMF cyclotron is the 100% macroscopic duty cycle: seen on a macroscopic time scale (as short as a microsecond), the proton beam appears to be a continuous current without a time structure (dc beam, means that the muons will arrive at more or less random intervals, the

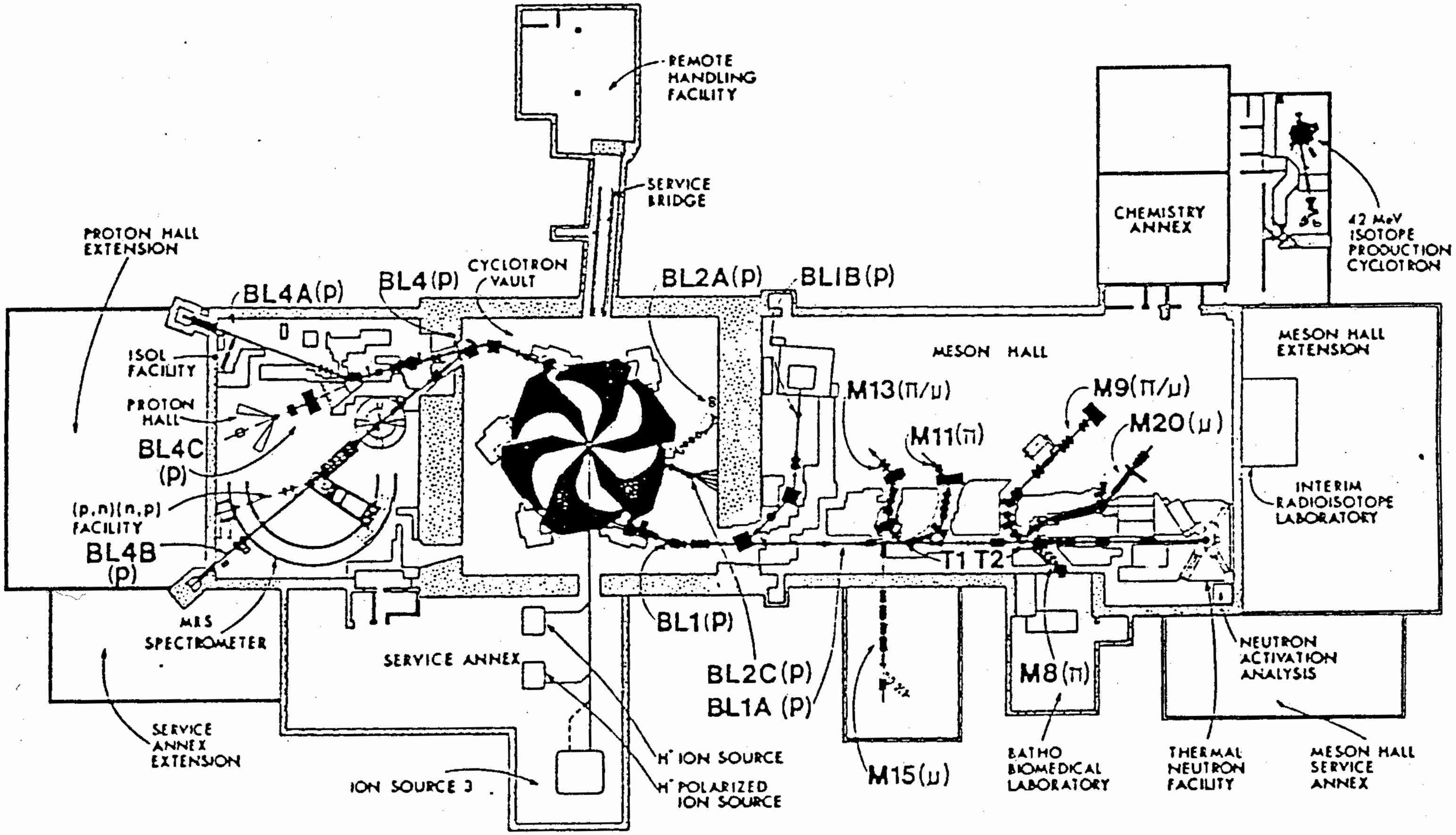

Figure 2-1. TRIUMF cyclotron and experimental areas [33].

average interval being determined by the total beam rate). The microscopic duty cycle is a 3 nanosecond burst of protons every 43 ns. Both the macroscopic and the microscopic structures of the beam can be changed by a number of devices.

Three beam lines are fed by the cyclotron: beam line 1 delivers beam to the meson hall; beam line 4 provides beam to the proton hall; and beam line 2C delivers low-energy beams for the production of radioisotopes.

Beam line 1 has two legs, 1A and 1B. 1A is the major beam line and normally delivers up to 150 μA of 500 MeV protons to several meson production targets. The first of these, 1AT1, feeds three secondary channels, M11 (a medium-energy, 80 to 300 MeV, pion channel), M13 (a low-energy, stopped pion/muon channel) and M15, a surface muon channel. 1AT2 is the second target encountered. This target also feeds three experimental channels, M9 (a stopped pion/muon channel), M8 (a pion channel for biomedical use) and M20, a stopped muon beamline essentially dedicated to μSR.

The experiments of this work were carried out at TRIUMF's M15 and M20 channels. Their main features will be described in the following sections.

2.1.2. M20 and M15 muon channels

The M20 channel is a decay muon channel and M15 is a surface muon channel. Figures 2-2 and 2-3 show the plan views of M20 and M15, respectively. In these secondary beam lines, quadrupoles and bending magnets are used for the collection and momentum selection of the particles emitted from the production targets, and the focusing of the selected particles. The dc separators may be operated at low voltage to eliminate beam positron contamination, or at high voltage to rotate the muon spin by 90°. Both the beam lines can be optimized using simple but effective automatic programs by tuning more than 20 of their elements.

2.1.2.1. Backward muons

Two different operating modes are commonly used to deliver the beam into the experimental area: backward and surface muon modes. In the backward mode, positive pions produced from 1AT2 are collected by the quadrupole doublet then momentum selected by the bending magnet. The muons are produced from pions decaying in flight after the first bending magnet and muons formed with momentum in the opposite direction to the pion beam (backward) are collected. The second bending magnet is tuned to momentum select the backward muons from the other particles in the beam (e^+, π^+, μ^+, and p). The resultant high momentum

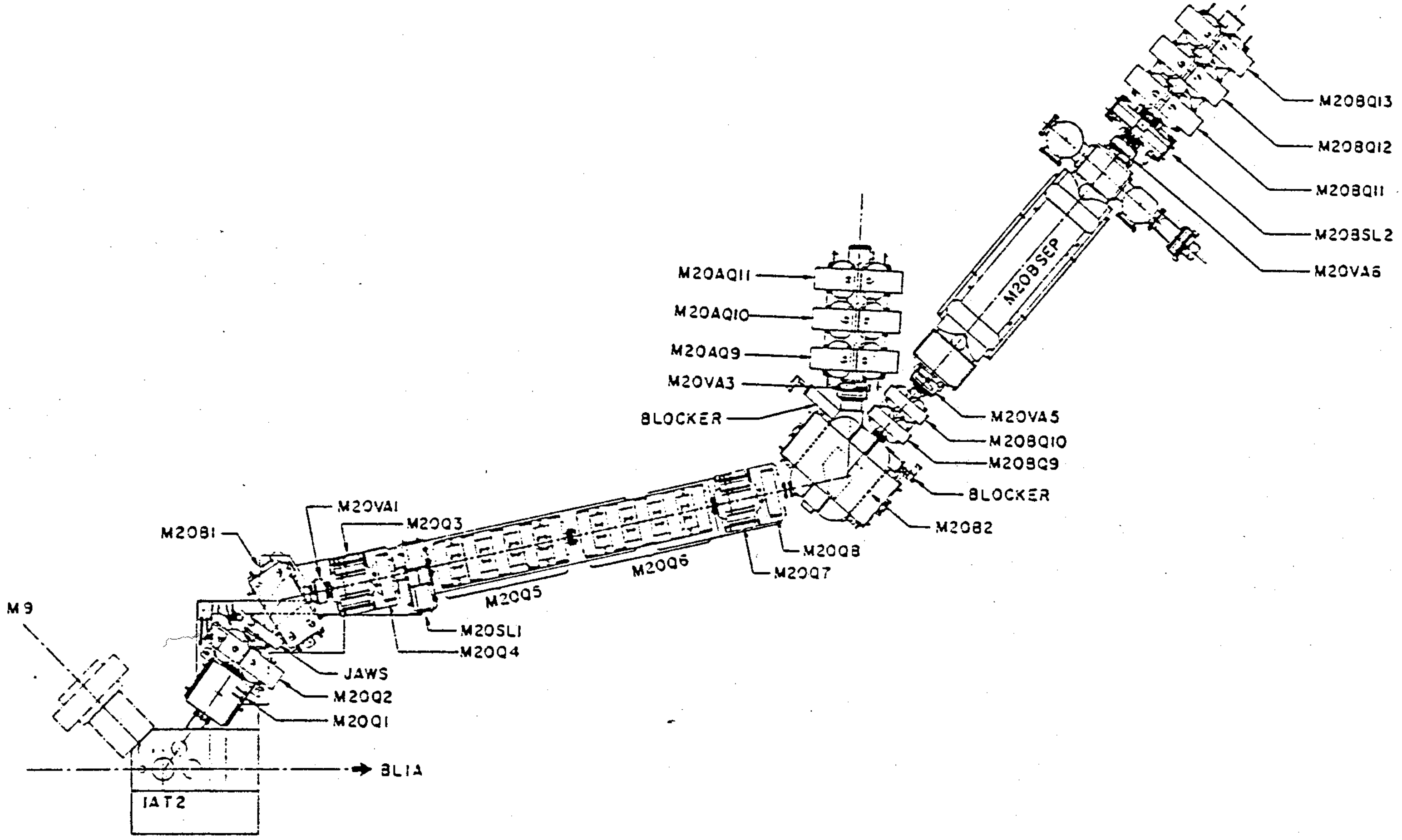

Figure 2-2. A plan view of the M20 channel at TRIUMF [34].

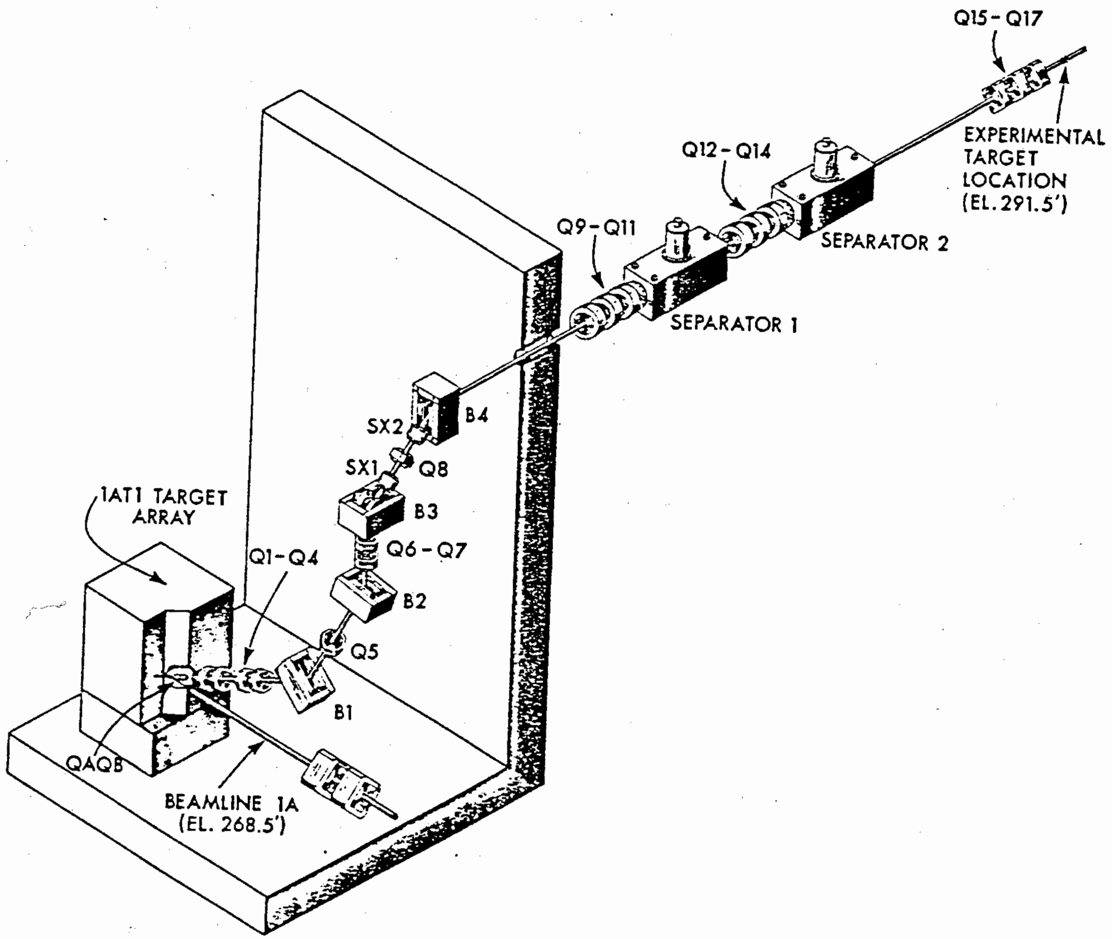

Figure 2-3. A plan view of the M15 channel at TRIUMF [33].

polarized μ^+ beam is delivered to the μSR apparatus.

2.1.2.2. Surface muons [35]

The essential difference between backward and surface muon modes is that in the latter case muons come from π^+ decaying before the first bending magnet at rest, within a few μm of the pion production target. Surface muons are nearly monoenergetic (4.1 MeV) with a nominal momentum of 28.6 MeV/c. Contamination of the surface muon beam with pions and protons is negligible. However, there are about 100 times more positrons than muons in the surface muon beam. Also, it is difficult to inject the surface muons into a strong transverse magnetic field, as the radius of curvature < 1 m/kG. The solution is to use a dc separator to remove the positron contamination in the surface muon beam and to rotate the muon spin so that it is transverse to the momentum. The spin rotator consists of a vertically oriented electric field E_0 and horizontally oriented magnetic field B_0. As B_0 affects both the spin and momentum of the muons while E_0 affects the momentum only, it is possible to select values of E_0 and B_0 to allow only particles with a certain mass to traverse the rotator without deflection, and to rotate the muon spin by 90°. Such a rotation permits injection of the beam into a strong magnetic field oriented longitudinally to the momentum but transversely to the muon spin. A single experimental apparatus can be used for both transverse and longitudinal field experiments with the spin rotated and unrotated muons.

2.2. Scintillation detectors [36]

Many transparent substances, including certain solids, liquids and gases, scintillate (*i.e.*, emit flashes of visible light) as a result of the action of ionizing radiation. Organic scintillators are widely applied as detectors of ionizing radiation. Through the application of a sensitive light detector such as a photomultiplier (PM) tube, the light emitted from scintillations can be converted into an electrical signal. Figure 2-4 shows a schematic design for the scintillator used in the experiments. The high voltage (HV in figure 2-4) applied to the PM is normally in the range of 1.5 to 2.5 kV. In order to protect the PM from the magnetic field, the lightpipe has to be 1 to 2 meters long. This limits the time resolution of μSR experiments to about 1 ns.

2.3. Temperature control systems

Two systems of temperature control were used in the experiments described in this thesis. For temperatures between 0 and 100 ^{o}C, the temperatures were controlled by circulating fluid from a constant-temperature bath through copper coils attached to the outside of the gas target or a copper plate attached to the back of the liquid targets. In addition to the

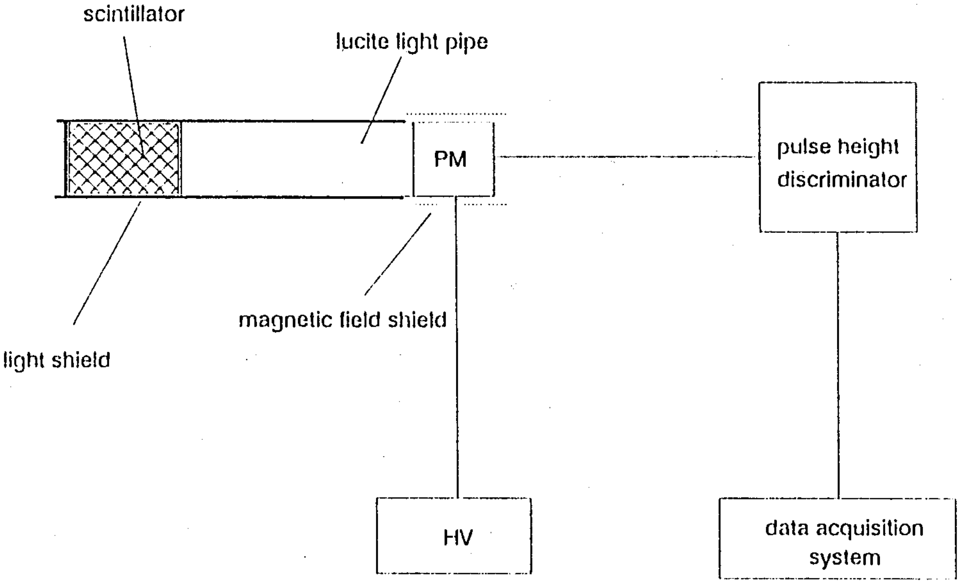

Figure 2-4. General schematic design for a scintillation detector.

direct reading from the circulator, the sample temperatures were also measured by thermometers and recorded for each target. The calibration for a liquid cell showed that the uncertainties of the sample temperature were less than 1 ^{o}C.

Low sample temperatures (20 K to 270 K) were obtained by using a helium-cooled cold-finger cryostat. The cryostat consists mainly of a cold head and a compressor unit. The control temperature of the cryostat is selected and read directly in Kelvin with a cryogenic digital thermometer with silicon diode sensors. The sample temperature was measured with either a silicon diode sensor or a platium resistance thermometer. The uncertainty of the sample temperature is estimated to be about 0.5 K.

2.4. Experimental Setup

2.4.1. Transverse field experiments with backward muons

For the muonium kinetics studies described in chapter three, small magnetic fields (about 10 gauss) were provided by the SFUMU spectrometer (as its name suggests, it stands for SFU muonium chemistry group). SFUMU was designed for backward muon experiments, with several collimators of different sizes to adjust the beam size at the site of the cell window. SFUMU provides uniform magnetic fields of up to 4 kG perpendicular to the beam. Figure 2-5 shows a schematic diagram of the SFUMU

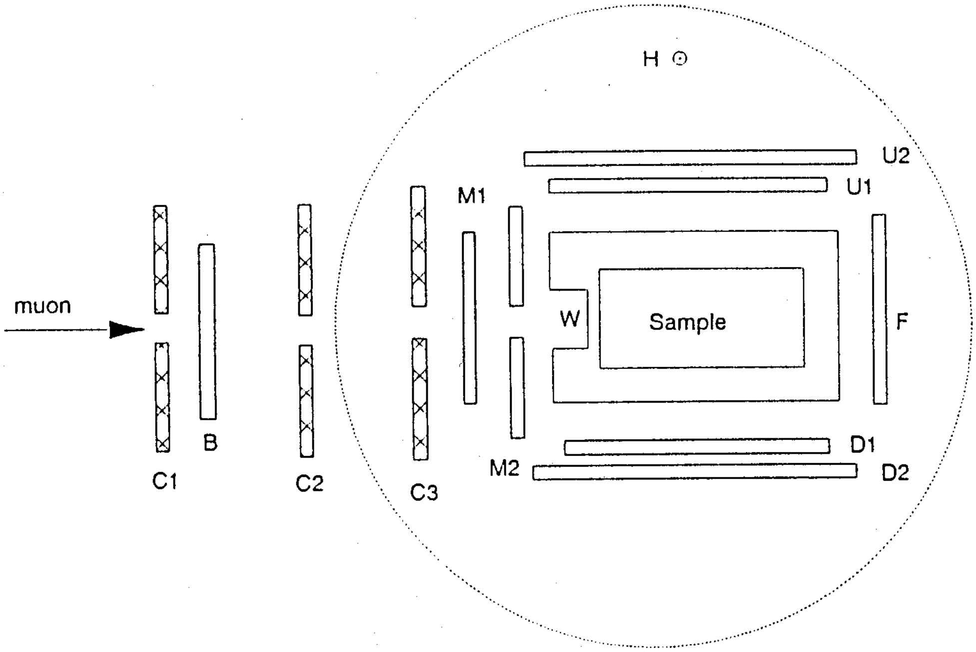

Figure 2-5. Schematic layout of SFUMU setup. C1, C2 and C3 are collimators, W is the window of the sample cell and B, M1, M2, U1, U2, D1, D2 and F are plastic scintillator counters. The magnetic field H is perpendicular to the plane of the paper.

set-up for the high-pressure experiments at M20A. An incoming muon is detected by B and M1. If a muon passes through the window of the sample cell, the veto counter M2 will show no response. The logic signature for a muon stopped in the sample is therefore defined by a signal from B and M1, and none from M2, in short: $B \cdot M1 \cdot \overline{M2}$. Likewise, an emitted positron in the down direction will produce coincident signals from D1 and D2 with the logic signature $D1 \cdot D2$. Similarly, an upward emitted positron can be identified by the logic signature $U1 \cdot U2$.

The principal layout of the electronic detection scheme is shown in figure 2-6. The signals from the photomultipliers are first transformed to standard nuclear instrument and measurement (NIM) pulses of ~20 ns width and then input to various electronic units. A good muon decay event requires that within a certain time interval after a muon stop, a positron is detected. This period is called the data gate and extends usually over several muon lifetimes. The data gate is produced by a gate generator triggered by the muon stop signal. A good decay positron is then identified by a coincidence of the positron signal with the data gate. A clock is started by a muon stop signal and stopped by the good decay event signal. The measured time then forms the address of a histogram memory, and the content of the corresponding channel is incremented by one. In this way a μSR time spectrum is formed.

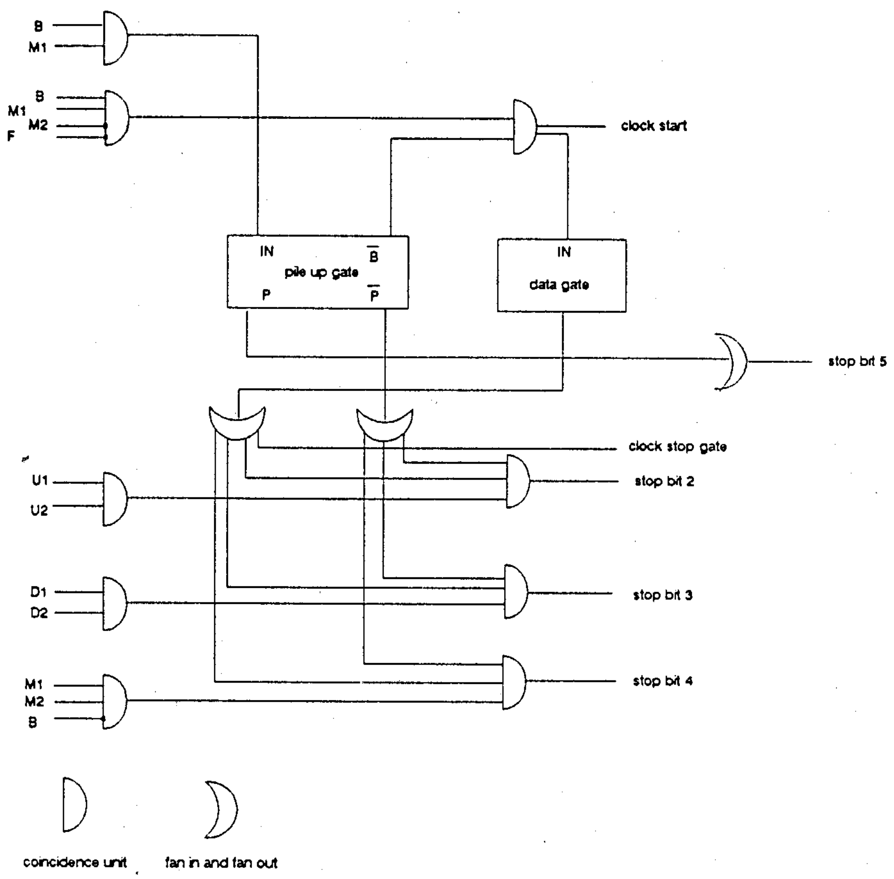

Figure 2-6. Principal components of the electronic detection scheme for time-differential μSR.

In practice the electronics has to check for a number of further details, such as pile-up rejection. A second muon event represents a stopped muon which follows a previously stopped first muon within the time interval defined by the pile-up gate. There are now possibly two muons in the target and a subsequently emerging positron cannot be related unambiguously to the correct parent muon. Such ill-defined events must be excluded. As shown in figure 2-6, this is achieved by requiring that the clock can only be started by a muon signal which is in coincidence with the non-busy signal ($\overline{B}$) from the pile up gate. It is important also to reject those events with the sequence muon(1)/positron/muon(2) all within the data gate set by the muon(1). These events are rejected in software via a "flag" from stop bit 5 as shown in figure 2-6. Such an event would otherwise result in a spectrum distortion because the observation of long-lived muons has a larger probability of suppression by second muons than that of the short-lived muons. By rejecting all second muon events regardless of the relative timing of the second muon with respect to the positron, this kind of bias is removed.

2.4.2. Setup for μLCR experiments

Free radical studies were carried out at relatively high magnetic fields. Transverse-field experiments were used to measure the muon hfcc and to calibrate the magnetic fields.

Longitudinal-field experiments were used to measure the μLCR fields for the nuclei other than the muon. SLC (University of Tokyo's Superconducting Longitudinal Coil) and HELIOS (a custom-built superconducting solenoid) were used to provide these magnetic fields (up to 3 tesla for SLC and 7 tesla for HELIOS). Both the magnets were designed for surface muon mode and can take high incident muon rates as required by μLCR experiments. Figure 2-7 shows a schematic representation of the SLC setup and the block diagram of the electronics is given in figure 2-8.

For μLCR experiments, the muon polarization is along the field direction. A thin scintillator counter M registers the arrival of each incoming muon, and decay positrons are separately detected in the four counters FL, FR, BL and BR. There is no theoretical limit on the incoming muon rate since it is not required that there be only one muon in the target at a time, as in the time-differential technique. The process of finding μLCR's involves an integral μSR method in which the integrated muon decay asymmetries A's are recorded as a function of magnetic field. The raw integrated asymmetry is sensitive to systematic effects, such as the deviations due to rate-dependent effects. These are minimized by a 50 G square-wave field modulation. The signal is defined as $A^+ - A^-$, where the muon decay asymmetries $A^\pm = (F^\pm - B^\pm)/(F^\pm + B^\pm)$ and $F^\pm$ and $B^\pm$ are the total number of positron events in the forward and backward

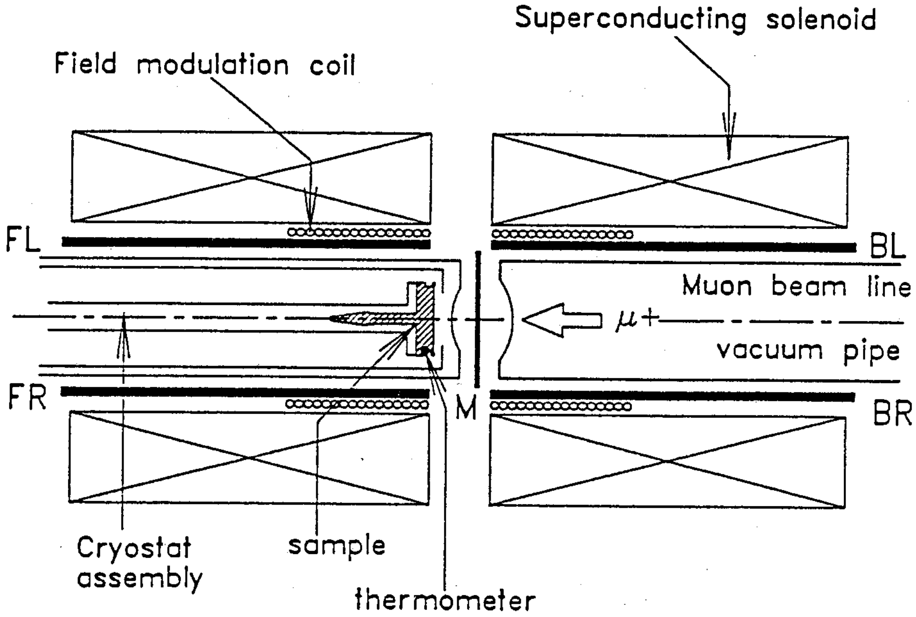

Figure 2-7. Schematic representation of the SLC setup.

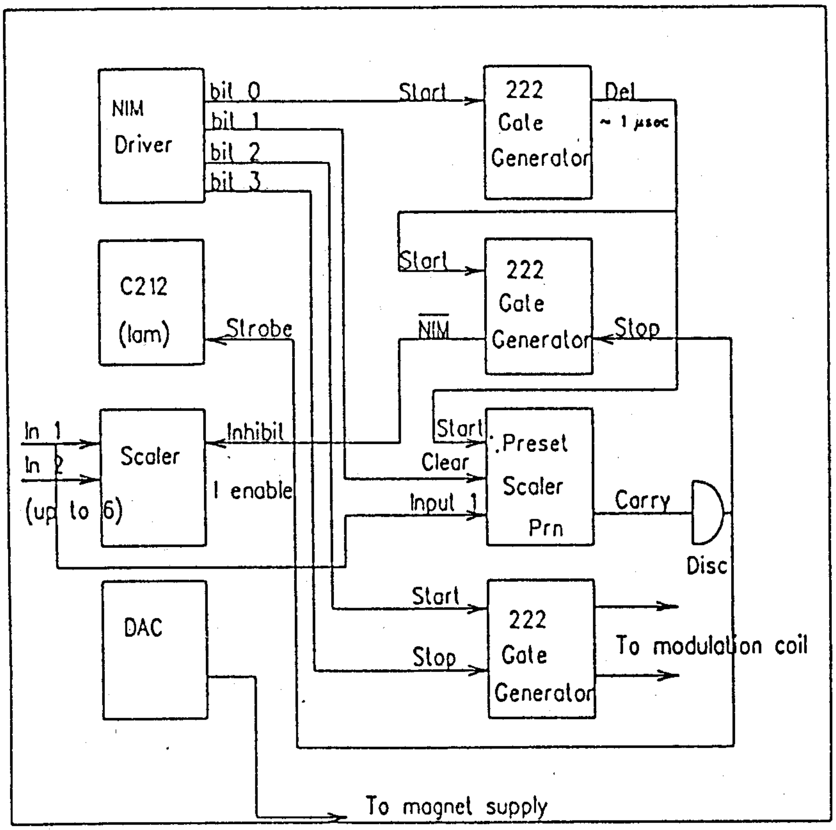

Figure 2-8. Block diagram of the electronics used for μLCR experiments.

telescopes, respectively, normalized to the number of incoming muons. The ± refer to the direction of the square-wave modulation field. For a resonance wider than the field modulation width, the lineshape is approximately field-differential [31].

2.5. Data analysis

The on-line computers in the TRIUMF counting rooms (PDP-11/34 at M15 and PDP-11/60 at M20) were used for data acquisition and monitoring the experiments. Most of the experimental data analysis was performed off-line on the TRIUMF M15VAX and SFU IBM 3081 computers. The main software used is a package of multiparameter chi-squared minimization routines called MINUIT [37]. MINUIT has enough flexibility to allow the user to devise a wide variety of fitting strategies. Two minimization algorithms are normally used: the simplex method of Nelder and Mead [38] and a variation of the Davidon variable metric method [39] called MIGRAD. The latter method, which is particularly efficient given a good set of initial parameter guesses, requires first partial derivatives of the function being minimized; these may be provided analytically by the user or may be calculated numerically by MINUIT. MINUIT can accommodate up to 15 variable parameters, any number of which may be fixed at any time and restored at a later time. Parameters may also be constrained to any physically meaningful numerical range. Covariance matrices and correlation coefficients are calculated by MINUIT, either as an estimate generated by MIGRAD or from the so-called hessian matrix, which is exact for a Gaussian parent distribution. Detailed non-symmetric error estimates of parameters for non-parabolic minima may be calculated by a search method called MINOS.

For the muonium kinetics studies described in chapter three, the raw histograms were fitted to equation (1.8). The muonium decay rate λ_M is the parameter of central interest. The data from different histograms are analyzed independently, and the weighted average [40] values of λ_M are reported.

In the radical studies the μSR time spectra are transformed to frequency space and the peaks are fitted with Lorentzian line shapes to determine the frequencies.

Precise values of magnetic field are essential for μLCR experiments. By measuring the frequencies of diamagnetic signals at different fields and knowing that the gyromagnetic ratio of muon is 13.55 kHz/G,

$$B = B_0 + m \cdot I \qquad (2.1)$$

can be used to calibrate the magnetic fields. In (2.1) B stands for magnetic field, I stands for the current set for the superconducting coil and B_0 and m are constants.

The μLCR spectra are fitted by a theoretical lineshape (the difference between two Lorentzian functions corresponding to the opposite directions of the modulation field) as described in section 2.4.2.

CHAPTER THREE

Pressure-Dependent Muonium Kinetics in Aqueous Solution

3.1. Introduction

To date, the variable of pressure has not been exploited in μSR studies of liquids, in strong contrast to temperature. The dominance of temperature is understandable on both practical grounds (necessary techniques are commonplace and the apparatus is readily available), and because of its greater fundamental significance. In principle, valuable information on the transition state of a chemical reaction can be gained by studying the pressure dependence of the rate constant. The volume of activation is defined by

$$\Delta V^{\ddagger} = -RT(\partial \ln k/\partial P)_T \qquad (3.1)$$

and is interpreted as the difference in partial molar volume between the transition state and the separated reactants. In practice, interpretation is difficult, and $\Delta V^{\ddagger}$ has mostly been used in a semi-quantitative manner in the classification of reaction mechanisms [41]. Thus, Hentz *et al* [42-46] studied the effect of pressure on hydrogen atom reactions in aqueous solutions and classified the reactions into two categories: (1)

activation-controlled reactions of H have $\Delta V^{\ddagger} = -5\ \mathrm{cm^3\ mol^{-1}}$, and (2) diffusion-controlled reactions of H have $\Delta V^{\ddagger} = +2\ \mathrm{cm^3\ mol^{-1}}$.

For activation-controlled reactions, the absence of any appreciable variation of $\Delta V^{\ddagger}$ with reactant led Hentz *et al* to propose a model for the transition state in which the small H atom is completely accommodated within the volume occupied by the reactant molecule, i.e. the partial molar volumes of reactant and transition state are equal. In this model (I) the partial molar volume of H alone determines the activation volume:

$$\Delta V^{\ddagger} = -\bar{V}(H) \qquad (3.2)$$

An alternative model (II) was also considered [43] but subsequently dismissed [46]. It constitutes the other extreme, where the volume of the transition state is the sum of the volume of H and reactant. The relevant H volume would then be the van der Waals volume, $V_w(H)$, and

$$\Delta V^{\ddagger} = V_w(H) - \bar{V}(H) \qquad (3.3)$$

Model I implies that $\bar{V}(H) = 5\ \mathrm{cm^3\ mol^{-1}}$, and model II gives the upper limit of $9.4\ \mathrm{cm^3\ mol^{-1}}$ (based on the van der Waals radius for H of 0.12 nm used by Hentz *et al*).

Given that the molar volume of water is 18 $cm^3\ mol^{-1}$, both the above interpretations predict that $\overline{V}(H)$ is smaller than $\overline{V}(H_2O)$. On the other hand, Klein *et al* [47,48] carried out molecular dynamics simulations of the local structure of water around an isolated hydrogen atom, and concluded that the H atom is larger than a water molecule. It does not necessarily follow, however, that $\overline{V}(H)$ is greater than $\overline{V}(H_2O)$, since the ordering of water molecules in the clathrate-like structure suggested by Klein would make a negative contribution to the partial molar volume of H.

In addition to their simulation of H in water, Klein *et al* carried out similar computations for muonium. In fact, it was a muonium problem that provided the original motivation for their study. The fast reactions of muonium in aqueous solution are subject to the same diffusion limit as the hydrogen atom ($k \sim 2 \times 10^{10}\ M^{-1}s^{-1}$ [49], and this was ascribed to the similarity in diffusion constant and encounter radii. However, one school of thought held that an isotope effect should apply to the diffusion of species as small as Mu and H [50]. Klein *et al* argued that the effective size of Mu and H in water is more closely related to the van der Waals radius than the Bohr radius, and speculated that the diffusion process is limited by the breaking and formation of hydrogen bonds in the local water structure. The pressure dependence of muonium reaction rates provides the means to test these models.

The two reactions investigated in this study are:

$$Mu + NO_3^- \rightarrow MuO^- + NO_2 \qquad (3.4)$$

and

$$Mu + MnO_4^- \rightarrow \mu^+ + MnO_4^{2-} \qquad (3.5)$$

The literature values of the rate constants (at room temperature) are $1.5 \times 10^9\ M^{-1}s^{-1}$ for (3.4) and $2.5 \times 10^{10}\ M^{-1}s^{-1}$ for (3.5), respectively [51]. According to these rate constants, (3.4) is classified as an activation-controlled reaction and (3.5) as diffusion-controlled.

3.2. Experimental

With the exception of the high-pressure aspect, the experiments employed conventional μSR techniques described in chapter one and two. The main effort went into the design and testing of the pressure cell and setup, as this was the first application of high pressure measurements in liquid phase muonium chemistry [17].

The high-pressure cell and fittings are made of a beryllium-copper alloy, heat-treated for maximum strength after machining. A schematic representation is given in figure 3-1. The cell is pressurized with a 7 kbar hydraulic handpump charged with paraffin oil and connected *via* standard non-magnetic stainless-steel high-pressure tubing. A floating piston communicates the applied pressure to the liquid sample, which can be in direct contact with the cell body if non-corrosive. The piston is not needed if the sample is encapsulated in a deformable plastic vial. The muon window is 2.5 mm thick and 12 mm in diameter. The whole apparatus has been tested up to 4 kbar, but the μSR experiments were limited to 2 kbar for safety reasons.

The experiments were carried out at the TRIUMF M20A channel operating in the backward muon mode (muon momentum 88 MeV/c) for high penetration. To ensure a good muon stopping distribution, the beam was reduced in diameter to 10 mm with a series of lead and brass collimators. Scattered muons were vetoed by a scintillator with a 10 mm hole placed just before the window. Decay positrons were detected by two scintillator telescopes, one placed above and the other below the cell. Tests with various standard samples (aluminium, ferric oxide, water, carbon tetrachloride, and 50% manganous nitrate in water) showed that 90±3% of the incoming muons stopped in the sample region, and only 10% in the cell walls and window. Figure 3-2 shows the muon

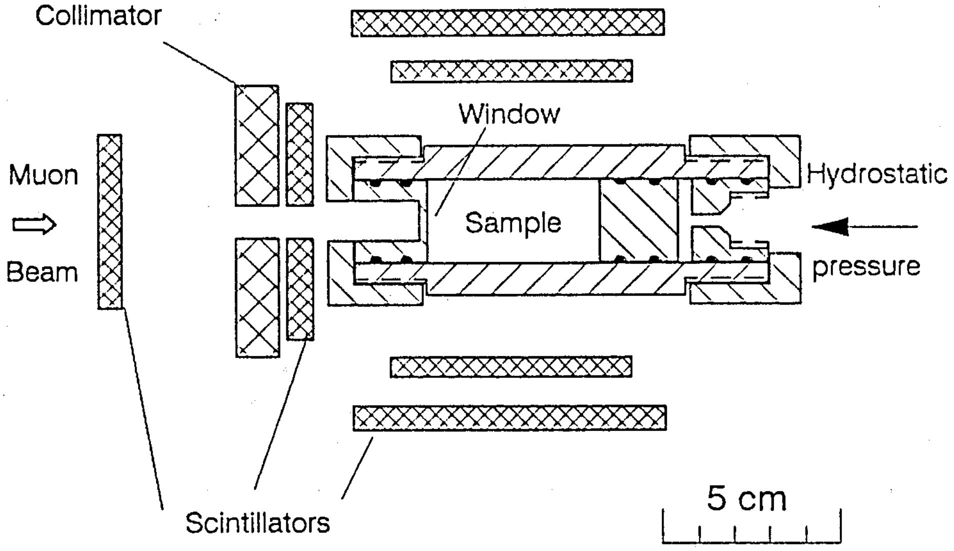

Figure 3-1. Schematic representation of the high-pressure cell and scintillator arrangement.

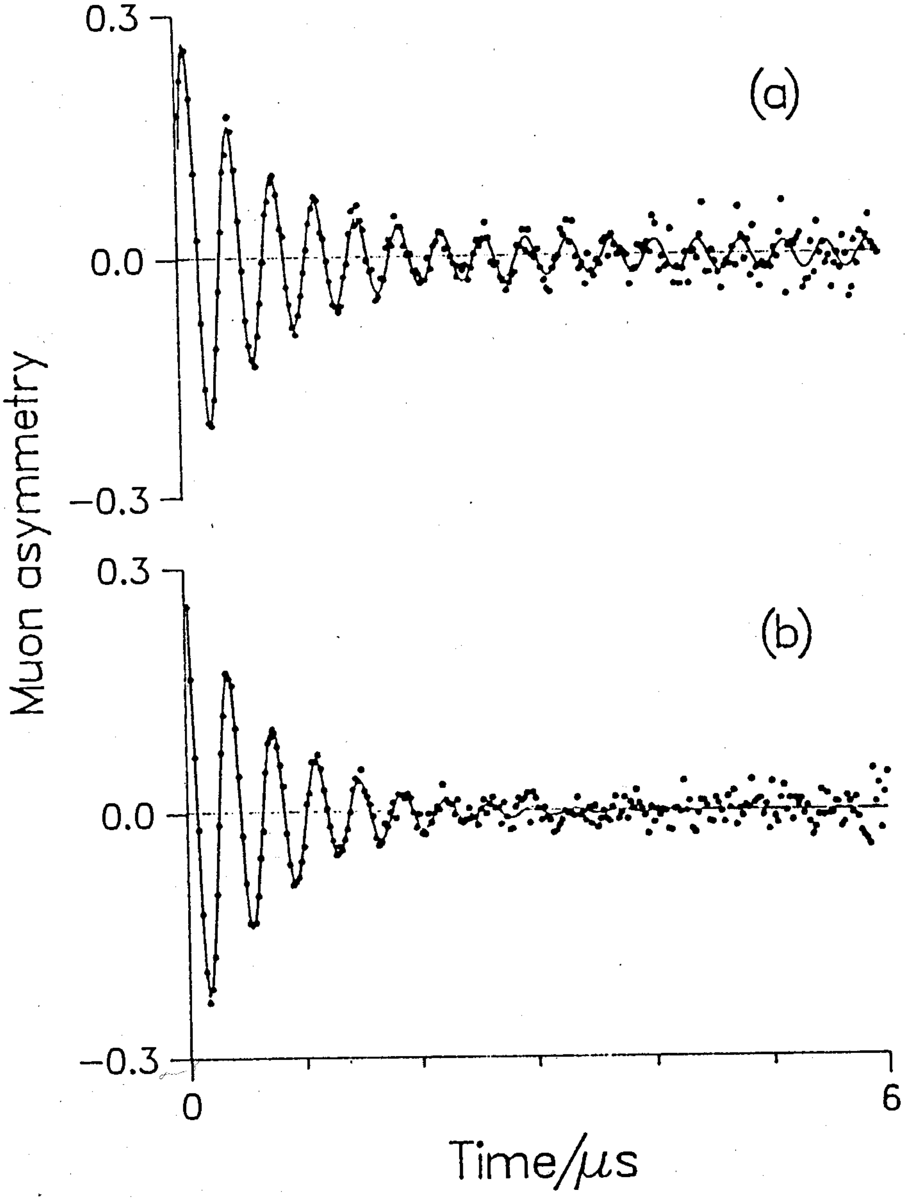

Figure 3-2. Muon asymmetry for a sample of 50% manganous nitrate solution in (a) the high-pressure cell, compared with (b) a conventional thin-walled cell, under an applied field of 200G.

asymmetry for a sample of 50% manganous nitrate solution in the high-pressure cell compared with that for the same sample in a conventional thin-walled cell. The fast-decaying signal is due to muon spin relaxation by the paramagnetic manganous ion. The low-amplitude non-relaxing component seen in the upper curve arises from muons stopped in the non-magnetic material of the cell.

The liquid solutions of $NaNO_3$ and $KMnO_4$ were used for the experiments. Muonium decay rates were measured for pure water, aqueous solutions of sodium nitrate at 0.29 and 0.58 mM, and aqueous solutions of potassium permanganate at 0.050 and 0.10 mM. The samples were prepared at SFU. Since muonium reacts very readily with O_2 ($k_M = 2.4 \times 10^{10}$ $M^{-1}s^{-1}$ in water) all media used for Mu studies need to have the oxygen concentration reduced from air-saturated level (2.6×10^{-4} M) to less than 2×10^{-6} M. This was achieved by bubbling the samples with nitrogen. μSR histograms containing 10-15 million events were accumulated for each of the positron telescopes for high statistics.

3.3. Results and discussion

The muonium decay rates were determined by computer fit of the theoretical expression equation (1.8) and are summarized in table 3-1. These decay rates represent the mean of the experimental decay rates determined from the two histograms, corrected for a contribution (in pure water λ_0 is usually about

Table 3-1

Pressure dependence of muonium rates in aqueous solutions

sample	P(kbar)	$\lambda_M(\mu s^{-1})$	$(\partial \ln k/\partial P)(kbar^{-1})$
0.29 mM $NaNO_3$	0.001	0.62(8)	0.30(8)
	1.00	0.78(8)	
	2.00	1.12(13)	
0.58 mM $NaNO_3$	0.001	0.83(10)	0.29(9)
	1.00	1.11(15)	
	2.00	1.49(19)	
0.05 mM $KMnO_4$	0.001	0.88(15)	-0.16(13)
	1.00	0.63(15)	
	2.00	0.65(14)	
0.10 mM $KMnO_4$	0.001	2.17(23)	-0.12(7)
	2.00	1.71(20)	

$\lambda_M = \lambda_{exp} - \lambda_0$ is the muonium decay rate from chemical reaction. λ_{exp} is the experimentally measured decay rate and λ_0 is the decay rate from solvent.

0.3 μs^{-1}) due to environmental effects. Thus,

$$\lambda_M = \lambda_{exp} - \lambda_0 = k_M[X] \tag{3.6}$$

where [X] represents the concentration of NO_3^- or MnO_4^-. Figures 3-3 and 3-4 show representative muonium precession signals and the decay rates, respectively. The lines through the points in figure 3-4 are weighted least-square fits. Their slopes are given in the last column of table 3-1. The slopes for different concentrations of the same reactant are compatible, and so the mean value was used to compute the volume of activation, through equation (3.1). For Mu + NO_3^- $\Delta V^{\ddagger} = -7.1 \pm 1.5$ cm^3 mol^{-1}, and for Mu + MnO_4^- $\Delta V^{\ddagger} = 3.1 \pm 1.6$ cm^3 mol^{-1}.

Since the rate constant for the reaction between Mu and NO_3^- is an order of magnitude less than the diffusion limit, this reaction is classified as activation-controlled, and the activation volume can be interpreted in terms of Hentz's models. Under model I, the partial molar volume of muonium is calculated from equation (3.2) to be $\overline{V}(Mu) = 7.1$ cm^3 mol^{-1}. A larger value is obtained from equation (3.3), model II: $\overline{V}(Mu) = 11.5$ cm^3 mol^{-1}, assuming $V_w(Mu) = 4.4$ cm^3 mol^{-1}. The true situation probably lies between these limits. Although there is some additional uncertainty as to the appropriate value of $V_w(Mu)$, the comparison with $\overline{V}(H)$ remains constant:

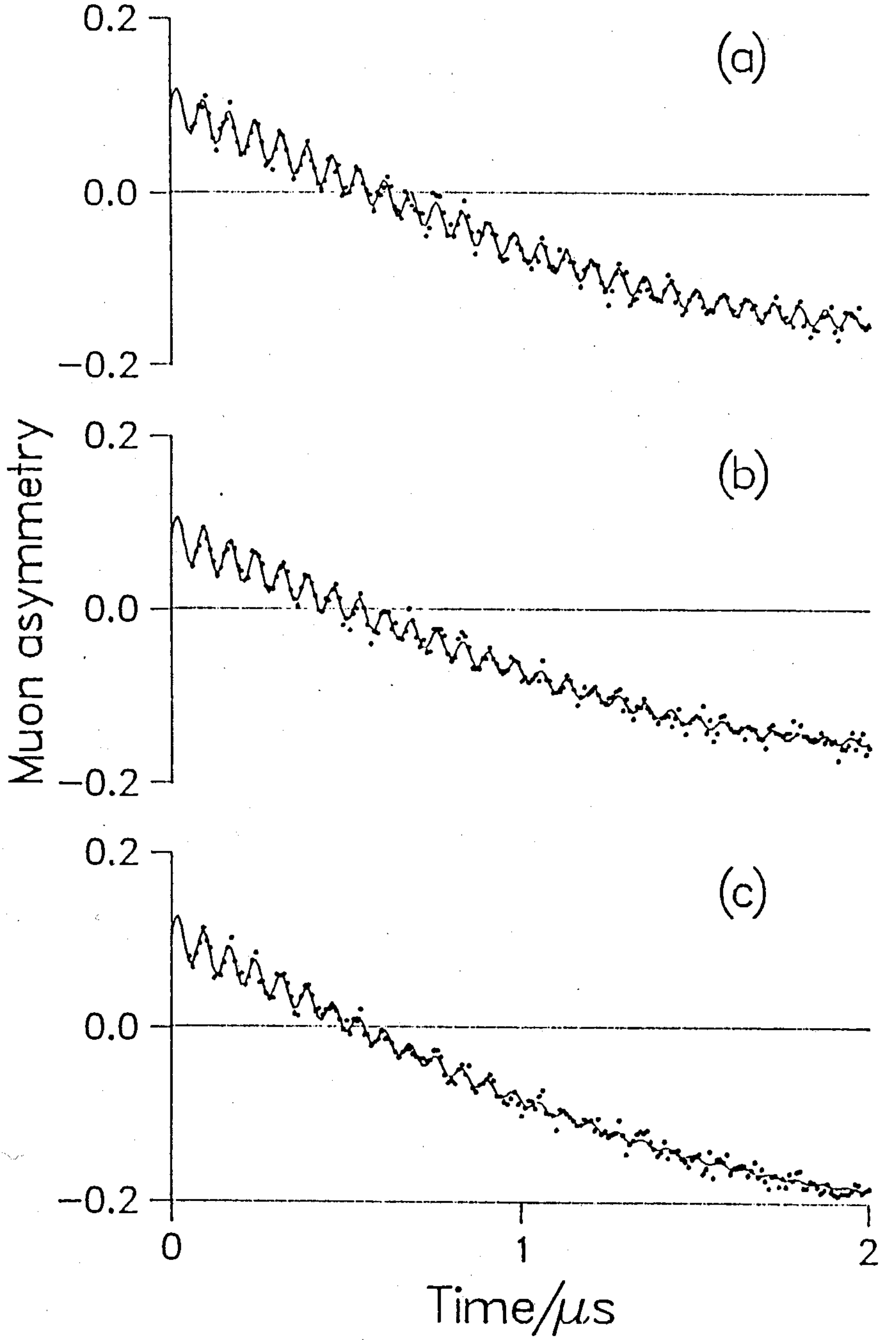

Figure 3-3. Muonium precession signals in (a) water, 1 bar (b) 0.29 mM $NaNO_3$, 1 bar (c) 0.29 mM $NaNO_3$ 2 kbar.

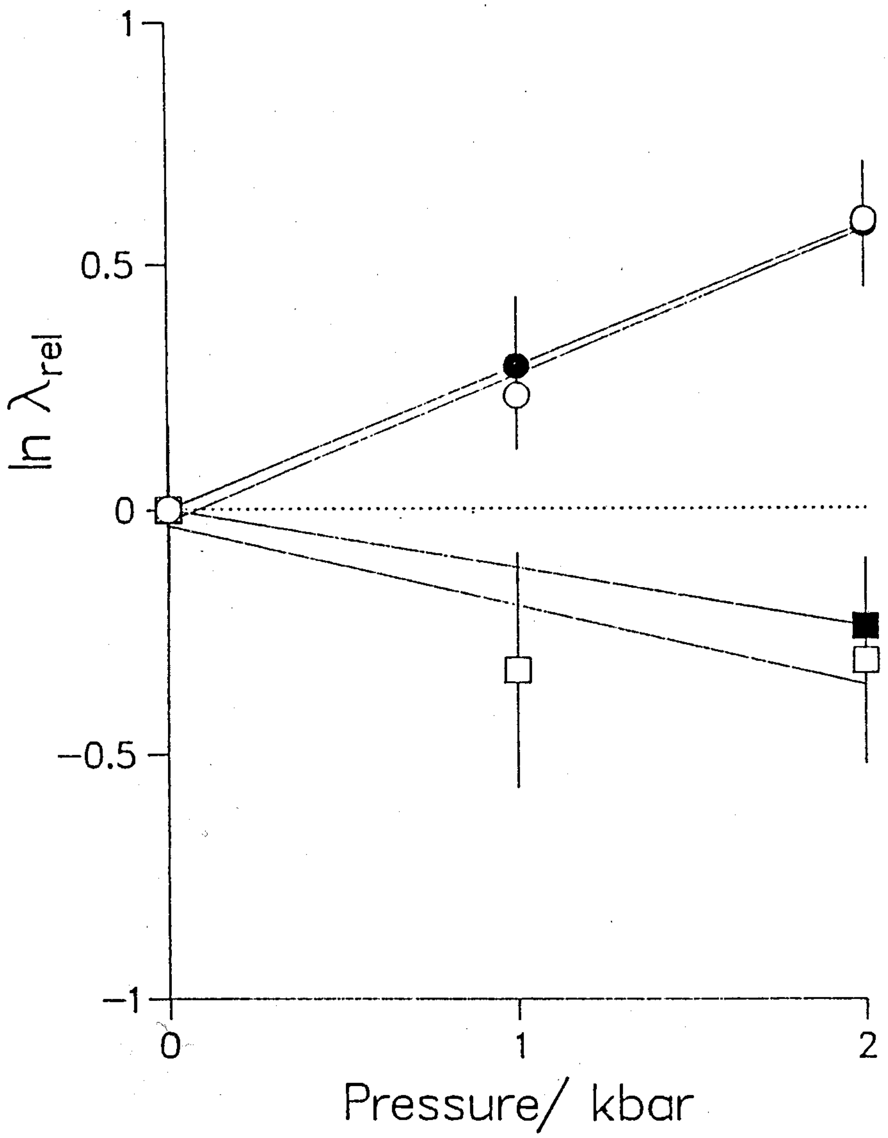

Figure 3-4. Pressure dependence of relative muonium reaction rates in aqueous solutions of sodium nitrate (o, 0.29 mM; •, 0.58 mM) and potassium permanganate (▫, 0.050 mM; ▪, 0.10 mM).

$$\bar{V}(\mathrm{Mu}) - \bar{V}(\mathrm{H}) = \Delta V^{\ddagger}(\mathrm{H}) - \Delta V^{\ddagger}(\mathrm{Mu}) = 2\ \mathrm{cm}^3\ \mathrm{mol}^{-1} \qquad (3.7)$$

If Mu and H atoms occupy cavities in liquid water in some non-interactive manner, without affecting the water structure, the partial molar volume represents the effective volume taken up by each atom. Equation (3.7) shows that in this case Mu is larger than H. Both atoms should have the same van der Waals radius, R_w, which for the free atom may be as large as 0.21 nm (one half of the internuclear distance at the potential minimum of $^3\Sigma_u^+$ H_2) [52], but muonium, being lighter, experiences greater quantum delocalization. An appropriate measure of the size of the atom could be [48]

$$R_{\mathrm{eff}} = (R_W^2 + 3L_T^2)^{\frac{1}{2}} \qquad (3.8)$$

where L_T is the thermal wavelength

$$L_T = \hbar/(mk_BT)^{\frac{1}{2}} \qquad (3.9)$$

and has values of 0.04 nm for H, 0.12 nm for Mu at room temperature. The calculated values of R_{eff} are 0.22 nm for H and 0.30 nm for Mu. These radii correspond to large volumes, 27 and 64 $\mathrm{cm}^3\ \mathrm{mol}^{-1}$, respectively. If a smaller value is chosen for R_w, the volume ratio becomes even larger. Clearly, the partial molar volumes are not good measures of the effective size of the atoms.

Since the partial molar quantities are so much smaller than the predicted volumes occupied by the atoms, there must be some compensating effect which reduces the volume occupied by solvent molecules. This phenomenon is known for the solvation of other non- and slightly polar molecules in water, and is termed hydrophobic hydration [53]. The molecular dynamics simulations performed by Klein *et al* are consistent with clathrate-like ordering of the nearest-neighbour water molecules around the H or Mu atom. The atomic radial distribution functions show distant peaks at O-H and O-Mu separations of 0.37 and 0.40 nm, respectively. The O-H distance is close to the sum of van der Waals radii of free H and water, indicating a near classical situation. The larger cavity occupied by Mu reflects the importance of quantum delocalization of the lighter particle. The sum of $R_{eff}(Mu)$ and $R_w(H_2O)$ is larger than the computed O-Mu separation, and it is this confinement of Mu that results in the expanded cavity. From the area under the radial distribution function Klein *et al* deduced that the clathrate cage around Mu contains 23 water molecules instead of the 18 around H. Thus, although the free volume available to Mu is almost 50% greater than for H, the ordering of the extra 5 water molecules almost compensates, with the result that the partial molar volumes are not very different.

CHAPTER FOUR

Theoretical Studies of Reactions
$H + H_2O_2$ and $Mu + H_2O_2$

The results of many studies indicate that the hydrogen atom reacts with hydrogen peroxide in two distinct ways (as illustrated in figure 4-1) [54-57]:

$$H + H_2O_2 \xrightarrow{k_a} H_2O + \cdot OH \qquad (4a)$$

$$H + H_2O_2 \xrightarrow{k_b} H_2 + \cdot OOH \qquad (4b)$$

The studies show little agreement on the absolute values of the rate constants k_a and k_b, or even which dominates at a particular temperature. Klemm *et al* found that k_a and k_b have markedly different temperature dependencies and $k_a >> k_b$ at room temperature [55]. But other works give $k_a/k_b = 1.86$ [56] and 1.3 [57].

As a light isotope of hydrogen, muonium is expected to undergo analogous reactions. The measurements of muonium decay rate for $Mu + H_2O_2$ in aqueous solutions were made by the SFU μSR group in 1984 [58]. The rate constant was determined to be 1.65×10^9 $M^{-1}s^{-1}$ at room temperature. The literature value of the

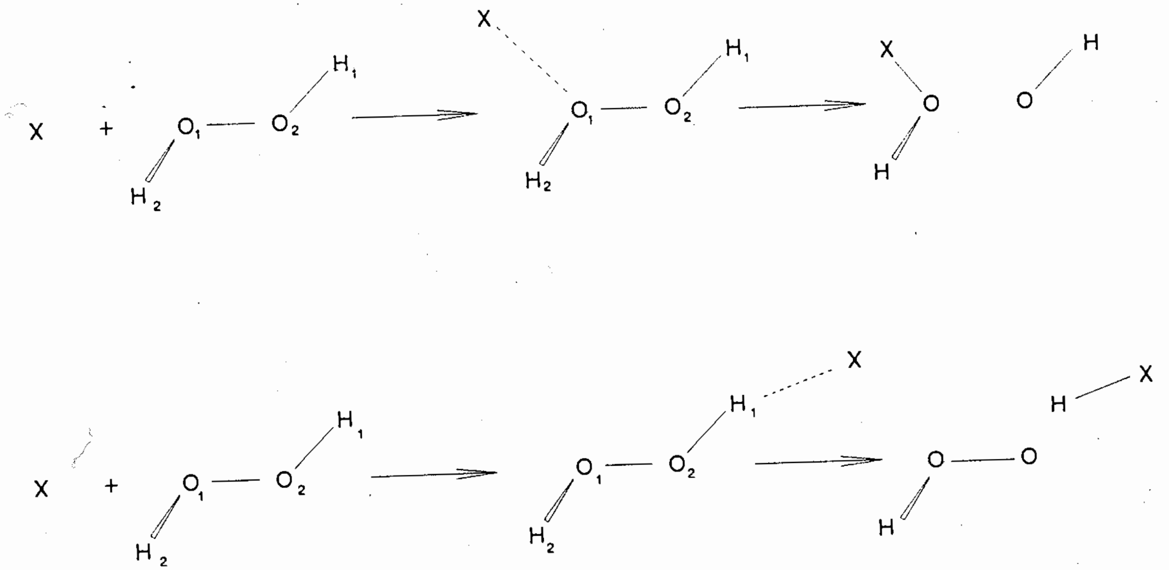

(4a)

(4b)

Figure 4-1. Schematic molecular arrangements for reactions (4a) and (4b), X = Mu or H.

rate constant for the H + H_2O_2 reaction in aqueous solution is 6×10^7 $M^{-1}s^{-1}$ [54]. These rate constants give a kinetic isotope effect of 27.5. With above information, a theoretical investigation of these reactions is desirable to provide tests of kinetic isotope effects. Semiempirical calculations were carried out in this study to approach the problem.

4.1. Theoretical background

4.1.1. Harmonic rate ratio

For a reaction between two substances A and B, the rate constant derived from transition state theory is given by [59]:

$$k = \kappa(C^{\ddagger}/C_A C_B)(kT/2\pi M^{\ddagger})^{\frac{1}{2}}/\delta \qquad (4.1)$$

where κ is the transmission coefficient and the C's are the concentrations of A, B and the transition state molecule, depending on the superscripts and subscripts (as a convention, superscript $\ddagger$ is reserved for the transition state). $M^{\ddagger}$ is the molecular weight of the transition state molecule and δ is a characteristic length at the top of the potential energy barrier for the reaction.

Without including the tunneling corrections, the ratio of the rate constants is given by [60,61]:

$$k_1/k_2 = \kappa_1 Q_1^{\ddagger}(M_2^{\ddagger})^{\frac{3}{2}}/\kappa_2 Q_2^{\ddagger}(M_1^{\ddagger})^{\frac{3}{2}} \tag{4.2}$$

where the subscripts 1 and 2 refer to the light and heavy isotopes. The Q's in equation (4.2) are the partition functions, and can usually be expressed as the product of translation, rotation and vibration partition functions [62]:

$$Q(\text{trans}) = (2\pi MkT)^{\frac{3}{2}}V/h^3 \tag{4.3}$$

$$Q(\text{rot}) = 8\pi^2(8\pi^3 XYZ)^{\frac{1}{2}}(kT)^{\frac{3}{2}}/sh^3 \tag{4.4}$$

and

$$Q(\text{vib}) = \sum_i \exp(\tfrac{1}{2}u_i)/[1-\exp(-u_i)] \tag{4.5}$$

In equations (4.3) to (4.5), V is the volume of the container and s stands for a symmetry number (the number of equivalent positions attainable by pure rotation), which is always equal to one for our systems. X, Y and Z are the moments of inertia corresponding to the three principal axes. The u's are dimensionless vibrational frequencies $u_i = h\nu_i/kT$, corresponding to the frequencies ν_i of the vibrational modes.

Substituting the partition functions defined by (4.3) to (4.5) into (4.2), the ratio of the rate constants obtained is called the harmonic rate ratio (HRR) [63]:

$$\mathrm{HRR} = (\kappa_1 s_1 s_2^{\ddagger}/\kappa_2 s_2 s_1^{\ddagger})(M_2 M_1^{\ddagger}/M_1 M_2^{\ddagger})^{\frac{3}{2}}$$

$$(X_2 Y_2 Z_2 X_1^{\ddagger} Y_1^{\ddagger} Z_1^{\ddagger}/X_1 Y_1 Z_1 X_2^{\ddagger} Y_2^{\ddagger} Z_2^{\ddagger})^{\frac{1}{2}} U^{\ddagger} U \qquad (4.6)$$

where $U^{\ddagger}$ and U relate to the vibrational partition functions and are given by:

$$U^{\ddagger} = \Pi_i \exp(\tfrac{1}{2}u_{i\,2}^{\ddagger})[1-\exp(-u_{i\,2}^{\ddagger})]/\exp(\tfrac{1}{2}u_{i\,1}^{\ddagger})[1-\exp(-u_{i\,1}^{\ddagger})] \qquad (4.7)$$

$$U = \Pi_i \exp(\tfrac{1}{2}u_{i\,1})[1-\exp(-u_{i\,1})]/\exp(\tfrac{1}{2}u_{i\,2})[1-\exp(-u_{i\,2})] \qquad (4.8)$$

For isotopically substituted molecules the Teller-Redlich product rule [64] holds, so that equation (4.6) reduces to:

$$\mathrm{HRR} = (s_1 s_2^{\ddagger} \nu_1^{\ddagger}/s_2 s_1^{\ddagger} \nu_2^{\ddagger}) U^{\ddagger} U \qquad (4.9)$$

where the $\nu^{\ddagger}$'s represent the imaginary frequencies corresponding to motion along the reaction coordinate. The ν's can be obtained by a standard procedure due to Wilson [65] and will be discussed in the next section.

4.1.2. Calculation of vibrational frequencies

The procedure used for calculating vibrational frequencies includes:

(1) Using MINDO/3 to calculate the structures, energies, and energy gradients for the reagents, transition states and products at several values of all geometric parameters.

(2) Finding the second derivatives of the energy with respect to each of the geometric parameters from the gradients by a numerical method. In this work, the second derivatives were determined by:

$$f''(x_0) = [f'(x_{-2}) - 8f'(x_{-1}) + 8f'(x_1) - f'(x_2)] \qquad (4.10)$$

where the positive and negative signs for the subscripts of x stand for both sides of the relevant point. The second derivatives of the energy are the elements of the force constant matrix **F** in the internal coordinate system.

(3) Constructing the kinetic matrix in the Cartesian coordinate system and transferring it to the internal coordinate system [66]. The kinetic matrix **T** in the Cartesian coordinate system is simply a diagonal matrix of the masses of the atoms, but it has a more complicated form in the internal coordinate

system. The translation between the two systems was performed using the **B** matrix, whose elements are given in appendix 4-B.

(4) Constructing the **G** matrix in the internal coordinate system as $\mathbf{G} = \mathbf{B}\mathbf{T}^{-1}\mathbf{B}'$ ($\mathbf{B}'$ is the transpose of **B**).

(5) Diagonalizing the matrix **GF** to obtain the vibrational frequencies (this was performed by the FORTRAN library routine F02AEF [67]).

(6) Calculating the HRR by using equation (4.9).

The MINDO/3 program was purchased from QCPE and run in double precision at SFU on the IBM 3081. A FORTRAN program ISOHRR was written to perform the above calculations. It was tested by reproducing the vibrational frequencies of H_2O and D_2O and the HRR for several reactions reported by Dewar *et al* [68,69] based on their MINDO/3 calculations.

4.1.3. Tunnelling corrections

It is well known in quantum mechanics that a small particle can exist in regions where classically it is excluded, that is, where its energy is less than the potential energy. In kinetics this means that such a particle may leak, or tunnel through a potential energy barrier, rather than pass over it. It is a consequence of the Heisenberg uncertainty principle and its importance in any given case may be gauged by calculating the de

Broglie wavelength

$$\lambda = h/mv \tag{4.11}$$

For a hydrogen atom traveling with a velocity of 2×10^{5} cm s^{-1}, the de Broglie wavelength is 2×10^{-8} cm. In a hydrogen bond, A-H--B, a typical value of the H--B distance would be 1.7×10^{-8} cm, which is comparable to the H atom de Broglie wavelength. Therefore, tunnelling is not negligible.

The tunnelling factor Q may be defined as [70]

$$Q = k_{obs}/k_{class} \tag{4.12}$$

where k_{class} is the expected rate constant in the absence of tunneling. To calculate Q it is necessary to assume some reasonable form for the potential energy function. The Schrödinger equation is then solved to give an expression for G(W), the probability of penetrating the barrier. This is a function of the energy W of the particle. Assuming a Boltzmann distribution over W, the averaged value of Q can be found by

$$Q = \int_0^\infty G(W)e^{-W/kT}dW/\int_E^\infty e^{-W/kT}dW$$

$$= e^{E/kT} \int_0^\infty G(W)e^{-W/kT}dW/kT \tag{4.13}$$

where E is the height of the energy barrier. The denominator of the first line of equation (4.13) has the classical value, $kTe^{-E/kT}$, which results from setting $G(W) = 0$ for $W < E$ and $G(W) = 1$ for $W \geq E$.

4.1.4. Eckart's 1-D potential and penetrating probability [71]

Eckart's 1-D potential function is given by

$$V = -Ay/(1-y) - By/(1-y)^2 \tag{4.14}$$

where $y = -\exp(2\pi x/L)$, x is the variable dimension, L is characteristic length related to $F^* = d^2V/dx^2$ at the potential maximum, $A = V_1 - V_2$ and $B = [V_1^{\frac{1}{2}} + V_2^{\frac{1}{2}}]^2$. V_1 is the activation energy of the reaction and V_2 is the energy difference between the saddle point and the products.

A particle of mass m and energy W approaching the barrier is characterized by the parameters ν^*, a_1 and a_2, defined as:

$$\nu^* = (-F^*/m)^{\frac{1}{2}}/2\pi \tag{4.15}$$

$$a_1 = 2\pi V_1/h\nu^* \tag{4.16}$$

$$a_2 = 2\pi V_2/h\nu^* \tag{4.17}$$

In these variables, the probability G(W) that a particle starting toward the barrier with energy W at $-\infty$ will pass the barrier and appear later at $+\infty$ with energy W is found by solving Schröedinger's equation for the Eckart function. The transmission probability is

$$G(W) = 1 - [\cosh(a-b)+\cosh(d)]/[\cosh(a+b)+\cosh(d)] \qquad (4.18)$$

where

$$a = 2(a_1\xi)^{\frac{1}{2}}/(a_1^{-\frac{1}{2}}+a_2^{-\frac{1}{2}}) \qquad (4.19)$$

$$b = 2[(1+\xi)a_1-a_2]^{\frac{1}{2}}/(a_1^{-\frac{1}{2}}+a_2^{-\frac{1}{2}}) \qquad (4.20)$$

$$d = 2(a_1a_2-\pi^2/4)^{\frac{1}{2}} \qquad (4.21)$$

with $\xi = W/V_1$.

4.2. Results

4.2.1. Structures of the reagents, transition states and products

The structures of the reagents and products for reactions (4a) and (4b) were obtained from energy minimization by using MINDO/3. Since only electronic energies are involved, the structures for muonium-substituted molecules are identical to those of unsubstituted ones. For the transition states of the reactions, the vibrational energies were included to locate the saddle points [72] and other corresponding parameters. Significant shifts of the transition states from the MINDO structures were found. The direction and extent of the shifts depended on the vibrational zero point energy (ZPE) of reagents, transition stated and products. For reaction (4a), the Mu-O bond length changed 0.1 nm and H-O 0.06 nm from the MINDO saddle point; for reaction (4b), the Mu-H bond length shifted 0.01 nm and H-H 0.2 nm. The calculated structures are reported in tables 4-1 and 4-2 in the standard way: the bond length refers to the distance between the first two nuclei from the right, the bond angle is formed by the first three atoms from the right and the twist angle is formed by all four atoms. The labelling of the atoms can be found in figure 4-1.

Table 4-1

Structures of the reagents, transition states (saddle point) and products of reaction (4a)

nuclei	bond length Å	bond angle degree	twist angle degree
Reagent: H_2O_2			
O(2)O(1)	1.380		
H(1)O(2)O(1)H(2)	0.9648	106.9	85.25
Transition states: MuH_2O_2 and HH_2O_2			
O(2)O(1)	1.384		
H(1)O(2)O(1)	0.9640	106.1	
H(2)O(1)O(2)H(1)	0.9656	106.5	85.70
Mu-O(1)O(2)H(1)	1.700	114.8	-169.7
O(2)O(1)	1.384		
H(1)O(2)O(1)	0.9641	106.2	
H(2)O(1)O(2)H(1)	0.9654	106.5	85.55
H-O(1)O(2)H(1)	1.740	115.2	-169.4
Product: XOH (X = H or Mu) and HO			
XOH	0.9487	103.8	
HO	0.9479		

Table 4-2
Structures of the reagents, transition states (saddle point) and products of reaction (4b)

nuclei	bond length Å	bond angle degree	twist angle degree
Reagent: H_2O_2, same as in table 4-1			
Transition states: MuH_2O_2 and HH_2O_2			
O(2)O(1)	1.363		
H(1)O(2)O(1)	1.025	109.6	
H(2)O(1)O(2)H(1)	0.9664	107.6	85.68
Mu-H(1)O(2)O(1)	0.990	168.4	-175.0
O(2)O(1)	1.381		
H(1)O(2)O(1)	0.9796	107.3	
H(2)O(1)O(2)H(1)	0.9650	107.0	83.84
H-H(1)O(2)O(1)	1.200	163.4	-162.2
Product: HOO and HX (X = H or Mu)			
OO	1.275		
HOO	0.9770	111.9	
HX	0.7466		

4.2.2. Vibrational frequencies and harmonic rate ratio

The vibrational frequencies needed for the HRR calculations were those of the transition states of (4a) and (4b). These were determined by the procedures described in 4.1.2. and are collected in table 4-3. The HRR defined by (4.9) are 0.79 for (4a) and 0.14 for (4b).

4.2.3. Tunnelling corrections and kinetic isotope effects

In order to obtain the tunnelling corrections defined in equations (4.12) and (4.13), the main characteristics of the the energy profiles along the reaction coordinates had to be determined. MINDO/3 was again used to provide the electronic energies and structures. The vibrational energies (ZPE) were then added, and the results are summarized in tables 4-4 and 4-5 and plotted in figure 4-2. The penetration probability as a function of energy G(W) was calculated as described in 4.2., and Q's were then calculated according to equation (4.13) by numerical integration, using the FORTRAN library routine D01AMF [67]. The result was Q(Mu)/Q(H) equal to 116 for reaction (4a) and 2.48×10^3 for reaction (4b). The KIE (kinetic isotope effect) were calculated to be 91.5 and 354 for reactions (4a) and (4b), respectively.

Table 4-3

Vibrational frequencies of the transition states of reactions (4a) and (4b) in cm^{-1}

(4a)		(4b)	
X = Mu	X = H	X = Mu	X = H
-2330	-771	-735	-740
363	280	434	257
780	354	879	359
1075	421	1065	506
1344	1323	1376	1278
1443	1428	1440	1409
1479	1470	1790	1472
3822	3821	3075	3108
3881	3873	3794	3862

Table 4-4
MINDO and vibrational energies of molecules in reactions (4a) and (4b) in kJ/mol

molecule	MINDO energy	ZPE	total energy
(4a)			
H_2O_2+H/Mu	85.89	73.49	159.4
MuH_2O_2	116.3	86.27	202.6
HH_2O_2	117.1	77.58	194.7
MuHO	-224.6	115.5	-109.1
H_2O	-224.6	57.54	-167.1
OH	70.67	24.06	94.7
(4b)			
H_2O_2+H/Mu	85.89	73.49	159.4
MuH_2O_2	120.3	82.84	203.1
HH_2O_2	118.2	73.27	191.5
HMu	0.551	68.04	68.59
H_2	0.551	30.18	30.73
HOO	-11.69	40.19	28.50

Table 4-5
Parameters of Eckart's 1-D potential for (4a) and (4b)

reaction	V_1[1]	V_2	
(4a)			
X = Mu	43.2	217.0	kJ/mol
X = H	35.3	267.1	kJ/mol
(4b)			
X = Mu	43.7	106.0	kJ/mol
X = H	32.1	132.3	kJ/mol

[1] V_1 is the activation energy of the reaction.

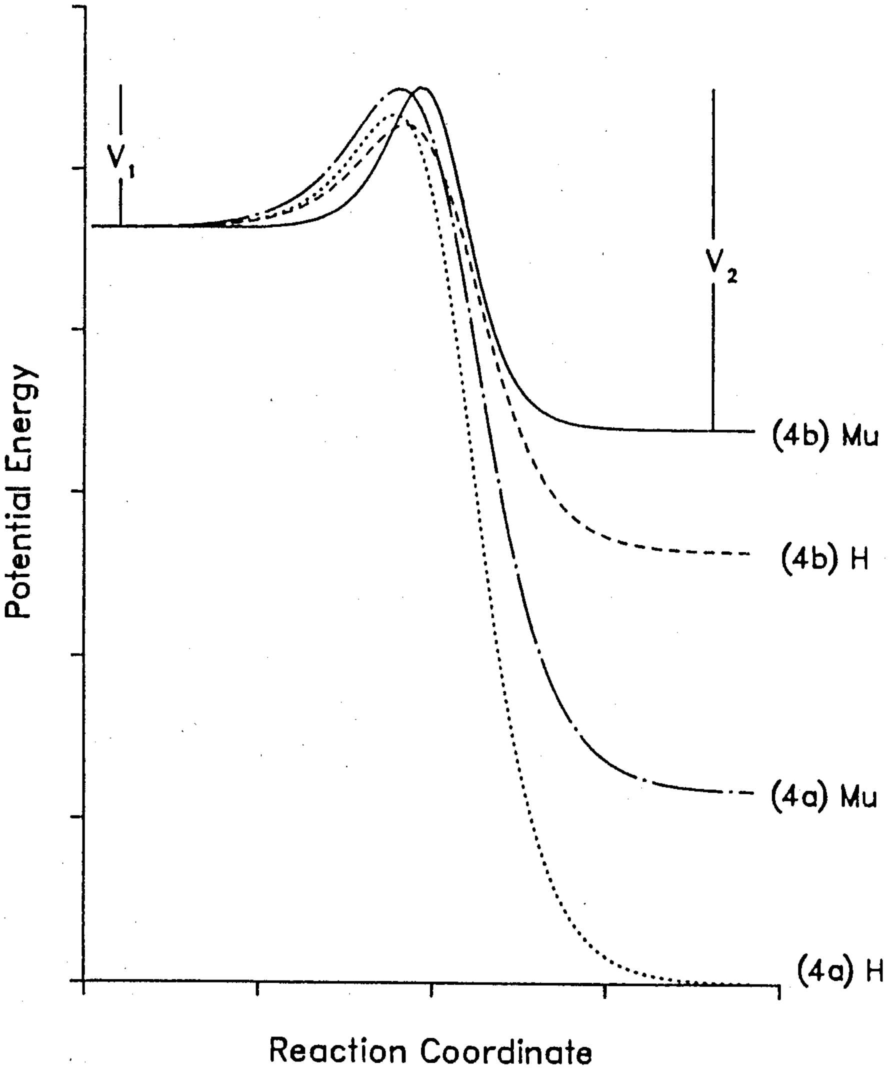

Figure 4-2. Potential energy profiles along reaction paths.

4.3. Discussion

As mentioned in the beginning of this chapter, the experimental KIE for reactions Mu + H_2O_2 and H + H_2O_2 is 27.5. The calculated results for both (4a) and (4b) predict a much higher KIE than the experimental value. This disagreement might be caused by the following reasons:

(1) MINDO/3, in common with other semiempirical programs based on the restricted Hartree-Fock method, has a weakness in dealing with radicals. The structures and energy profiles provided by MINDO/3 in this study may not be accurate enough.

(2) The tunnelling correction was calculated on the basis of an oversimplified 1-D Eckart potential function. Theoretical studies indicate that Q is very sensitive to the potential surface and a high quality energy profile is a must for correctly predicting tunnelling effects [73].

(3) The experimental observation was made in aqueous solution, but the calculation included no solvent effects.

APPENDIX 4-A

Self-Consistent-Field Method [74] and MINDO/3 Program [19]

Based on the variation principle [75] and earlier work by Hartree [76], Fock derived the well-known self-consistent-field (SCF) equation for molecular orbitals which has the Hartree-Fock hamiltonian operator as [77]:

$$f_i = H_{ii}^{core} + \sum_j (2J_{ij} - K_{ij}) \qquad (4a.1)$$

where H_{ij} is one electron operator and J_{ij} and K_{ij} are the Coulomb and exchange integration operators, respectively. The LCAO (linear combinations of atomic orbitals) approximation leads to the Roothaan equation [78]:

$$\sum_\nu (F_{\mu\nu} - \epsilon_i S_{\mu\nu}) C_{\nu i} = 0 \qquad (4a.2)$$

where the elements of the matrix representation of the Hartree-Fock hamiltonian operator are:

$$F_{\mu\nu} = H_{\mu\nu} + \sum_{\lambda\sigma} P_{\lambda\sigma}[(\mu\nu|\lambda\sigma) - \tfrac{1}{2}(\mu\lambda|\nu\sigma)] \qquad (4a.3)$$

with

$$H_{\mu\nu} = \int \phi_\mu(1) H^{core} \phi_\nu(1) dv_1 \qquad (4a.4)$$

$$H_p^{core} = -\tfrac{1}{2}\Delta - \sum_i Z_i / r_{ip} \qquad (4a.5)$$

$$P_{\mu\nu} = 2 \sum_i C^*_{\mu i} C_{\nu i} \qquad (4a.6)$$

$$(\mu\nu|\lambda\sigma) = \int\int \phi_\mu(1)\phi_\nu(1)(1/r_{12})\phi_\lambda(2)\phi_\sigma(2) dv_1 dv_2 \qquad (4a.7)$$

and

$$S_{\mu\nu} = \int \phi_\mu(1)\phi_\nu(1) dv_1 \qquad (4a.8)$$

To solve equation (4a.2) *ab initio*, one needs to evaluate the integrals defined by equations (4a.4), (4a.7) and (4a.8). The number of integrals is very large even for a small molecule, and consequently the method is not suitable for large molecules.

Different approximation methods have been developed to avoid the evaluation of many difficult integrals. Some make use of experimental data in selecting values for some of the integrals. In such semiempirical theory, one no longer attempts to derive molecular properties directly from the principles of quantum mechanics, but rather seeks to interpret correlations within experimental data.

The semiempirical method adopted in MINDO/3 is called INDO (intermediate neglect of differential overlap approximation) [79]. Its main features can be summarized as follows:

Approximation 1: Replacing the overlap matrix by the unit matrix in the Roothaan equations and neglecting the overlap integrals $S_{\mu\nu}$ in normalizing the molecular orbitals;

Approximation 2: Neglecting differential overlap in all two-electron integrals but retaining monoatomic differential overlaps if they are one-center integrals, so that

$$(\mu\nu|\lambda\sigma) = \delta_{\mu\nu}\delta_{\lambda\sigma}(\mu\mu|\lambda\lambda) \qquad (4a.9)$$

but

$$(\mu\nu|\mu\nu) = \int\int\phi_{\mu}(1)\phi_{\mu}(2)(1/r_{12})\phi_{\nu}(1)\phi_{\nu}(2)dv_1dv_2 \qquad (4a.10)$$

Approximation 3: Reducing the remaining set of coulomb-type integrals to one value per atom pair,

$$(\mu\mu|\lambda\lambda) = \gamma_{AB} \qquad \phi_{\mu} \text{ on A, } \phi_{\nu} \text{ on B} \qquad (4a.11)$$

Approximation 4: Neglecting monoatomic differential overlap in the interaction integrals involving the cores of other atoms

$$(\mu|V_B|\nu) = \delta_{\mu\nu}V_{AB} \tag{4a.12}$$

Approximation 5: Taking diatomic off-diagonal core matrix elements to be proportional to the corresponding overlap integrals, that is

$$H_{\mu\nu} = \beta_{AB}S_{\mu\nu} \qquad \phi_\mu \text{ on A, } \phi_\nu \text{ on B} \tag{4a.13}$$

The MINDO/3 program is one of the semiempirical routines developed by Dewar's group based on the INDO approximation. It calculates the geometry and energy of a molecule by minimizing the energy with respect to all geometrical parameters. The heat of atomization is found by subtracting the energies of the component atoms and it is then converted to heat of formation, according to the experimental values measured for gaseous atoms. The system is parameterized to handle H, B, C, N, O, F, Si, P, and Cl atoms. It is capable of handling up to fifty orbitals and has the option for open-shell calculations. In the testing process of MINDO/3 calculations were carried out for several hundred species, including neutral molecules, ions, radicals, carbenes, and triplet states [80-83]. The results show that MINDO/3 may provide a good overall quantitative guide to chemical behaviour while the cost of calculations is less by a factor of 10^6 than that of *ab initio* calculations.

APPENDIX 4-B

Definition of Elements of the B Matrix

(1) Stretching coordinates

Let $(x_i\ y_i\ z_i)$ be the coordinates of atom i in the Cartesian system and r_{ij} be the Mth internal coordinate being the length between atom i and j. Then the non-zero elements of row M of **B** are:

$B(M,3i-2) = -P_{ij}$,

$B(M,3i-1) = -Q_{ij}$,

$B(M,3i) = -R_{ij}$,

$B(M,3j-2) = P_{ij}$,

$B(M,3j-1) = Q_{ij}$,

$B(M,3j) = R_{ij}$

with

$P_{ij} = (x_j-x_i)/r_{ij}$,

$Q_{ij} = (y_j-y_i)/r_{ij}$,

$R_{ij} = (z_j-z_i)/r_{ij}$.

(2) Valence angle bending coordinates

Let α be the angle formed by atoms j, i and k. If it is the Mth coordinate in the internal coordinate system, then the non-zero elements of row M of **B** are:

$$B(M,3j-2) = (P_{ij}\cos\alpha - P_{ik})/r_{ij}\sin\alpha$$

$$B(M,3j-1) = (Q_{ij}\cos\alpha - Q_{ik})/r_{ij}\sin\alpha$$

$$B(M,3j) = (R_{ij}\cos\alpha - R_{ik})/r_{ij}\sin\alpha$$

$$B(M,3k-2) = (P_{ik}\cos\alpha - P_{ij})/r_{ik}\sin\alpha$$

$$B(M,3k-1) = (Q_{ik}\cos\alpha - Q_{ij})/r_{ik}\sin\alpha$$

$$B(M,3k) = (R_{ik}\cos\alpha - R_{ij})/r_{ik}\sin\alpha$$

$$B(M,3i-2) = -[B(M,3j-2) + B(M,3k-2)]$$

$$B(M,3i-1) = -[B(M,3j-1) + B(M,3k-1)]$$

$$B(M,3i) = -[B(M,3j) + B(M,3k)].$$

(3) Torsion angle coordinates

If atoms k, l, i and j form a torsion angle, and this angle is the Mth internal coordinate, there will be 12 non-zero elements for row M of **B** . With the definitions:

$$c_1 = r_{ik}\sin^2\alpha$$

$$c_2 = r_{ik}\sin^2\beta$$

$$c_3 = r_{kl}\cos\beta$$

$$c_4 = r_{ij}\cos\alpha$$

$c_5 = \cos\beta/c_2$

$c_6 = \cos\alpha/c_1$

$c_7 = r_{ij}c_1$

$c_8 = r_{kl}c_2$

the non-zero elements can be expressed as:

$B(M,3j-2) = (R_{ji}Q_{ik}-Q_{ji}R_{ik})/r_{ij}\sin^2\alpha$

$B(M,3j-1) = (P_{ji}R_{ik}-R_{ji}P_{ik})/r_{ij}\sin^2\alpha$

$B(M,3j) = (Q_{ji}P_{ik}-P_{ji}Q_{ik})/r_{ij}\sin^2\alpha$

$B(M,3l-2) = (R_{lk}Q_{ki}-Q_{lk}R_{ki})/r_{kl}\sin^2\beta$

$B(M,3l-1) = (P_{lk}R_{ki}-R_{lk}P_{ki})/r_{kl}\sin^2\beta$

$B(M,3l) = (Q_{lk}P_{ki}-P_{lk}Q_{ki})/r_{kl}\sin^2\beta$

$B(M,3i-2) = [r_{ik}-c_4(Q_{ji}R_{ik}-R_{ji}Q_{ik})]/c_7 - c_5(Q_{lk}R_{ki}-R_{lk}Q_{ki})$

$B(M,3i-1) = [r_{ik}-c_4(R_{ji}P_{ik}-P_{ji}R_{ik})]/c_7 - c_5(R_{lk}P_{ki}-P_{lk}R_{ki})$

$B(M,3i) = [r_{ik}-c_4(P_{ji}Q_{ik}-Q_{ji}P_{ik})]/c_7 - c_5(P_{lk}Q_{ki}-Q_{lk}P_{ki})$

$B(M,3k-2) = [r_{ki}-c_3(Q_{lk}R_{ki}-R_{lk}Q_{ki})]/c_8 - c_6(Q_{ji}R_{ik}-R_{ji}Q_{ik})$

$B(M,3k-1) = [r_{ki}-c_3(R_{lk}P_{ki}-P_{lk}R_{ki})]/c_8 - c_6(R_{ji}P_{ik}-P_{ji}R_{ik})$

$B(M,3k) = [r_{ki}-c_3(P_{lk}Q_{ki}-Q_{lk}P_{ki})]/c_8 - c_6(P_{ji}Q_{ik}-Q_{ji}P_{ik})$,

where α is the angle formed by atoms k, i and j, and β is the angle formed by atoms l, k and i.

CHAPTER FIVE

Intramolecular Motion of Muonium-Substituted Alkyl Radicals

5.1. Introduction

Free radicals isotopically substituted with a positive muon in place of a proton can be generated by stopping energetic muons in a target containing unsaturated organic compounds. Regardless of the specific reaction mechanism, muonium-substituted free radicals can be considered to be formed by addition of Mu to an unsaturated bond. Thus, Mu is initially one atom removed from the site of the unpaired electron. In chemical terminology, muonium is on the "beta" position to the radical centre. The beta proton hyperfine coupling constants (hfcc) in alkyl radicals obey the empirical relation [84]:

$$A = L + M\langle\cos^2\theta\rangle \tag{5.1}$$

where L and M are constants (M >> L) and θ is the dihedral angle between the axis of the p-orbital at C_α (which contains the unpaired electron) and the C_β-H bond. The observed coupling is a statistically weighted average over conformations with different θ. Temperature dependence of the coupling constant and the isotope effect on A when deuterons are substituted in the β-position have both been explained [85] in terms of different weighting of the conformers. Analogous arguments have been used to explain muonium hf frequencies in alkyl radicals [86]. Recently, however, it has been suggested [87] that hyperconjugation may be enhanced by muonium substitution, so that it is a change in the unpaired spin distribution that affects A by a change in M. μLCR spectroscopy is an ideal tool to distinguish between the two explanations of the isotope effect, because it can be used to measure the hfcc for both a proton and a muon substituted onto the same carbon. Any change in M would affect both substituents, whereas a preferred conformation which enhances the muon coupling would have the opposite effect on the proton coupling. With the interest of settling the question fully, the muon, proton and deuteron hfcc were determined for C_2H_4Mu, C_2D_4Mu and $(CH_3)_2CCH_2Mu$ radicals in this study.

The temperature dependence of β-hfcc carries information about intramolecular motion. Ramos *et al* [88,89] made a thorough study in muonium-substituted radicals. They measured muon hfcc as a function of temperature for C_2H_4Mu, $CHDMuCH_2$, CH_2MuCHD, CD_2MuCHD, $CHDMuCD_2$, and CD_2MuCD_2 and proton and deuteron hfcc (by ESR) in CH_2DCH_2 and CD_2HCD_2. The barrier to rotation was calculated for each radical. Muonium substitution has a dramatic effect: the barrier for CD_2MuCD_2 was found to be 3.45 kJ/mol compared with only 0.376 kJ/mol in CD_2HCD_2. A μLCR study of muonium-substituted ethyl (Mu-ethyl) should provide measurements of proton hfcc in the muonium substituted species. If a methyl group remains rigid as it rotates then the barrier experienced by H in the CH_2Mu group should be identical to that of Mu. The temperature dependence should be in the opposite direction, however, so that the mean β-hfcc, $\bar{A}(CH_2Mu) = \frac{1}{3}(2A_p + A'_\mu)$, ($A'_\mu = 0.314\ A_\mu$, scaled by a factor γ_p/γ_μ for direct comparison between muon and proton hfcc) is constant. Also, the proton hfcc of the unsubstituted methyl group, $A(CH_3)$ is expected to be temperature independent. The latter two tests have already been done by Ramos *et al*, but only for CH_2DCH_2, where the temperature dependence is much less than in the muonium-substituted species.

Although simple alkyl radicals are commonly held to have a planar configurations at the trigonal carbon [90], the most recent theoretical and experimental investigations conclude that only the methyl radical is planar, and that all other simple alkyls exhibit deviations from planarity in their lowest energy geometries [91,92]. The structure of t-butyl has been an interesting subject for both theoretical and experimental studies [93-96]. The experimental evidence for a pyramidal configuration includes photoelectron [95] and infrared [96] spectral data, but a controversy was centered on the interpretation of the ESR data [97,98]. Particularly important is the temperature dependence of the ^{13}C hfcc (A_C) of the C_α, which is expected to be positive for a planar species. In fact,

A_C was found to fall with temperature [99], go through a broad minimum around 220 K and then rise [98]. This is consistent with pyramidal inversion in a shallow double-well potential [100], with at least three vibrational levels below the barrier to inversion, which was estimated to be about 2 kJ/mol above the minimum [98]. Independent calculations [93,94] confirmed the pyramidal nature of the t-butyl radical but challenged the concept of a simple double-minimum potential curve for inversion. It was found that the torsional modes of the methyl group are strongly coupled to the low-frequency inversion mode, and the lowest energy path to inversion involves simultaneous rotation of the methyl group to optimize the interactions between the β C-H bonds and the radical center. Further theoretical work [101,102] has explored this coupling, and barriers to the concerted rotation-inversion have been variously estimated to be 5-7 kJ/mol, according to basis set and type of motion [93,94,101,102]. The calculated pyramidal angle varies from 7.4° to 19.5° [94,100]. Percival *et al* studied the muonium-substituted t-butyl (Mu-t-butyl) using μSR and μLCR spectroscopy [103]. They found that the average β-hfcc $\bar{A}(CH_2Mu)$ is significantly larger than $A(CH_3)$ and that the latter is very close to the value measured by ESR for t-butyl [104,105]. This suggests that the muonium-substitution in one methyl group has little effect on the others. In view of the interest in both the isotope effect and the internal dynamics of the radical, the hfcc of muon, proton and ^{13}C were determined over a wide range of temperature in this work.

5.2. Muonium-substituted ethyl radical

The muonium-substituted ethyl (Mu-ethyl) radical can be formed by addition of muonium to ethene, *e.g.*,

$$Mu + H_2C{=}CH_2 \rightarrow H_2\dot{C}{-}CH_2Mu \tag{5.2}$$

The rate constant for reaction (5.2) is 4.0×10^{9} M^{-1} s^{-1} so that it is suitable for μLCR study.

5.2.1. Experimental

Both μSR and μLCR measurements were made over a temperature range 20 to 300 K covering the solid, liquid and gas phases of ethene. The gas-phase targets were prepared by Dr. Fleming's μSR group of University of British Columbia as a collaboration. A variety of gas sample cells was used in the course of this study, reflecting the conflicting requirements of different technical considerations. The cells were cylindrical in shape, with a stainless steel or aluminium body and a Mylar window at one end. The cell length varied from 5 to 20 cm and window thickness from 0.1 to 0.5 mm. A long cell accommodates the extended stopping distribution of muons in low pressure gas, but a short cell has the advantage of good field homogeneity. A thick window is necessary for high pressure samples and can act as a degrader to shorten the muon stopping distance; disadvantages include muon stops in the window and an increase in range straggling and scattering. Early versions of the sample cell had no provision for temperature control, so measurements were subject to diurnal variation of room temperature. Subsequently, fluid from a constant-temperature bath was circulated through copper coils attached to the outside of the cell.

The liquid target (same for solid) was prepared at the experimental area. The ethene gas was condensed into a pre-cooled cell inside a helium-cooled cryostat. The temperatures were also controlled using the cryostat system.

5.2.2. Results

Measurements with the gas target were made at pressures from 1 to 14 atm for C_2H_4, 12 and 16 atm for C_2D_4 and at about 2.7 atm for $^{13}C_2H_4$. The muon momentum was adjusted according to gas pressure and window thickness, typically 27.8 MeV/c with 5% bite. Table 5-1 collects the results measured from the gas target of ethene at room temperature. The measurements show no systematic variation of A_μ or μLCR proton fields with C_2H_4 pressure as evidence of table 5-1. The spread of results is consistent with a temperature variation of 18 - 23 $^{\circ}$C during the period of the experiments. Table 5-2 lists the results from

Table 5-1

Muon hfcc and μLCR fields of Mu-ethyl at ~ 300 K

pressure/atm	A_μ/MHz	α-H resonance/kG	β-H resonance/kG
13.6	331.8(4)	14.129(8)	
10.8	331.1(1)	14.131(6)	21.133(2)
5.5	330.4(4)	14.129(3)	21.137(1)
2.8	331.6(1)	14.137(3)	21.149(1)
1.0	331.4(4)	14.140(7)	21.147(4)

statistical errors in parentheses on the last figure

Table 5-2

Hfcc (in MHz) of $C_2H_4Mu/^{13}C_2H_4Mu$, C_2D_4Mu and C_2H_5 at ~ 300 K

	This work		ESR [106,107][1]
	$C_2H_4Mu/^{13}C_2H_4Mu$	C_2D_4Mu	$C_2H_5/^{13}C_2H_5$
C_α	113.1(4)		109.5
C_β	-38.8(4)		-38.1
X_α[2]	-63.4(4)	-63.2(32)[3]	-62.7
X_β	66.8(4)	63.8(19)[3]	75.3
Mu	103.6(1)/104.1(1)[4]	106.9(1)[4]	
$(2X_\beta+Mu)/3$	79.1/79.2	78.2	

[1] at 193 K

[2] X = H or D

[3] Scaled by a factor 6.514 = γ_p/γ_d

[4] Scaled by a factor 0.314 = γ_p/γ_μ

measurements at 10 atm and 25 °C (temperature-regulated), where they are compared with ESR data for C_2H_5 [106,107]. Muon and proton hfcc at different temperatures are collected in tables 5-3 and 5-4. The muon hfcc are consistent with literature values [89,108].

5.2.3. Theoretical treatment of the experimental results

For simple alkyl radicals the major component of the unpaired electron spin density derives from the $2p_z$ orbital centered at the α-carbon nucleus [90]. As shown in figure 5-1, let θ be the dihedral angle for a particular substituent X, then the equilibrium conformation of the radical can be specified by θ_0, the value of θ at the minimum of the potential for internal rotation about the C_β-C_α axis. Assuming that the internal rotation of the CR'RX group about the C_β-C_α internuclear axis can be treated as independent from the vibrational motion, molecular rotation and solvent interaction, the torsional Hamiltonian $H(\theta)$ is then simply given by

$$H(\theta) = -(\hbar^2/2I)d^2/d\theta^2 + V(\theta) \tag{5.3}$$

where $V(\theta)$ is the rotational potential and I, the reduced moment of inertia, is defined as

$$I = I_1 I_2/(I_1 + I_2) \tag{5.4}$$

Table 5-3

Muon hfcc of Mu-ethyl determined from μSR spectra

Temp./K	A_μ/MHz[1]	A'_μ/MHz
20.0	482.0	151.4
60.0	459.0	144.2
93.6	430.1	135.1
109.0	417.4	131.1
124.5	405.2	127.3
138.5	395.9	124.4
153.4	385.8	121.2
300.0	331.3	104.1

[1] typical uncertainty 0.4 MHz

Table 5-4

μLCR fields and proton hfcc of Mu-ethyl

	CH_2		CH_2Mu	
Temp./K	B_0/kG[1]	A_p/MHz[2]	B_0/kG[1]	A_p/MHz[2]
60.0			22.113	49.6
93.6			20.360	53.2
109.0	25.719	-61.99	19.361	55.83
124.5	25.080	-62.21	18.633	57.25
138.5	24.580	-62.27	18.060	58.56
153.4	24.047	-62.34	17.456	59.80
300.0	21.141	-62.64	14.138	67.13

[1] uncertainty is less than 1 unit of the last digit

[2] uncertainty is about 0.4 MHz, dominated by that of A_μ

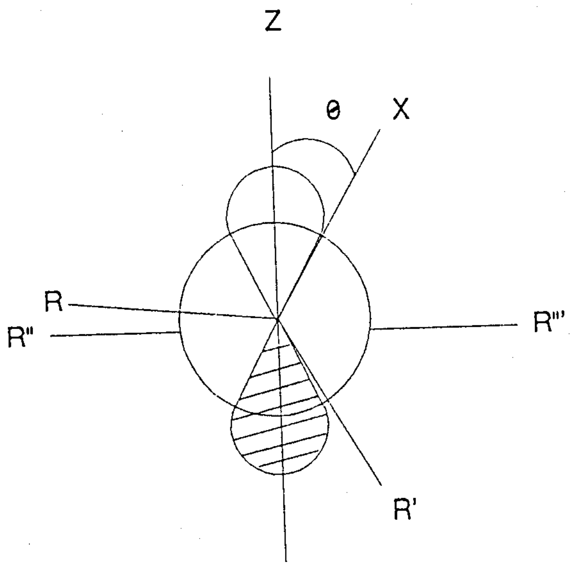

Figure 5-1: Schematic diagram showing the $2p_z$ orbital at the α-carbon and the definition of the dihedral angle for alkyl radicals.

in terms of the moments of inertia I_1 and I_2 for the two groups rotating about the C_β-C_α axis evaluated at the equilibrium molecular geometry.

If there exists a Boltzmann population of the torsional energy levels E_i, the temperature dependence of the β-hfcc of alkyl radical will follow

$$A_\beta(T) = \sum_i \langle A(\gamma)\rangle_i \exp(-E_i/kT)/\sum_i \exp(-E_i/kT) \tag{5.5}$$

where $\gamma = \theta + \theta_0$ and $\langle A(\gamma)\rangle_i$ is the expectation value of the β-hfcc for the molecule in the ith torsional state. Measurements of the hfcc at different temperatures can be used to derive information on radical conformations and intramolecular potentials.

For Mu-ethyl X = Mu and R = R' = R" = R'" = H in figure 5-1. From the consideration of symmetry, a two-fold potential is expected which can be defined by

$$V(\theta) = \tfrac{1}{2}V_2(1 - \cos 2\theta) \tag{5.6}$$

This barrier can also be considered as a truncation of a Fourier series for $V(\theta)$ with only the two-fold term being retained. The Hamiltonian defined by equation (5.3) with potential (5.6) can be employed to calculate the torsional energy levels and the corresponding eigenfunctions. The hfcc can then be calculated from equation (5.5).

The angular dependence of the β-proton-electron hf interaction and β-deuteron-electron interaction are often represented by equation (5.1). The leading constant L in equation (5.1) represents a contribution to the hf interaction arising from a spin polarization mechanism and the second constant M is due to hyperconjugation. M is usually much larger than L, and typically takes the value 140 MHz for proton coupling in alkyl radicals. Such a relationship is also suitable for β-muon-electron hf interactions [88]. For occupancy of the ith torsional level the expectation value $A_\beta(\gamma)$ can be evaluated from

$$A_\beta(\gamma) = L + M\langle i|\cos^2\gamma|i\rangle \tag{5.7}$$

Adopting the wavefunction constructed from a linear combination of free rotor states

$$\Psi_j = \sum_n C_n \exp(in\theta),$$

$$n = 0, \pm 1, \pm 2, \cdots \pm\infty, \; j=1, 2, \cdots 2n_{max}+1 \tag{5.8}$$

the expectation value in (5.7) can be rewritten as

$$\langle i|\cos^2\gamma|i\rangle = \tfrac{1}{2}\sum_n C_n[C_n + \tfrac{1}{2}C_{n+2}(\cos2\theta_0-\sin2\theta_0)$$

$$+ \tfrac{1}{2}C_{n-2}(\cos2\theta_0+\sin2\theta_0)] \qquad (5.9)$$

The coefficients $\{C_n\}$ are obtained by solution of the secular problem using the Hamiltonian given by (5.3) and (5.6). The secular determinant then has the elements defined by

$$\begin{aligned} H_{nn} &= \hbar^2n^2/2I + \tfrac{1}{2}V_2 & & \\ H_{nk} &= -V_2/4 & \text{for } k &= n\pm2 \qquad (5.10) \\ H_{nk} &= 0 & \text{for } k &\neq n\pm2. \end{aligned}$$

A FORTRAN program FCN.V2 was written for a least-squares fit of equation (5.5) to the experimental data. The fits were performed using a basis of 21 free rotor states ($n_{max} = 10$ in equation (5.8)) after checking the convergence of the calculations for different numbers of wavefunctions. Two different fits were carried out. In the first one, four parameters L, M, θ_0(H) and V_2, the barrier to internal rotation, were allowed to vary simultaneously in the calculations. In the second, different values of L and M were used for Mu and H. The fit parameters are listed in table 5-5 and the calculated hfcc are collected in table 5-6 and plotted in figure 5-2. The good agreement between calculated and experimental hfcc shows the above treatment is applicable.

Table 5-5

Best fit parameters for the analysis of the temperature dependence of hfcc for Mu-ethyl assuming a V_2 potential

Fit 1	V_2	3.1 kJ/mol
	L	-13 MHz
	M	183 MHz
	θ_0(H)	122°
	θ_0(Mu)	0° (fixed)
Fit 2	V_2	2.8 kJ/mol
	L(Mu)	-16 MHz
	M(Mu)	192 MHz
	L(H)	-15 MHz
	M(H)	185 MHz
	θ_0(H)	122°
	θ_0(Mu)	0° (fixed)

Table 5-6

Comparison of experimental data and calculated values from the best fits (hfcc in MHz)

Temp./K	A'_μ(exp)	A'_μ(Fit 1)	A'_μ(Fit 2)
109.0	131.11	130.86	131.07
124.5	127.29	127.37	127.33
138.5	124.35	124.43	124.25
153.4	121.20	121.56	121.30
300.0	104.08	104.05	104.08
	A_p(exp)	A_p(Fit 1)	A_p(Fit 2)
109.0	55.83	55.78	55.72
124.5	57.25	57.28	57.30
138.5	58.56	58.54	58.60
153.4	59.80	59.76	59.85
300.0	67.13	67.25	67.13

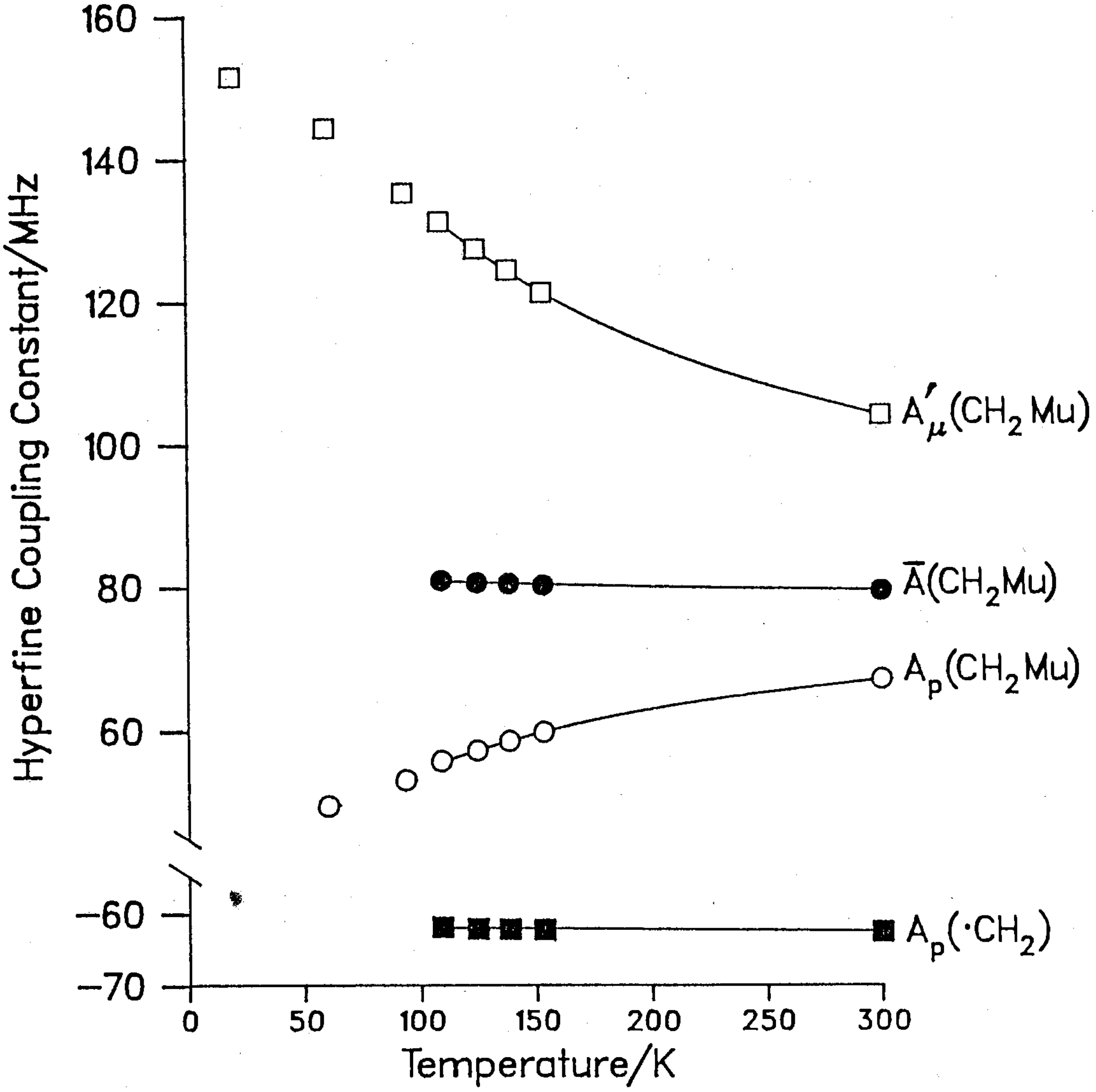

Figure 5-2. Temperature dependence of the muon and proton hyperfine coupling constants in Mu-ethyl radical. The solid lines represents the best fits (Fit 2) of the experimental values (points).

5.2.4. Discussion

The decrease of the muon hfcc with increase in temperature suggests that the C-Mu bond eclipses the p_z orbital of the α-carbon in the preferred conformation at low temperature, as shown in figure 5-3. This could arise from enhanced hyperconjugation or it could be a steric effect. Both relate to a longer C-Mu bond than the corresponding C-H bond [109-113]. The longer bond for C-Mu than C-H is a result of the displacement of the mean nuclear separation for the zero-point energy levels in an anharmonic potential, as shown in figure 5-4. Roduner [113] used a diatomic Morse potential to calculate average bond lengths of 1.141 Å for C-H and 1.197 Å for C-Mu, an increase of 4.9%. This makes a weaker C-Mu bond than C-H bond and a bound Mu is effectively larger than a bound H. The preferred conformation of the n-propyl radical has been shown experimentally (ESR) [104,114] to be that with the β-methyl substituent lying in or close to the radical plane. This favours the argument that conformational control normally depends on more efficient hyperconjugative electron release from a C-Mu bond over a C-H bond. Most primary alkyl radicals prefer the in-plane conformation (eclipsed). That the sizes of the β-alkyl substituent cause relatively small changes in this preference [90] supports this argument.

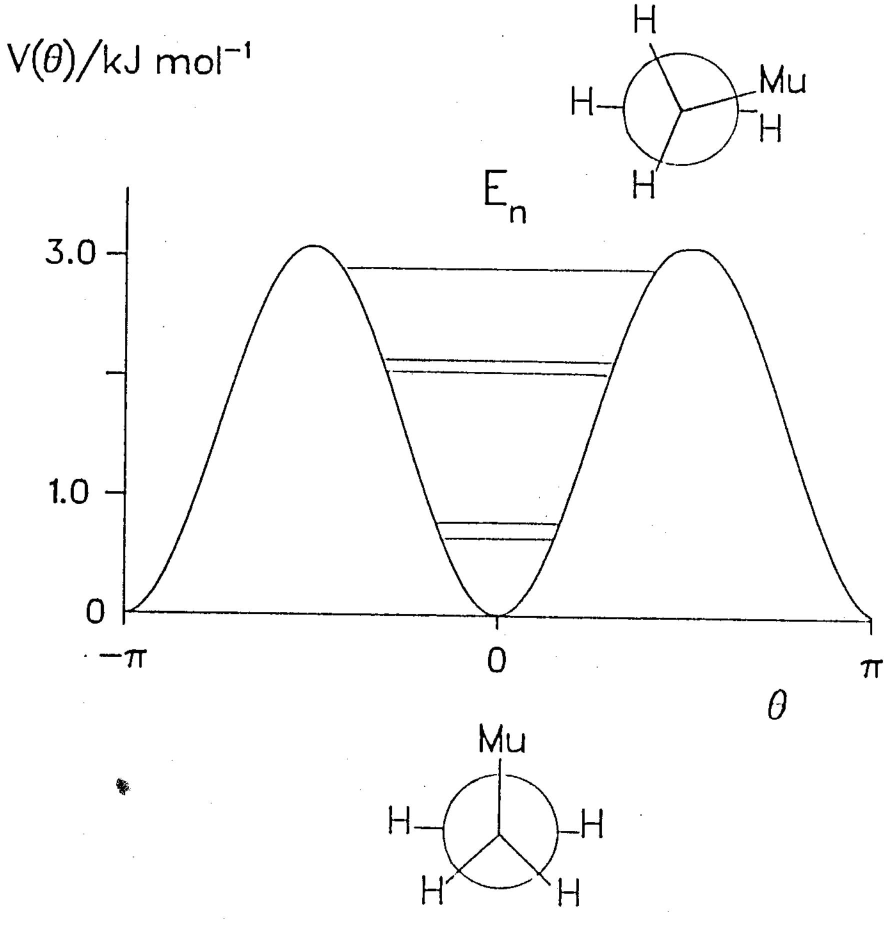

Figure 5-3. V_2 potential and energy levels of Mu-ethyl.

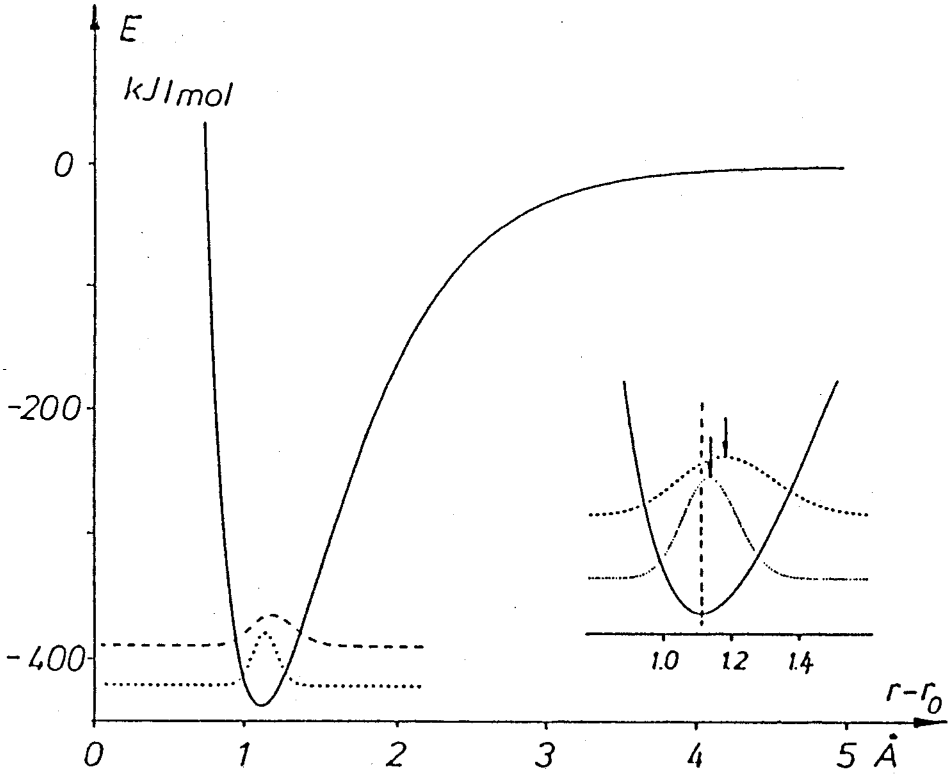

Figure 5-4: Ground state vibrational wavefunction ($|\Psi|^2$) for a diatomic C-H and C-Mu fragment in a Morse potential [113].

A'_μ is considerably larger than A_p, in keeping with the general principle that in the minimum energy conformation the lighter isotope eclipses the orbital containing the unpaired electron. At sufficiently high temperature in the "free rotation" limit, $<\cos^2\theta> = \frac{1}{2}$ and is isotope independent. The unsubstituted methyl group should give the free rotation value of $L + \frac{1}{2}M$ at all temperatures [114], as should $\bar{A}(CH_2Mu)$ in the absence of any isotope effect on L and M. In fact, the results in table 5-2 show that $\bar{A}(CH_2Mu)$ = 79.1 MHz is significantly greater than the methyl proton hfcc, $A(CH_3)$ = 75.3 MHz in CH_2CH_3 [115], confirming the existence of the so-called "residual" isotope effect (The residual isotope effect represents the hfcc difference between isotopically substituted groups caused other than the preferred conformations). This is consistent with the hyperconjugation effect. The hyperconjugation will increase the muon coupling for all conformations even when rotational preferences have been quenched at high temperature. The increased C-Mu bond length should promote enhanced hyperconjugation and thereby affect the values of L and M in equation (5.1). This has been found in the calculations as reported in table 5-5.

Ab initio calculation of CH_2CH_3 gave a barrier of 0.63 kJ/mol for methyl rotation [91] while the value of V_2 for Mu-ethyl is 3.1 kJ/mol. This indicates a strong isotope effect on the rotation barrier. By diagonalization of the Hamiltonian matrix discussed in 5.2.3., 5 energy levels below the barrier were obtained for both fit 1 and fit 2. For example, the energies of these levels for fit 1 are 0.739, 0.744, 2.04, 2.14 and 2.93 kJ/mol, respectively, as shown in figure 5-3.

Using the calculated MINDO/3 equilibrium structure of ethyl, the moment of inertia of the CH_2 group is $I_1 = 2.78\text{x}10^{-47}$ kgm^2, and that of the CH_2Mu group is $I_2 = 3.69\text{x}10^{-47}$ kgm^2. From equation (5.4), the reduced moment of inertia is $I = 1.59\text{x}10^{-47}$ kgm^2. Various fits were carried out with I as a variable parameter to include any possible change in geometry. These fits showed that the hfcc and other parameters are not sensitive to I, as found by others [88,89].

The hfcc of Mu-ethyl in frozen ethene followed the same trend as in the gas and liquid phases. The μLCR spectra were asymmetric, as shown in figure 5-5, indicating an anisotropic hfcc. Accurate analysis of the spectra is still under way and is not included in this thesis.

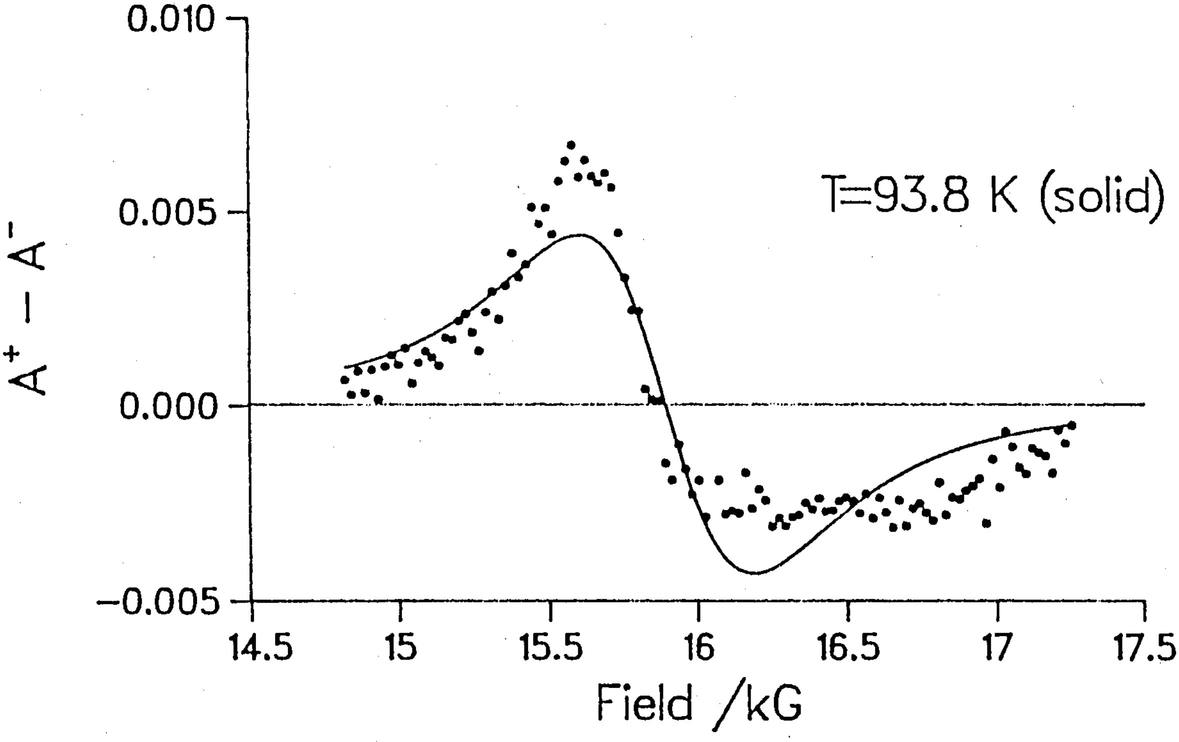

Figure 5-5. μLCR spectrum of frozen Mu-ethyl radical.

5.3. Muonium-substituted t-butyl radicals

5.3.1. Muon and proton hyperfine coupling constants in Mu-t-butyl

5.3.1.1. Experimental and results

Measurements of muon and proton hfcc in Mu-t-butyl covered a temperature range of 40 K to 300 K. As isobutene has a low boiling point (266.2 K), it was mixed (50:50) with dodecane (b.p. 489.5 K) for high temperature measurements. The samples were degassed by the freeze-pump-thaw method. The temperature was controlled with either the helium-cooled cryostat system, for lower temperatures, or the circulator, for higher temperatures. For frozen isobutene the μLCR with $\Delta(m_\mu + m_k) = 1$ (see section 1.5.2.) was observed. The μSR and μLCR results are collected in tables 5-7 to 5-9.

5.3.1.2. Theoretical treatment

The principles used in the analysis of the experimental data are the same as described in section 5.2. The temperature dependence of hfcc of the muon and protons is to be interpreted in terms of methyl rotation. As the molecule is more complicated, so is the potential profile. Rotation of an unsubstituted methyl group should generate a three-fold or six-fold potential, according to the symmetry at C_α. It is

Table 5-7

Muon hfcc for Mu-t-butyl in the liquid phase determined from μSR spectra

Temp./K	A_μ/MHz	A'_μ/MHz
140.7	361.30(10)	113.49
155.0	349.39(6)	109.75
169.1	340.08(6)	106.83
202.0	321.72(6)	101.06
227.2	311.21(10)	97.76
259.0	300.24(10)	94.31
289.0	291.70(13)	91.63
297.1	289.52(16)	90.95

Table 5-8

μLCR fields and proton hfcc for Mu-t-butyl in the liquid phase

	CH_3		CH_2Mu		
Temp./K	B_0/kG	A_p/MHz	B_0/kG	A_p/MHz	$\bar{A}$/MHz
140.7	16.002	62.37	16.877	46.16	68.60
155.0	15.331	62.62	16.133	48.11	68.66
169.1	14.833	63.00	15.571	49.28	68.46
202.0	13.844	63.04	14.455	51.72	68.17
227.2	13.278	63.09	13.816	53.12	68.00
259.0	12.684	63.20	13.146	54.64	67.86
289.0	12.233	63.08	12.641	55.52	67.56
297.1	12.141	62.98	12.534	55.33	67.20

Table 5-9

Muon hfcc determined from $\Delta M = 1$ μLCR fields for $(CH_3)_2CCH_2Mu$ in frozen solution

Temp./K	B_0/kG	A_μ/MHz	A'_μ/MHz
43.10	18.17	495.0	155.5
52.00	17.96	489.2	153.7
61.50	17.70	482.2	151.5
80.90	17.01	463.4	145.6
102.50	16.07	437.8	137.5
109.90	15.89	432.8	136.0
118.50	15.45	420.4	132.2
128.50	15.04	409.7	128.7

therefore reasonable to predict a function for a substituted methyl that has:

$$V(\theta) = \tfrac{1}{2}V_2(1 - \cos 2\theta) + \tfrac{1}{2}V_3(1 - \cos 3\theta) \tag{5.11}$$

or

$$V(\theta) = \tfrac{1}{2}V_2(1 - \cos 2\theta) + \tfrac{1}{2}V_6(1 - \cos 6\theta) \tag{5.12}$$

Various shapes of potential have been explored. The fit results are reported in tables 5-10 to 5-12 and plotted in figures 5-6 and 5-7. In these fits, the moment of inertia was obtained from the structure calculated by Pacansky *et al* (restricted open-shell Hartree-Fock method) [102]. For the $C(CH_3)_2$ group $I_1 = 9.48 \times 10^{-46}$ kgm² and for the CH_2Mu group $I_2 = 3.63 \times 10^{-46}$ kgm². From equation (5.4) $I = 3.50 \times 10^{-46}$ kgm². Again it was found that the fits were not sensitive to I.

5.3.1.3. Discussion

The most distinctive feature of the results is the discontinuity in A_μ at the melting point of isobutene. Since the variation of hfcc with temperature arises from the change in occupancy of the various torsional or vibrational states in the radical, the sudden change on freezing suggests that interaction with the lattice in the solid influences the distribution of

Table 5-10

Best fit parameters for the analysis of the temperature dependence of hfcc for Mu-t-butyl assuming a V_2 potential

	liquid	solid	
V_2	2.1	3.4	kJ/mol
L	-53	-63	MHz
M	237	242	MHz
θ_0(H)	122°	120°	(fixed)

Table 5-11

Representative fits to the temperature dependence of hfcc of the CH_2Mu group in Mu-t-butyl in liquid solution

	I	II	III	IV	
V_2	2.1	2.5	1.78	1.77	kJ/mol
V_3	-	2.8	-	-	kJ/mol
L(Mu)	-53	-33	-68	-69	MHz
M(Mu)	237	200	271	273	MHz
L(H)	[1]	[1]	-46	0	MHz
M(H)	[1]	[1]	223	131	MHz
θ_0(H)	122	122	120[2]	105[2]	°

[1] same as for Mu

[2] fixed

Table 5-12

Comparison of experimental data and calculated values for fit IV

Temp./K	A'_μ/MHz		A_p/MHz	
	expt.	calc.	expt.	calc.
140.7	113.49	113.42	46.16	46.55
155.0	109.75	109.84	48.11	48.03
169.1	106.83	106.79	49.28	49.28
202.0	101.06	101.07	51.72	51.64
227.2	97.76	97.68	53.13	53.04
259.0	94.31	94.26	54.64	54.46
289.0	91.63	91.67	55.52	55.54
297.1	90.95	91.06	55.33	55.79

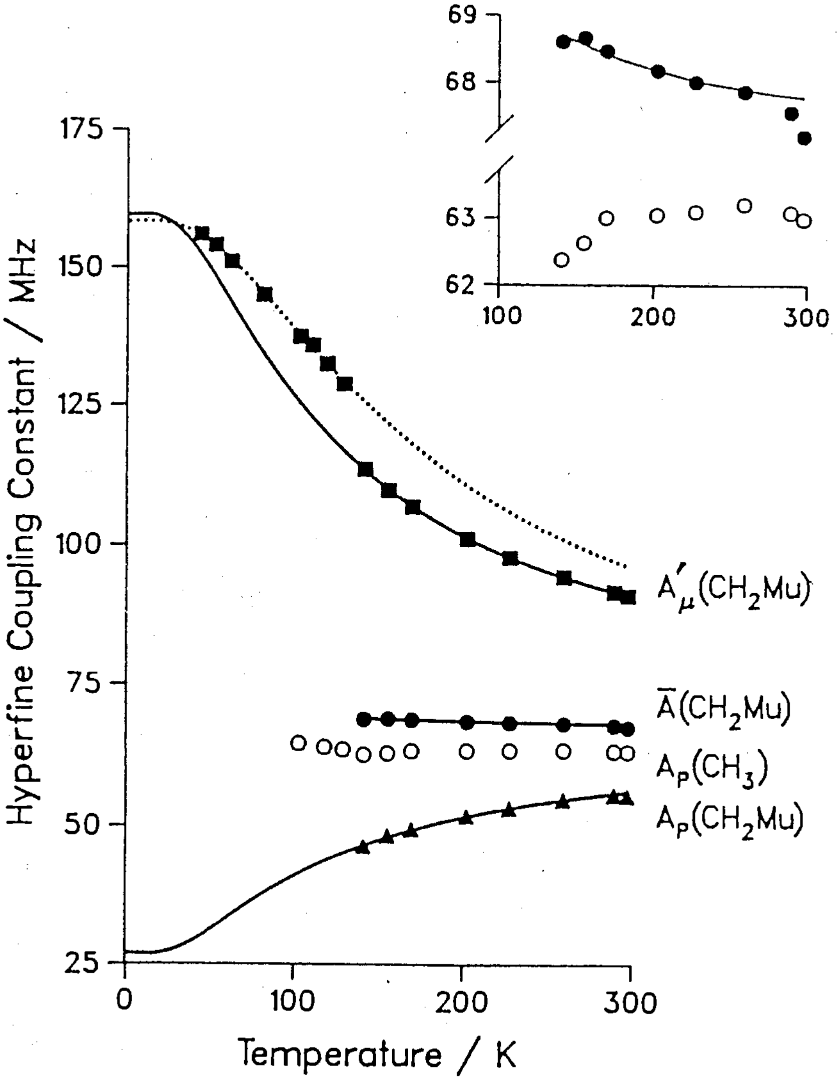

Figure 5-6. hfcc in $(CH_3)_2CCH_2Mu$. The solid lines correspond to fit I for the liquid solution data, the dotted line to the frozen solution.

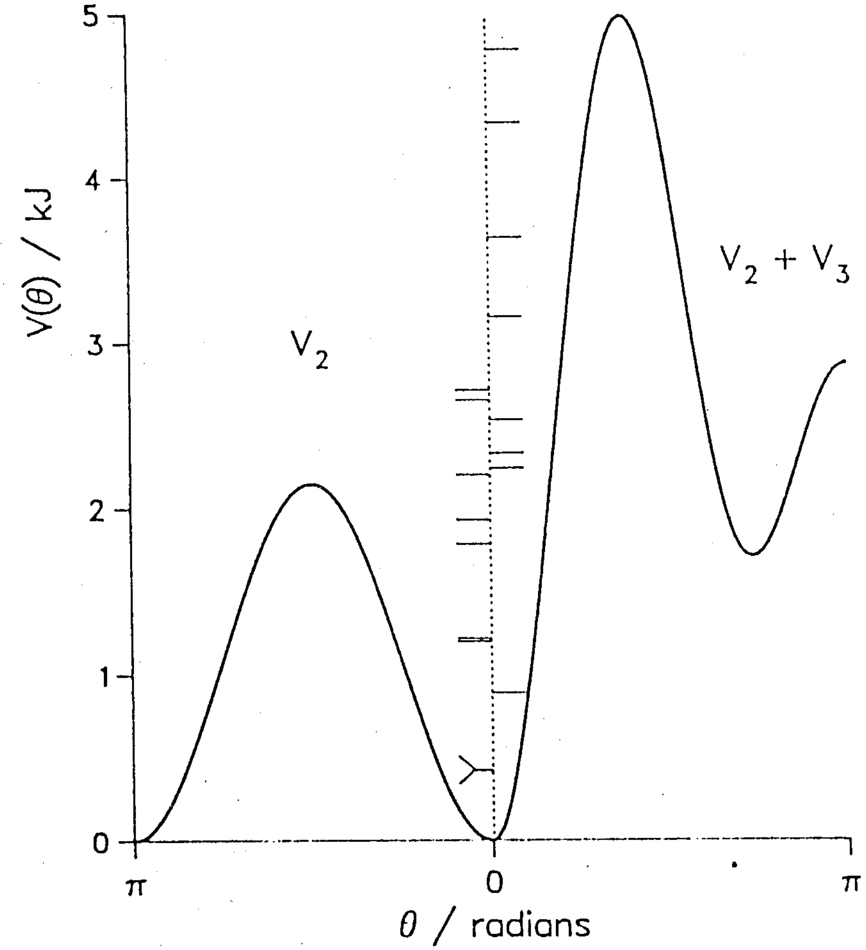

Figure 5-7. Comparison of V_2 and V_2 + V_3 potentials used to fit the temperature dependence of the hfcc of $(CH_3)_2CCH_2Mu$ in the liquid phase. The horizontal lines denote the calculated torsional energy levels.

motional states. It is significant that analysis using a V_2 potential gives almost the same extrapolated value for A_μ at 0 K. Thus, the minimum energy structure is identical for the solid and liquid states, only the temperature dependence changes. The analysis shows that there is a higher barrier for CH_2Mu rotation in the solid. This suggests that methyl rotation in the liquid phase is facilitated by simultaneous inversion of the carbon skeleton, but that the inversion mode is somewhat inhibited in the solid. The infrared spectrum of tert-butyl is consistent with a C_{3v} structure, and since the inversion has not been detected, it is assumed to have a frequency below 200 cm^{-1} [96]. If the pyramidal structure was entirely frozen in the solid, the V_1 or V_1+V_3 potentials should be used (see equations (5.11) and (5.12)) in the analysis, and the potential barrier determined under the assumption of a V_2 potential (reported in table 5-10) would be in error. However, the qualitative argument remains valid, namely that the minimum energy structure is common to the solid and liquid phases, and that the barrier to methyl rotation is higher in the solid.

With a C_{3v} structure for the methyl group, the rotation of the protons in the methyl group makes them all equivalent and their hfcc should be essentially temperature independent as shown in table 5-8. The muonium-substitution breaks the C_{3v} symmetry. The average β-hfcc $\overline{A}(CH_2Mu)$ as in table 5-8, has a value of 67.2 MHz (at 297 K) which is larger than $A_t(CH_3)$ = 63.7

MHz [114], the hfcc of the unsubstituted t-butyl, so there is clearly an isotope effect. Extrapolation of fit IV to high temperature limiting values gives 71.0 MHz and 64.5 MHz for A'_μ and $A(CH_2)$, respectively. Similarly to Mu-ethyl, there exists a residual isotope effect. It is significant that the high temperature limit for $A(CH_3)$ in Mu-t-butyl is close to $A_t(CH_3)$ in t-butyl. This suggests that the C-H bond length is not much affected by the neighbouring Mu, and that usual values of L(H) and M(H) should apply. It is generally accepted in the ESR literature that L is negligibly small compared to M. By adding this constraint to the fits, $\theta_0(H)$ is deduced to be significantly less than 120°, as shown by fit IV in table 5-11 .

An additional factor that could affect L(Mu) and M(Mu) is distortion from tetrahedral geometry at C_β. Other studies have suggested [90,104] that β-methyl groups in simple alkyl radicals tilt towards the radical centre as shown in figure 5-8, so that the C_3 symmetry axis of the methyl group is no longer collinear with the C_α-C_β bond. More recently, *ab initio* calculations [93] have shown that each methyl group in tert-butyl has one long C-H bond trans to the radical orbital on the pyramidal central carbon. It seems reasonable that the intrinsically "weaker" C-Mu bond would enhance this effect, and this could result in a larger tilt of the C-Mu bond towards the radical orbital. This type of distortion would reduce $\theta_0(H)$ from its standard value of 120°.

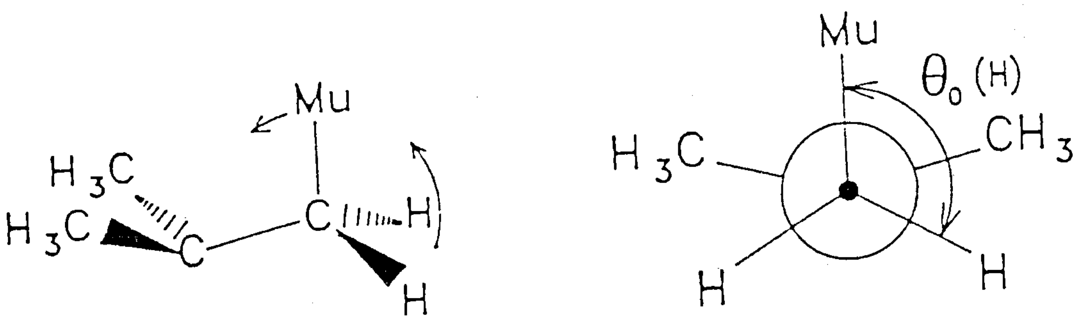

Figure 5-8. Schematic representation of $(CH_3)_2CCH_2Mu$ showing the pyramidal distortion at C_α and tilting of the methyl group.

Another, more subtle effect of isotopic substitution can be seen in the difference in the trends of $\bar{A}(CH_2Mu)$ and $A(CH_3)$. The former falls monotonically with temperature, while the latter rises at first, goes through a broad maximum, and finally drops off at the highest temperatures measured. A similar broad maximum in $A_t(CH_3)$ was found by Wood *et al* [97,99] for unsubstituted t-butyl together with a corresponding minimum for the α-C hfcc, and these were interpreted as the effects of out-of-plane vibrations at the radical centre. The drop in $\bar{A}(CH_2Mu)$ with temperature is also found for the average methyl hfcc in CH_2DCH_2 [88], and is presumably due to reduced hyperconjugation at increased amplitudes of the C-H (C-Mu) bending vibration. A similar argument will be proposed to explain the temperature dependence of the methylene group hfcc in muonium-substituted cyclohexadienyl in chapter six.

Finally, it should noted that the simple $\cos^2\theta$ angular dependence expressed in equation (5.1) is inadequate to describe the effects of distortion at C_β or inversion at C_α. Furthermore, if methyl rotation is indeed coupled to inversion, then the motional coordinate along the path of least energy may not be directly proportional to θ, again bringing into question the validity of (5.1). In retrospect, it is surprising that the data were fitted so closely. Apparently these factors introduce only subtle deviations, and are consequently only amenable to study with high quality data.

5.3.2. ^{13}C hyperfine coupling constants in Mu-t-butyl

The temperature dependence of the central carbon (C_α) hfcc is ideal for the study of out-of-plane bending of alkyl radicals [117]. By using a simple double-minimum potential [100], the vibrational energy of the distortion can be represented by:

$$V(x) = V_0(x^4 - 2x^2) \tag{5.13}$$

where x equals δ/δ_0 and δ is the angle between the plane of the methyl carbon atoms and a C-C bond. According to the 'classical' theory of the double-minimum potential the temperature dependence of ^{13}C hfcc is given by [117]

$$A_C(T) = A_0[\rho_0 + \rho_2\delta_0^2F_2(T,V_0) + \rho_4\delta_0^4F_4(T,V_0)] \tag{5.14}$$

where $F_n(T,V_0)$ =

$$\int_0^\infty \xi^n \exp[-V_0(\xi^4-2\xi^2)/kT]d\xi / \int_0^\infty \exp[-V_0(\xi^4-2\xi^2)/kT]d\xi \tag{5.15}$$

and

$$\rho(\delta) = \rho_0 + \rho_2\delta^2 + \rho_4\delta^4 \tag{5.16}$$

A_0 is the atomic scale factor which relates the spin density at the central carbon, $\rho(\delta)$, to A_C. The constants ρ_0, ρ_2 and ρ_4 in equation (5.16) are usually obtained from calculations, by investigating the relation between the spin density and angle δ.

5.3.2.1. Experimental and results

A dilute solution of ^{13}C labeled isobutene in isopentane was used for the experiments in order to reduce the cost of the sample. μLCR measurements were carried out for a temperature range 125 K to 300 K (a dodecane mixed solution was used for high temperature measurements). It is impossible to measure the muon hfcc by μSR as the radical formation rate in the diluted solution is too slow. The muon hfcc were derived from those in pure isobutene, by using a quadratic fit to 3 nearby temperature points. Based on these muon hfcc and measured μLCR fields the ^{13}C hfcc were determined. Table 5-13 collects the muon and ^{13}C hfcc. Figure 5-9 shows the temperature dependence of the ^{13}C hfcc. The minimum of ^{13}C hfcc lies around 250 K which is close to 259 K, near the maximum in $A(CH_3)$.

5.3.2.2. Data analysis and discussion

The temperature dependence of the ^{13}C hfcc for Mu-t-butyl were analysed using the double-well potential model. For unsubstituted t-butyl, Griller *et al* used the INDO method to compute $\rho(\delta)$ for $\delta \leq 30^\circ$. Fitting equation (5.16) to calculated

Table 5-13

μLCR fields and hfcc of $^{13}C_\alpha$ of Mu-t-butyl

Temp./K	B_0/kG	A_μ/MHz	A_C/MHz
125.4	9.769	374.77	128.62
150.2	8.985	353.34	126.87
196.2	7.887	324.62	125.69
248.5	7.054	303.63	125.60
279.4	6.683	294.34	125.61
299.4	6.473	289.35	125.89

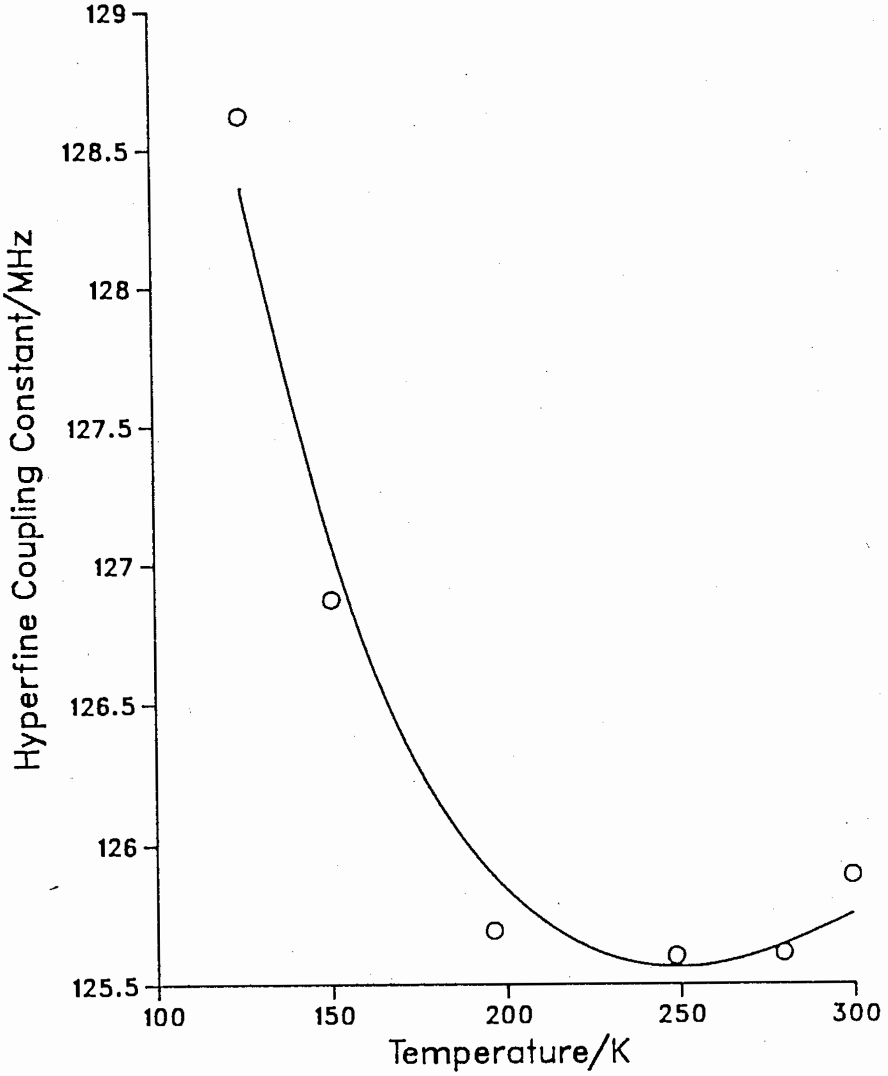

Figure 5-9. Experimental (points) and calculated (solid line) hyperfine coupling constants of ^{13}C in t-butyl.

values of $\rho(\delta)$, they obtained the constants $\rho_0 = 0.04151$, $\rho_2 = 0.84552$, and $\rho_4 = -1.16246$ [117]. As Mu substitution in the β position will introduce little change to the spin density on the α carbon, the same constants ρ_0, ρ_2 and ρ_4 were taken for Mu-t-butyl (In fact, none of the semiemipirical programs distinguish between isotopes as only the electronic interactions are considered). The calculated ^{13}C hfcc are also plotted in figure 5-9. The fitted parameters A_0, δ_0 and V_0 are reported in table 5-14 and the double-well potential is plotted in figure 5-10.

The values of V_0 in table 5-14 seem to suggest that muonium-substitution has little effect on the inversion barrier. But it should be noted that this barrier corresponds to a much larger inversion angle ($\delta_0 = 19.3^0$) than that of t-butyl ($\delta_0 = 11.5^0$) [117]. An alternative fit with fixed $\delta = 11.5^0$ gave $V_0 = 2.46$ kJ/mol, which is larger than that for t-butyl.

That the out-of-plane bending is more pronounced for the Mu-t-butyl is consistent with the earlier discussion in section 5.3.1.3.

A quite different A_0 was found for Mu-t-butyl compared with that of the t-butyl. This factor as it was defined in [100], depends on the reduced mass for the inversion vibration. In the empirical formulas (5.14), it is a scale factor relating the spin density and hfcc of C_α. As discussed earlier, the spin

Table 5-14

Best fit parameters for the analysis of the temperature dependence of ^{13}C hfcc for Mu-t-butyl

	This work	t-butyl [117]	
A_0	1193	1845	MHz
δ_0	19.3	11.5	o
V_0	1.77	1.88	kJ/mol

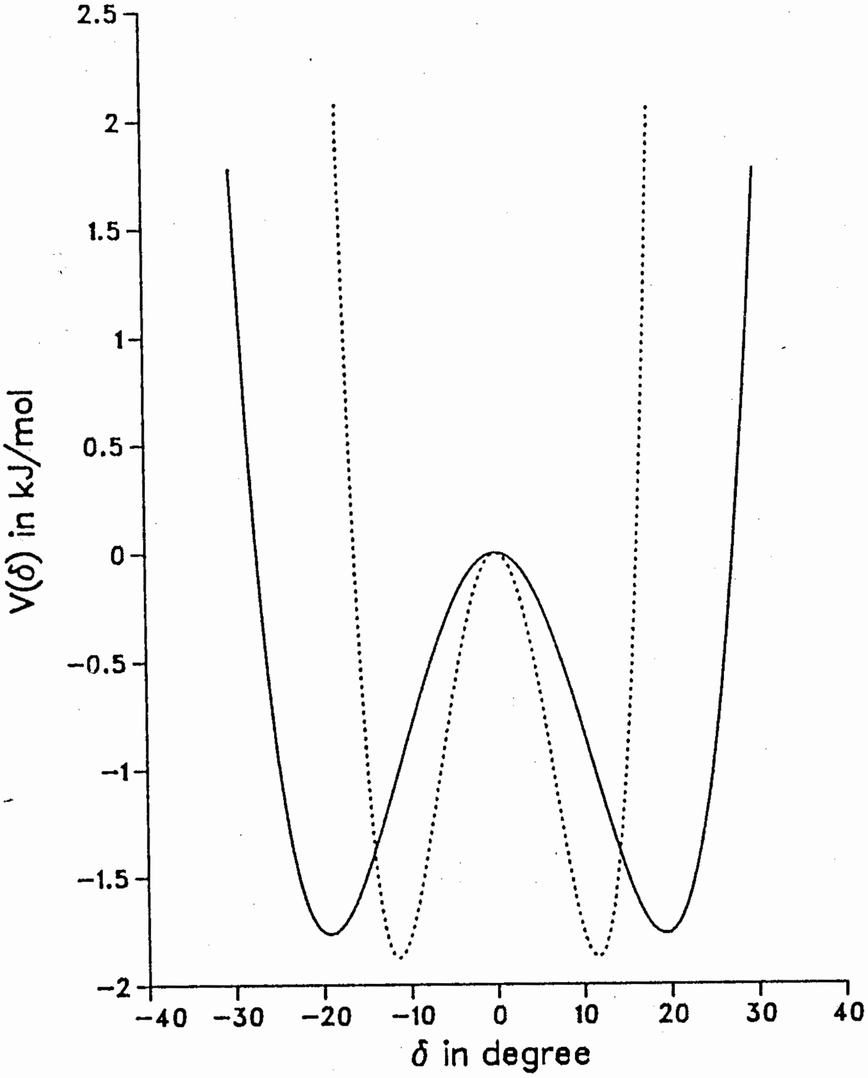

Figure 5-10. Double-well potential of δ in Mu-t-butyl (solid line) and t-butyl (dotted line).

distributions for t-butyl and Mu-t-butyl should be essentially the same, as should the A_0's. The different A_0's are also related to the change of δ_0. The fit with fixed $\delta = 11.5^0$ gives a value of A_0, 1852 MHz, which is the same as that for t-butyl.

CHAPTER SIX

Structure and Intramolecular Motion of Muonium-Substituted Cyclohexadienyl Radicals

6.1. Introduction

The electronic structure of the cyclohexadienyl radical has been the subject of considerable theoretical and experimental investigation over the past 25 years [118-129]. Interest was centred on the anomalously high hfcc of the methylene protons and the possible deformation of the equilibrium structure by out-of-plane deviation of the C(6)-methylene group (see figure 6-1 for the definition of the ring positions). Both these matters are related to the extent of interaction of the cyclopentadienyl π system with the C(6)-X(6) σ bonds (X = H, D, F etc.) and several theoretical models and semiempirical formulae have been derived on this aspect [124-126].

In attempting to apply a similar equation to (5.1) to cyclohexadienyls, Kira *et al* [126] used the well-known Heller-McConnell equation [84] in connection with Whiffen's consideration (the methylene proton hfcc should not be compared with the sum of unpaired spin densities on the ortho carbons, $\rho_1 + \rho_5$, but instead to the square of the sum of the relevant π orbital coefficients, *i.e.* $(c_1 + c_5)^2$, where $c^2 = \rho$) [127]. They

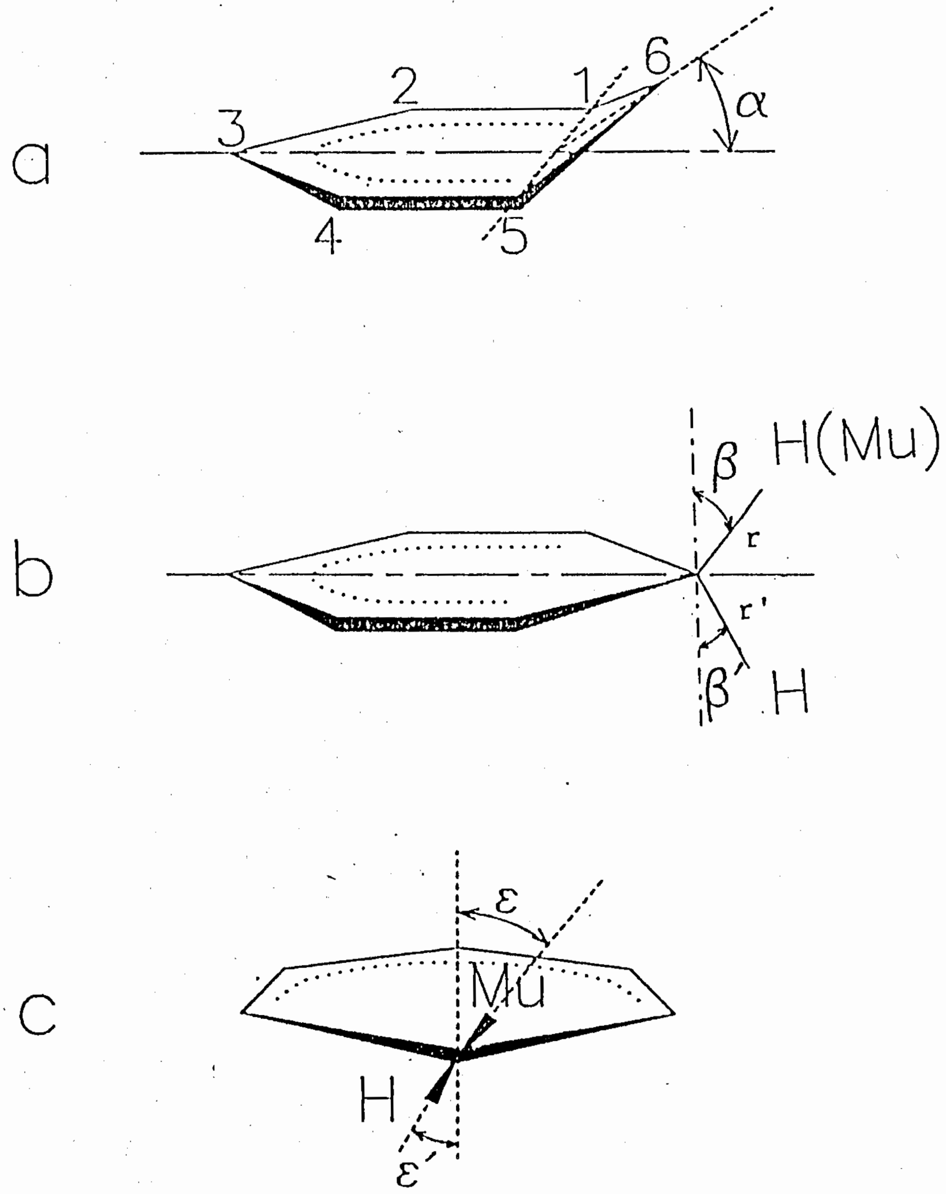

Figure 6-1: Definition of the ring positions and notation for muonium-substituted cyclohexadienyl radicals.

related the hfcc of the methylene protons to the angle β (figure 6-1b) formed by methylene C-H and a normal to the plane of the ring as:

$$A(\beta) = (\rho_1^{\frac{1}{2}} + \rho_5^{\frac{1}{2}})^2(L + M\cos^2\beta)$$

$$= 4\rho_1(L + M\cos^2\beta) \qquad (6.1)$$

where ρ_i is the π spin density on carbon i. L and M have similar meanings to those for alkyl radicals discussed in chapter 5.

The distribution of unpaired spin density ρ in the planar ring can be estimated by using the McConnell's relation [125]:

$$A_{H(i)} = Q_H\rho_i \qquad (6.2)$$

where $A_{H(i)}$ are the proton coupling constants and the proportionality constant Q_H contains several contributions and is usually given an empirical value.

The ^{13}C hfcc can be related to spin density by the Karplus-Fraenkel equation [124]. For cyclohexadienyl it takes the form:

$$A_{C(j)} = Q_j\rho_j + Q_i\rho_i + Q_k\rho_k, \qquad Q_j>0,\ Q_i,Q_k<0 \qquad (6.3)$$

where i and k label the carbons adjacent to C(j). The Q's have similar meaning to that in equation (6.2). They depend on spin polarization of the electrons between a given carbon and its bonded neighbours.

Experimental and theoretical studies [126,128,129] confirm that the equilibrium structure of C_6H_7 has a planar ring. The temperature dependence of methylene hfcc has been interpreted in terms of out-of-plane vibration, characterized by variation of angle α in figure 6-1a. The H(6) coupling in C_6H_7 itself falls with temperature, but the opposite is true for some substituted cyclohexadienyls [126,129], consistent with a non-planar structure in which the single methylene H takes the equatorial position. An alternative suggestion, which is not explicitly discussed in the literature, is that C(6) remains coplanar with the ring and the hfcc temperature dependence arises from a C-H bending mode, *e.g.* variation of the angle β or ϵ (defined in figure 6-1c).

Muonium-substituted cyclohexadienyl radicals were among the first radicals to be detected by μSR [11,113] and μLCR [14,103] spectroscopy. Percival *et al* [103] demonstrated the use of the μLCR technique to study the intramolecular motion and the isotope effect in cyclohexadienyl radicals. Measurements of Mu and X(6) hfcc for C_6H_6Mu, C_6D_6Mu, and C_6F_6Mu at room temperature were reported [14,103]. This chapter describes the extension of this work, specifically the study of the temperature dependence of Mu, H, D, F and ^{13}C hfcc in C_6H_6Mu, C_6D_6Mu, C_6F_6Mu and $^{13}C_6H_6Mu$. Since ^{13}C hfcc have not been measured for C_6H_7, this study provides novel information on motion of the carbon skeleton in this radical. Various MINDO/3 and INDO [130] calculations on some of the radicals were also carried out. A new fit procedure was developed for the temperature dependence of hfcc introduced by vibrational motion.

6.2. The initial measurement of the ^{13}C hfcc of $^{13}C_6H_6Mu$ [131]

The experiments were performed at TRIUMF, using apparatus and techniques described in chapter two. A pure liquid sample of C_6H_6 was used for muon hfcc measurements. For $^{13}C_6H_6Mu$, a dilute solution, 30 mM $^{13}C_6H_6$, 99% enriched, in cyclohexane, was used in order to reduce the amount of $^{13}C_6H_6$ required. Previous study has shown that about 30% of the muons thermalize as muonium in cyclohexane and that the rate constant for muonium addition to benzene is about 4×10^9 $M^{-1}s^{-1}$ [132]. Thus the estimated average lifetime of muonium in the target before the addition reaction to give $^{13}C_6H_6Mu$ is about 8 ns, which is much shorter than the muon lifetime (2.2 μs) and therefore suitable for μLCR spectroscopy. It was not possible to measure the muon hfcc by transverse field μSR experiments on this sample, since the formation time of the radical in the dilute solution was too long to observe coherent muon spin precession. Therefore, for

A_μ, the values from the pure C_6H_6Mu measurements under identical conditions were used, after accounting for the solvent shift. From the μLCR spectrum of $^{13}C_6H_6Mu$, the position of the H(6) resonance was found to be shifted by -0.41% relative to muonium cyclohexadienyl in neat benzene. Assuming that the percentage shifts in the hfcc for the methylene proton and the muon at ring position 6 are equal, then from the leading term in equation (1.16), the shift in the muon hfcc is also approximately equal to -0.41%.

Figure 6-2 shows part of the μLCR spectrum for $^{13}C_6H_6Mu$ at room temperature. All eight of the expected μLCRs were observed — four proton and four ^{13}C. The ^{13}C hfcc with the same sign as that of the muon were attributed to $^{13}C(3)$ and $^{13}C(1,5)$, and the two of opposite sign to $^{13}C(6)$ and $^{13}C(2,4)$. This assignment can be checked by using Karplus-Fraenkel theory [124] and McConnell's relation [125]. The spin densities of the carbon atoms can be estimated from equation (6.2). Using an empirical value of Q_H = -75.7 MHz [133], the spin densities were determined to be $\rho_1 = 0.33$, $\rho_2 = -0.10$ and $\rho_3 = 0.48$. With these spin densities and estimated values of Q (Q_j = 99.8 MHz and $Q_i = Q_k$ = -39.0 MHz [124]), A_C were determined from equation (6.3). The experimental results are collected in table 6-1 together with the Karplus-Fraenkel predictions and an *ab initio* calculation [134].

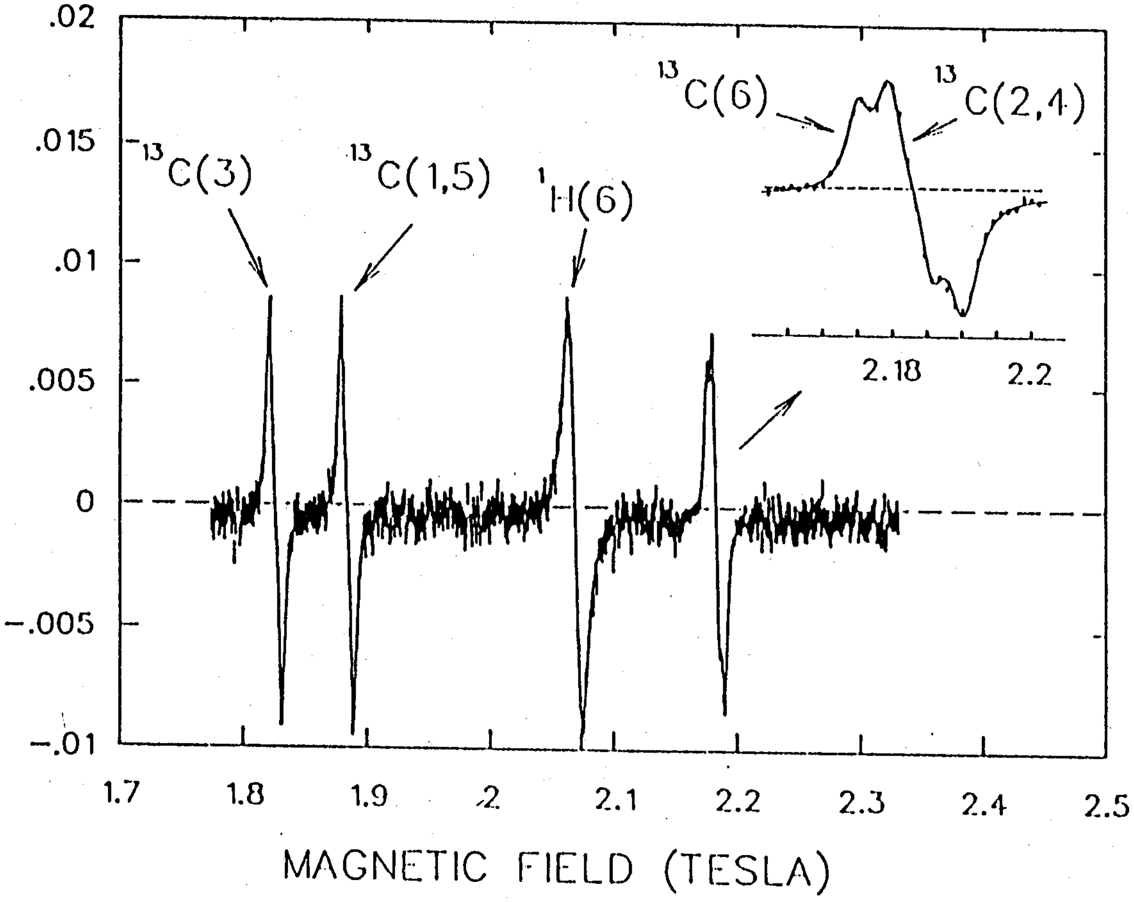

Figure 6-2: Part of the μLCR spectrum for the $^{13}C_6H_6Mu$ radical in cyclohexane at 300 K. The inset shows that two of the ^{13}C resonances are close but still resolved. Three additional proton resonances were observed but are off scale.

Table 6-1

Comparison of measured hfcc (in MHz) for $^{13}C_6H_6Mu$ with an *ab initio* calculation, and a Karplus-Fraenkel treatment

Nucleus	This work	ab initio [134]	Karplus-Fraenkel theory
$^{13}C(1,5)$	39.57(10)	71	36.8
$^{13}C(2,4)$	-35.21(10)	-65	-41.6
$^{13}C(3)$	53.95(10)	69	55.7
$^{13}C(6)$	-34.08(10)	-44	
H(1,5)	-25.00(10)	-36	
H(2,4)	7.89(20)	27	
H(3)	-36.08(10)	-33	
H(6)	125.50(10)	99	

The remaining ambiguities can be removed with a high degree of certainty by comparing the line widths. The resonance lineshape is sensitive to the spin and number of equivalent nuclei which are on resonance. The Lorentzian line shape of μLCR has a width approximately equal to $2[\nu_r^2+1/(2\pi\tau_\mu)^2]^{\frac{1}{2}}/(\gamma_\mu-\gamma_n)$, where ν_r is the resonance frequency. The $^{13}C(2,4)$ and $^{13}C(1,5)$ resonances involve two equivalent nuclei and the $^{13}C(6)$ and $^{13}C(3)$ resonances involve a single nucleus each. The measured line widths for these resonances were 168.0, 136.6, 161.6 and 109.5 MHz. The ratio of the line widths, as assigned, $\Delta B(3)/\Delta B(1,5) = 1.04$ and $\Delta B(2,4)/\Delta B(6) = 1.24$, are in good agreement with the theoretical predictions of 1.00 and 1.38. If the assignments were reversed, the predicted ratios would be 0.53 and 0.76, which are incompatible with the experimental results.

6.3. Hyperfine coupling constants of Mu, H and D in C_6H_6Mu and C_6D_6Mu

6.3.1. Experimental results

The muon hfcc measured from μSR experiments for C_6H_6Mu and C_6D_6Mu at different temperatures are collected in table 6-2. The corresponding μLCR fields and hfcc of X(6) are listed in table 6-3. In these tables, A' stands for the hfcc scaled by the ratio of the nuclear gyromagnetic ratio to that of the proton. The errors reported are statistical errors only. The least-squares

Table 6-2

Muon hfcc of C_6H_6Mu and C_6D_6Mu

Radical	Temp./K	A_μ/MHz	A'_μ/MHz
C_6H_6Mu	10.7	515.519(14)	161.940(4)
	25.1	514.409(13)	161.591(4)
	39.5	513.254(13)	161.228(4)
	54.4	512.115(13)	160.871(4)
C_6D_6Mu	10.7	520.921(19)	163.624(6)
	25.1	519.656(20)	163.240(6)
	39.6	518.479(25)	162.870(6)
	54.1	517.304(20)	162.501(6)

Table 6-3

μLCR fields and hfcc of X(6) in C_6H_6Mu and C_6D_6Mu

Radical	Temp./K	B_0/kG[1]	A_X/MHz	A'_X/MHz
C_6H_6Mu	11.0	20.821	126.26(2)	
	25.2	20.773	126.04(2)	
	39.7	20.721	125.89(2)	
	54.0	20.821	125.73(2)	
C_6D_6Mu	11.1	19.365	18.77(2)	122.3
	25.2	19.320	18.72(2)	122.0
	39.7	19.272	18.73(3)	122.0
	54.3	19.227	18.76(2)	122.2

[1] the uncertainty on B_0 is less than 1 unit of final digit

fits of a straight line show the steepest temperature gradient for Mu (-0.025 MHz/°C), then for H (-0.012 MHz/°C) and the least for D (-0.000 MHz/°C), as shown in figure 6-3. All the experimental results at room temperature agree well with previous measurements and literature values [103].

6.3.2. Theoretical treatment and discussion

6.3.2.1. Equilibrium structure of C_6H_6Mu and C_6D_6Mu

Comparing the hf couplings in tables 6-2 and 6-3, it is evident that muonium substitution in the methylene group results in a substantial increase in hf coupling in C_6H_6Mu and C_6D_6Mu over the unsubstituted species after allowance is made for the trivial effect of the different magnetic moments of the muon, proton and deuteron. This may be explained [128] in terms of out-of-plane deformation of the C(6)X(6)Mu group (described by α in figure 6-1a) in the equilibrium structure; the magnitudes of the methylene hf couplings are related to the extent of interaction of the ring π system with the C-H σ bonds at C(6). Based on the out-of-plane equilibrium structure, Kira *et al* argued [129] that the axial nuclei should have a negative temperature coefficient and the opposite for the equatorial ones. This argument implies that both methylene couplings having negative temperature gradients is evidence for a planar configuration [126,128,129,135]. Furthermore, if the out-of-plane structure were true, a significant change in the

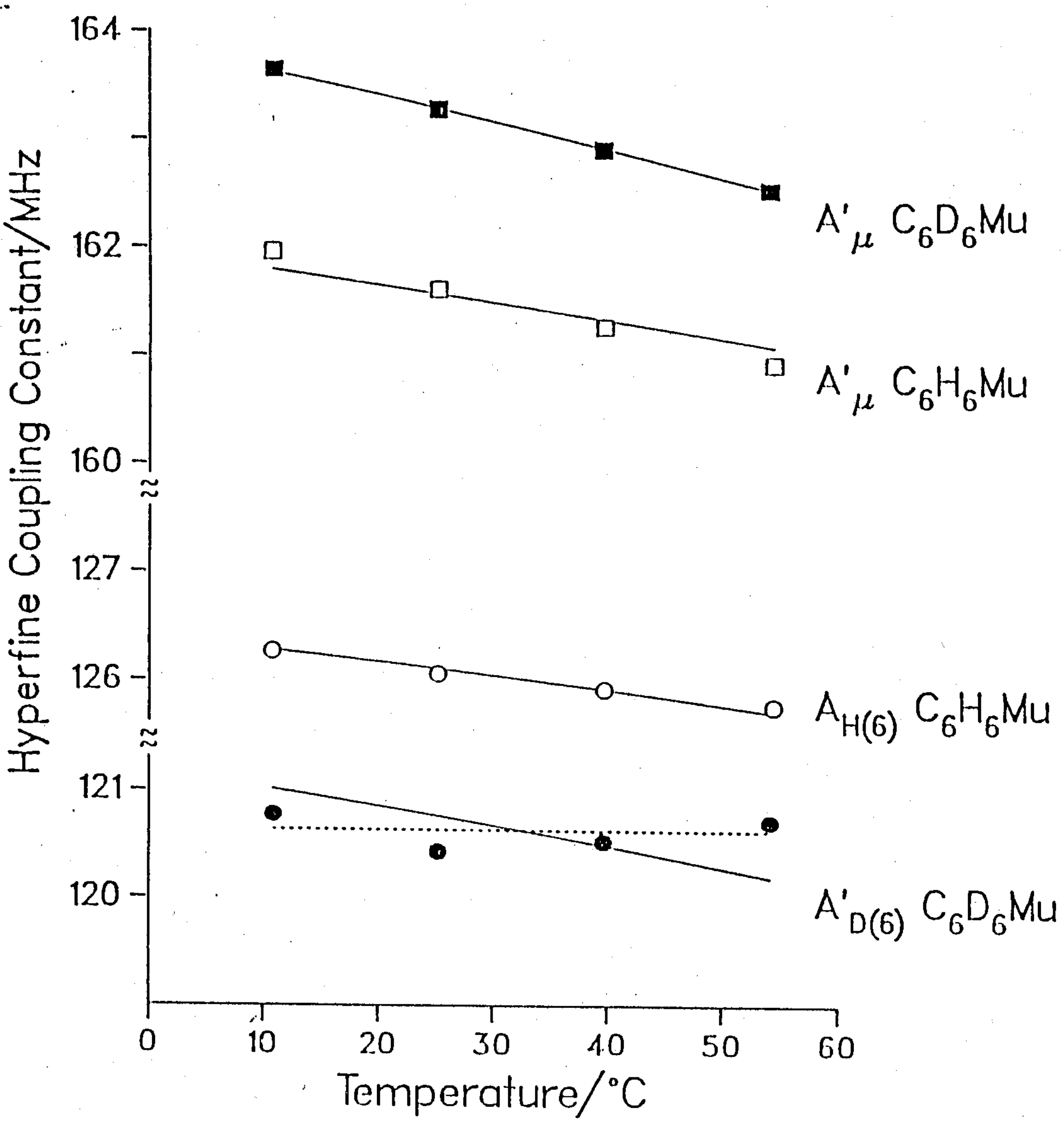

Figure 6-3: Temperature dependence of hfcc for Mu, H and D in C_6H_6Mu and C_6D_6Mu. The muon and deuteron hfcc have been scaled by the appropriate ratio of magnetic moments to make them directly comparable to the proton couplings. Note the broken axis. The solid line through the points represents the best fit of the theoretical model. The dotted line represents the least-squares straight-line fit to the deuteron hfcc.

$^{13}C(1,5)$ hfcc with temperature is expected, since the proportion of s and p orbitals in the hybridization will change with the amplitude of out-of-plane deformation, which is related to temperature. No such changes were found, as will be discussed in section 6.4. All these factors suggest that muonium-substituted cyclohexadienyl radicals have planar or very close to planar structures at equilibrium.

As mentioned in section 6.2., the estimated ρ_1 equals 0.33, ρ_2 equals -0.10 and ρ_3 equals 0.48 for $^{13}C_6H_6Mu$. The remaining spin density (0.06) is located in the antisymmetric methylene group orbital. These results apply to C_6D_6Mu and C_6H_7 as well as C_6H_6Mu, since the ring proton hfcc are so similar. Of course, the precise values of ρ's depend on the choice of Q_H, but there is little doubt as to the qualitative shape of the spin distribution, and there is strong support from semi-empirical molecular orbital calculations [113]. The lack of a significant isotope effect on the spin distribution suggests that the differences in magnitude and temperature gradient of the methylene hfcc are mostly due to local effects as will be discussed in the following sections.

6.3.2.2. Enhanced hyperconjugation from muonium-substitution

One of the local effects on hfcc in the methylene group is the enhanced hyperconjugation as discussed in chapter five. This is caused by the effectively longer C-Mu bond than that of C-H.

Roduner [113] carried out MNDO calculations on C_6H_7 with one methylene bond length fixed at a value 4.9% longer than for the optimized structure. The hfcc were obtained from an INDO calculation based on the new MNDO geometry. His results show isotope effects of +25.1% (Mu) and -4.9% (H) relative to the hfcc of C_6H_7, in reasonable agreement to the experimental observations (+20.5% and -5.9%) [103].

Similar calculations were also carried out in this study. Various MINDO/3 optimized geometries were obtained with one of the C(6)-H bonds (defined as r in figure 6-1b) fixed at different values larger than those of another C(6)-H bond (defined as r' in figure 6-1b). From these "conditional optimized structures" hfcc were calculated using INDO.

Using the equilibrium structure of C_6H_7, as shown in figure 6-4, the INDO hfcc of the methylene protons was determined to be 217.0 MHz. At $r = 1.044\ r'$, the ratio of the two methylene proton hfcc is 1.28, which equals that for experimental measurements on C_6H_6Mu at 25 ^{0}C. Similarly, r is increased by 4.9% in C_6D_6Mu. The results agree well with those of Roduner [113]. The calculated hfcc from INDO for C_6H_7, C_6H_6Mu and C_6D_6Mu are collected in table 6-4.

Compared with the experimental hfcc, the MINDO/3 and INDO predictions are 60% high for methylene proton and muon couplings. Although the ortho and para proton couplings agree

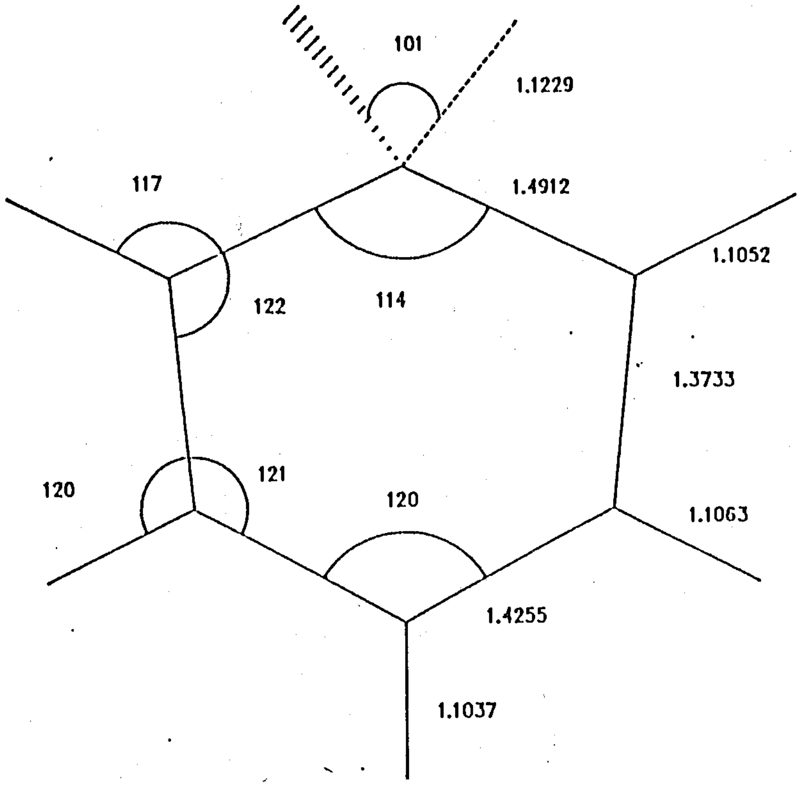

Figure 6-4: MINDO/3 structure of C_6H_7, bond lengths in Å and angles in degree.

Table 6-4

Hfcc (in MHz) of C_6H_7, C_6H_6Mu and C_6D_6Mu from INDO calculations

nucleus	C_6H_7	C_6H_6Mu	C_6D_6Mu
X(1,5)	-29.25	-29.29	-29.30
X(2,4)	15.31	15.17	15.16
X(3)	-33.24	-32.69	-32.59
X(6)	217.0	208.7	207.9
Mu		267.9	276.5

with experiment to within 10%, the meta proton coupling is a factor of two too large. The latter seems to be a general result of INDO for protons adjacent to carbon atoms carrying negative spin population [136].

6.3.2.3. Bending motion of the methylene group

The above discussion shows that the methylene bond stretch accounts for the hf isotope effect. It is desirable to explore the consequences of the bending modes, in particular the "wagging" of the methylene group (defined by changes in β, see figure 6-1b). This motion may affect the temperature gradients of the hfcc in the methylene group. The extent will depend on the differences of zero-point energy and the degree of bending vibration, both of which are isotope dependent. A thorough study of this motion was carried out using MINDO/3 and INDO. The potential energy along β was found to be rather shallow as shown in table 6-5 and figure 6-5. The potential can be described well by $V(x) = \frac{1}{2}kx^2 + k'x^3$ ($x = \beta-\beta_0$ and β_0 is the value of β at the potential minimum) with $k = 304.2$ kJ mol^{-1} and $k' = -101.8$ kJ mol^{-1}. As there is no isotope dependence in MINDO/3 calculations, k and k' are the same for C_6H_7, C_6H_6Mu and C_6D_6Mu.

As in the case of alkyl radicals, separability between the β motion and others was assumed. Using the above V(x) as the potential energy function, the Hamiltonian is:

Table 6-5

Energy profile along β for C_6H_7

x/degree	V(x)/kJ mol^{-1}	
	MINDO/3	$\frac{1}{2}kx^2+k'x^3$
-21.9	27.43	27.91
-17.9	18.78	17.95
-14.1	11.78	10.73
-10.3	6.42	5.51
-6.7	2.69	2.24
-3.1	0.57	0.46
0.0	0.00	0.00
4.3	0.57	0.81
9.3	2.69	3.57
14.3	6.42	7.89
19.3	11.78	13.37
24.3	18.78	19.59
29.3	27.43	26.16

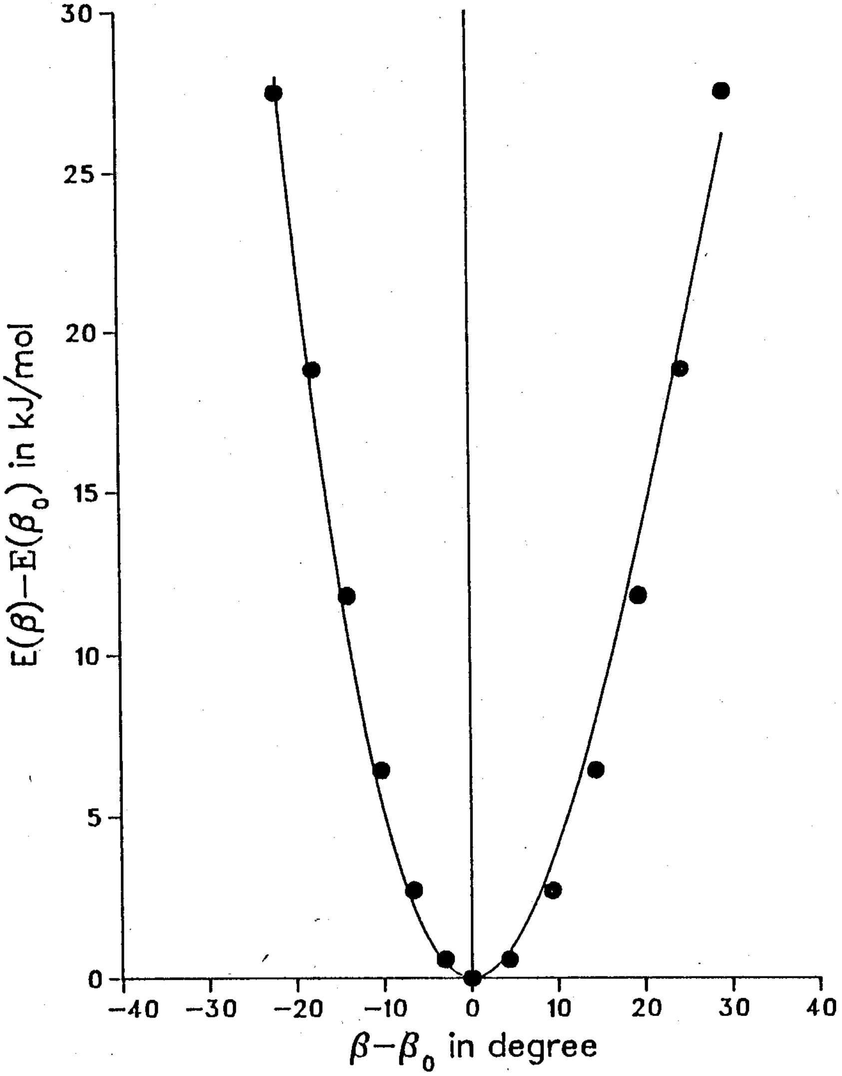

Figure 6-5: Relative energy as a function of $x = \beta-\beta_0$ for C_6H_7, circles are MINDO/3 calculated values and the solid line is an anharmonic potential.

$$H(x) = -(\hbar^2/2I)d^2/dx^2 + \tfrac{1}{2}kx^2 + k'x^3 \qquad (6.4)$$

where I is the reduced moment of inertia of the methylene group for rotation about C(6). As the moment of inertia for the ring (I_1) is much larger than the moment of inertia of the methylene group (I_2), I_2 was used as an approximation for I. From MINDO/3 geometries, I equals 2.37×10^{-47} kgm^2 for C_6H_6Mu and 4.47×10^{-47} kgm^2 for C_6D_6Mu.

Equation (6.1) relates the muon and methylene proton hfcc to angle β. Similarly to the treatment of alkyl radicals in chapter 5, the hfcc of each vibrational state is determined by:

$$A_n = 4\rho_1(L + M\langle n|\cos^2(\beta_0+x)|n\rangle) \qquad (6.5)$$

The β_0's needed for equation (6.5) were calculated using MINDO/3. β_0 equals 41.5° for H(6) and 37.9° for Mu in C_6H_6Mu; β_0 equals 41.7° for D(6) and 37.8° for Mu in C_6D_6Mu. L and M were taken as variable fit parameters.

The observed hfcc were calculated as the Boltzmann-weighted average over vibrational energy levels E_n:

$$A(T) = \sum_n A_n \exp(-E_n/kT)/\sum_n \exp(-E_n/kT) \qquad (6.6)$$

To calculate A(T), the vibrational eigenstates were chosen as linear combinations of harmonic oscillators:

$$|n\rangle = \sum_i c_{in}\phi_i(x) \tag{6.7}$$

with

$$\phi_i(x) = N_i H_i(px)\exp(-p^2x^2/2) \tag{6.8}$$

where H_i are the Hermite polynomials and $p^4 = Ik/\hbar^2$. Constructing the Hamiltonian matrix over the basis set:

$$h_{mn} = \langle\phi_m|H(x)|\phi_n\rangle \tag{6.9}$$

c_{in} (hence $|n\rangle$) and E_n were obtained by diagonalizing the **H** matrix. They were then used to calculate A(T) through equations (6.5) and (6.6). The calculated values of hfcc A(T) were used to fit the experimental results by optimizing $4\rho_1$L and $4\rho_1$M. Table 6-6 reports the fitted L and M. The hfcc calculated from the fits are listed in tables 6-7 and 6-8 (also plotted in figure 6-3 for comparison with the experimental values).

Given that $4\rho_1 = 1.33$, according to the estimate of the unpaired spin distribution, the fit parameters seem reasonable. For example, L = 20.2 MHz and M = 142.7 MHz for H in C_6H_6Mu. The

Table 6-6

L and M values from INDO calculations and fits

radical	nucleus	$4\rho_1 L$/MHz		$4\rho_1 M$/MHz	
		INDO	Fits	INDO	Fits
C_6H_6Mu	H	16.5	26.9	191.1	190.3
	Mu	26.1	29.2	225.4	228.3
C_6D_6Mu	D	16.0	26.9[1]	184.8	181.9
	Mu	26.4	28.5	226.1	229.1

[1] parameter fixed

Table 6-7

Fitted hfcc of Mu and H(6) for C_6H_6Mu

Temp./C	Experimental	Calculated
	A'_μ/MHz	A'_μ/MHz
10.7	161.942	161.782
25.1	161.594	161.553
39.5	161.231	161.299
54.4	160.875	161.031
	A_p/MHz	A_p/MHz
11.0	126.26	126.27
25.2	126.04	126.09
39.7	125.89	125.89
54.0	125.73	125.67

Table 6-8

Fitted hfcc of Mu and D(6) for C_6D_6Mu

Temp./C	Experimental	Calculated
	A'_μ/MHz	A'_μ/MHz
10.7	163.624	163.599
25.1	163.240	163.248
39.6	162.870	162.881
54.1	162.501	162.498
	A'_d/MHz	A'_d/MHz
11.1	122.3	122.5
25.2	122.0	122.2
39.7	122.0	122.0
54.3	122.2	121.7

Mu values are larger than those of H, in keeping with the longer C-Mu bond and as found in the study of t-butyl in chapter 5.

From table 6-8 and figure 6-3, it can be seen that the temperature dependence of hfcc of the D(6) has scattered data. The best fit value of M was obtained by fixing L at the same value found for H. One contributing factor for the scatter is that the gyromagnetic ratio for the deuteron is less by a factor of 7 than that of the proton. A small error in the deuteron hfcc will produce a large error in the scaled hfcc.

For comparison, L and M were also derived by calculating the hfcc (from INDO) at different values of β for C_6H_6Mu and C_6D_6Mu. The hfcc calculated from INDO were scaled by reproducing the experimental hfcc at room temperature. Using the scaled hfcc and equation (6.1), values of $4\rho_1L$ and $4\rho_1M$ could easily be determined. The results are also reported in table 6-6 for comparison with those from the fits.

6.4. Temperature dependence of ^{13}C hfcc in $^{13}C_6H_6Mu$

6.4.1. Results

The μLCR fields and hfcc of ^{13}C in $^{13}C_6H_6Mu$ at four temperature points are reported in table 6-9. As shown in figure 6-6, no temperature dependence was found for the hfcc of C(1,5) and C(3), and a negative temperature dependence for C(2,4) and C(6). A straight-line least-squares fit gave temperature

Table 6-9

μLCR fields and ^{13}C hfcc in $^{13}C_6H_6Mu$

Nuclei	Temp./K	B_0/kG	A_C/MHz
C(6)	10.8	21.834(3)	-33.87(8)
	25.2	21.796(3)	-34.05(8)
	39.5	21.760(2)	-34.25(6)
	54.0	21.719(2)	-34.34(7)
C(2,4)	10.8	21.877(4)	-34.95(9)
	25.2	21.842(3)	-35.19(7)
	39.5	21.806(2)	-35.38(5)
	54.0	21.719(3)	-35.47(7)
C(3)	10.5	18.303(7)	53.91(3)
	25.2	18.262(8)	53.81(3)
	39.8	18.219(7)	53.73(3)
	54.0	18.173(8)	53.78(3)
C(1,5)	10.5	18.883(8)	39.50(3)
	25.2	18.841(8)	39.42(3)
	39.8	18.799(8)	39.32(3)
	54.0	18.752(8)	39.41(4)

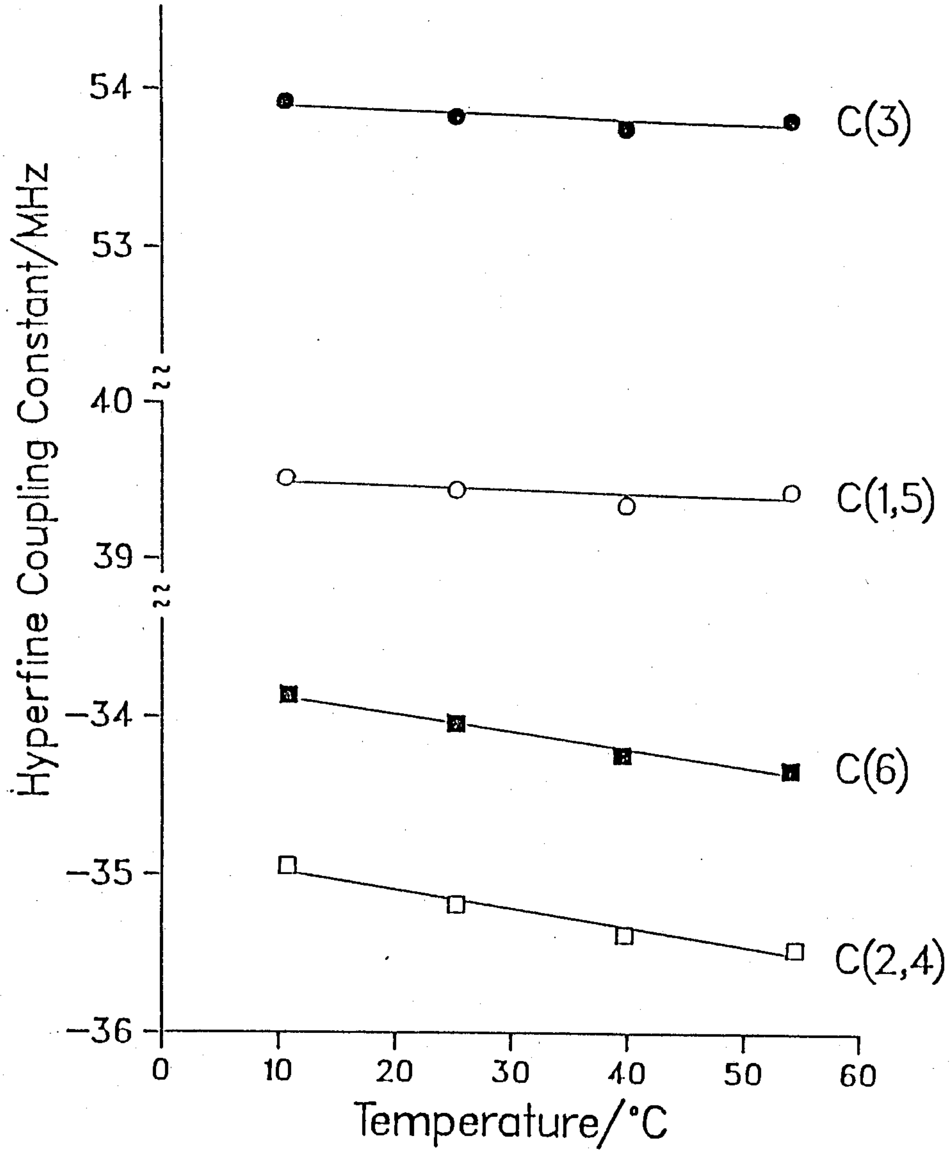

Figure 6-6: Temperature dependence of ^{13}C hfcc in $^{13}C_6H_6Mu$. The points represent experimental results and the straight lines are the best fits to the experimental values.

gradients of -0.010 and -0.011 MHz/°C for C(6) and C(2,4) respectively.

Table 6-10 collects the hfcc from MINDO/3 and INDO calculations. Compared with the experimental results, the calculated ^{13}C hfcc are 50% high for the methylene carbon. For ortho, para and meta carbons the calculated hfcc agree with experiment to about 10%.

6.4.2. Discussion

In principle, temperature dependence of the ^{13}C hfcc should be a good indication of vibrational motion involving the carbon skeleton. However there are two complications. First, the ^{13}C hfcc are sensitive to spin densities on adjacent atoms as well as the carbon under consideration. This is particularly relevant to conjugated systems where there is appreciable distribution of the unpaired spin density, as described by the Karplus-Fraenkel theory. For some purposes it is reasonable to consider that most of the spin density is confined to carbon 1, 3 and 5. Accordingly, the hfcc for C(1,5) and C(6) depend principally on ρ_1 alone. However, while this simplification may give reasonable estimates of the magnitude of the hfcc it is inadequate to describe the temperature dependence, because the minor spin densities may be critical in determining the small differences in hfcc with motion. In particular, the C(1,5) and C(6) coupling constants may depend on the spin density in the methylene group

Table 6-10

^{13}C hfcc (in MHz) of C_6H_7, C_6H_6Mu and C_6D_6Mu from INDO

nucleus	C_6H_7	C_6H_6Mu	C_6D_6Mu
$^{13}C(1,5)$	48.75	48.57	48.57
$^{13}C(2,4)$	-37.81	-37.73	-37.72
$^{13}C(3)$	59.80	58.81	58.63
$^{13}C(6)$	-47.87	-51.74	-52.46

orbital, and it is very difficult to incorporate this in the Karplus-Fraenkel equation. This brings one to the second consideration: not only does the spin density distribution change with intramolecular motion, so too do the Q's, as they depend on the degree of hybridization of each carbon.

Having come to the conclusion that there is no simple way to predict the temperature dependence of the ^{13}C hfcc, the effect of various types of motion using MINDO and INDO were explored. Out-of-plane bending (variation of α in figure 6-1a) predicted positive temperature gradients for C(6), C(3) and C(1,5) and a negative one for C(2,4); methylene wagging (variation of β, see figure 6-1b) predicted positive temperature gradients for C(6), C(2,4) and C(1,5) and a negative one for C(3). Both these motions are inconsistent with the experimental findings. The motions which result in significant decrease in the C(6) hfcc are the methylene C-Mu and C-H stretches and twisting of this group about the C(3)-C(6) axis (described by ϵ in figure 6-1c). The high vibrational frequencies of C-Mu and C-H stretches preclude significant contribution from these motions to the observed hfcc temperature gradient of C(6). The variations of the hfcc as a function of ϵ and ϵ' for Mu or H(6) are presented in table 6-11. Both of the functions were fitted to a polynomial yielding (a) hfcc(MHz) = $-51.74 - 10.53\epsilon^2$ and (b) hfcc(MHz) = $-51.74 - 14.74\epsilon'^2$ for Mu and H(6) respectively. The observed hfcc should be the Boltzmann average of the hfcc on the

Table 6-11

hfcc (in MHz) of C(6) for $^{13}C_6H_6Mu$ as functions of ϵ and ϵ'

ϵ/degree	$A_{C(6)}$	ϵ'/degree	$A_{C(6)}$
-15	-52.75	-15	-52.47
-10	-52.22	-10	-52.08
- 5	-51.86	- 5	-51.83
0	-51.74	0	-51.74
5	-51.86	5	-51.83
10	-52.22	10	-52.08
15	-52.75	15	-52.47

vibrational states. From (a) and (b) the temperature gradients were calculated to be 0.012 MHz/^{0}C and 0.013 MHz/^{0}C, respectively. Each of them alone is comparable with the experimental observation, where the gradient of hfcc of C(6) was 0.011 MHz/^{0}C. This may just be an coincidence. The real situation is more complicated as both ϵ and ϵ' motions will contribute to the temperature gradients as well as some other motions.

6.5. C_6F_6Mu

The muon and F(6) hfcc of C_6F_6Mu were determined at several temperatures as shown in tables 6-12 and 6-13 and figure 6-7.

Lusztyk and Ingold found [135] negative temperature gradients for both the F(6) and H hfcc in C_6F_6H. Based on a similar argument to Kira [126], they claimed that the radical is planar. Negative temperature gradients are also found for Mu and F(6) in C_6F_6Mu. This can be take as an evidence that the C_6F_6Mu also has a planar ring structure. The larger hfcc for F(6) than Mu may be attributed to a decrease in the energy of the methylene psuedo-π orbital caused by the electron-withdrawing character of fluorine which makes the hyperconjugation less efficient. The temperature gradients were found to be -0.14 and -0.0026 MHz/degree for F(6) and H in C_6F_6H [135]. For C_6F_6Mu, the temperature gradient for F(6) (-0.10 MHz/degree) is also found to be larger than that of Mu (-0.0072 MHz/degree). This

Table 6-12

Muon hfcc of C_6F_6Mu

Temp./K	A_μ/MHz	A'_μ/MHz
12.4	201.03(4)	63.15(1)
25.0	200.91(4)	63.12(1)
37.2	200.87(5)	63.10(2)
50.5	200.74(5)	63.06(2)

Table 6-13

μLCR fields and hfcc of F(6) in C_6F_6Mu

Temp./K	B_0/kG	A_x/MHz
12.4	8.4820	361.02(1)
25.0	8.4206	359.78(1)
37.2	8.3597	358.57(1)
50.5	8.2916	357.18(1)

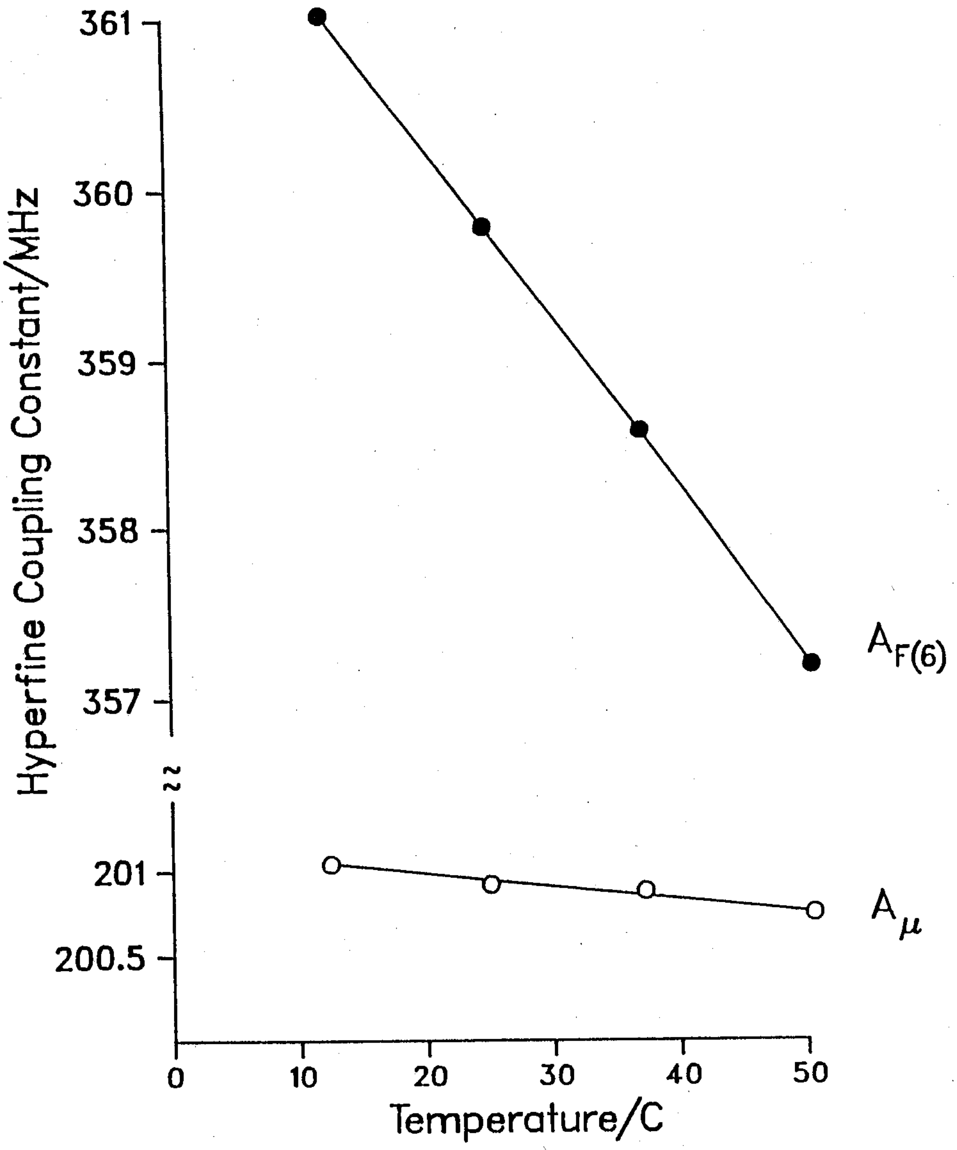

Figure 6-7: Temperature dependence of hfcc of Mu and F(6) in C_6F_6Mu. The points depict experimental results and the lines are best fits of straight lines to the experimental values.

can be seen clearly in figure 6-7.

6.6. Summary

The experimental results and the calculations show that the increased bond length of C-Mu provides the key role for the isotope shifts in hfcc of muonium-substituted cyclohexadienyl radicals. An out-of-plane equilibrium conformation is not supported by the analysis, nor does this type of vibrational distortion account for the measured temperature gradients of the ^{13}C hfcc. Instead, it is found that the variations of the methylene proton and carbon hfcc are consistent with bending modes within the methylene group, without significant distortion of ring planarity.

CHAPTER SEVEN

Summary

As a light isotope of hydrogen, muonium has been used as a probe in kinetic studies since the early days of muonium chemistry. The first pressure-dependent kinetics study, as reported in this thesis, again shows that μSR is a powerful and convenient technique. The results are comparable to those of hydrogen atom reactions and also provide new information relevant to theoretical studies of the effective size of hydrogen and muonium atoms in water.

The large mass difference between Mu and ^1H (compared with other ^1H isotopes) makes muonium ideal for studying kinetic isotope effects. Experimentally, various degrees of kinetic isotope effects have been obtained compared with the corresponding ^1H data, but little has been done on theoretical aspects. As exploratory work, the semiempirical calculations on the reactions $H + H_2O_2$ and $Mu + H_2O_2$ give an idea of what can be done, what kind of information can be obtained, and what has to be included for high quality theoretical studies in this field. Muon hfcc in muonium-substituted free radicals have been measured from μSR experiments and used to compare with those of hydrogen, to study the isotope effects in hf interactions, since

1978. In many cases this provides much more information than the study of unsubstituted radicals. For example, the hfcc of the methylene group in C_6H_6Mu give information on intramolecular motion not obtainable from C_6H_7 alone. In addition to the study of isotope effects, the μLCR technique makes it possible to use muonium just as a label to study other nuclear hf interactions in muonium-substituted free radicals. Compared with ESR spectroscopy, μLCR has the following major advantages: (1) The position and magnitude of each resonance are insensitive to the number of nuclei off resonance, thus the assignments of μLCR spectra are simple; (2) μLCR is sensitive to the relative signs of the muon hf frequency and that of the coupled nucleus; and (3) in contrast to ESR, the radicals are studied in μLCR at extreme dilution, so that the signals are not affected by radical-radical reactions. This last point was a significant factor in the succesful measurements of ^{13}C hfcc in $^{13}C_6H_6Mu$.

Muonium is an ideal isotope of ^1H for the study of kinetic isotope effects, and μSR and μLCR spectroscopies are powerful tools for the study of organic free radicals.

REFERENCES

1. C. D. Anderson and S. H. Neddermeyer, Phys. Rev. 51 (1937) 884.
2. T. D. Lee and C. N. Yang, Phys. Rev. 104 (1956) 254.
3. A. Schenck, Muon spin rotation spectroscopy; Principle and applications in solid state physics (Hilger, London, 1985).
4. J. I. Friedman and V. L. Telegdi, Phys. Rev. 106 (1957) 1290.
5. D. G. Fleming, D. M. Garner, L. C. Vaz, D. C. Walker, J. H. Brewer and K. M. Crowe, Adv. in Chemistry Series 175 (1979) 279.
6. P. W. Percival, H. Fisher, M. Camani, F. N. Gygax, W. Ruegg, A. Schenck, H. Schilling and H. Graaf, Chem. Phys. Lett. 39 (1976) 333.
7. S. K. Leung, J. C. Brodovitch, K. E. Newman and P. W. Percival, Chem. Phys. 114 (1987) 399.
8. P. W. Percival, Radiochimica Acta 26 (1979) 1.
9. S. F. J. Cox, J. Phys. C 20 (1987) 3187.
10. A. M. Brodskii, Zh. Exp. Teor. Fiz. 44 (1963) 1612.
11. E. Roduner, P. W. Percival, D. G. Fleming, J. Hochman and H. Fisher, Chem. Phys. Lett. 57 (1978) 37.
12. D. C. Walker, Muon and Muonium Chemistry (Cambridge University Press, Cambridge, 1983).
13. A. Abragam, C. R. Acad. Sc. Paris, Serie II 299 (1984) 95.

14. R. F. Kiefl, S. Kreitzman, M. Celio, R. Keitel, G. M. Luke, J. H. Brewer, D. R. Noakes, P. W. Percival, T. Matsuzaki and K. Nishiyama, Phys. Rev. A 34 (1986) 681.

15. M. Heming, E. Roduner and B. D. Patterson, Hyperfine Interactions 32 (1986) 727.

16. D. Yu, Cumulative Examination I, Simon Fraser University, (1986).

17. J. C. Brodovitch, S. K. Leung, P. W. Percival, D. Yu and K. E. Newman, Radiat. Phys. Chem. 32 (1988) 105.

18. P. W. Percival, TRIUMF Research Proposal 398 (1986).

19. QCPE Program No. 309, Quantum Chemistry Program Exchange, Department of Chemistry, Indiana University.

20. V. W. Hughes, Bull. Am. Phys. Soc. II 2 (1957) 205.

21. J. H. Brewer and K. M. Crowe, Ann. Rev. Nucl. Sci. 28 (1978) 239.

22. A. Schenck, in: Nuclear and Particle Physics at Intermediate Energies, ed. J. B. Warren (Plenum Press, New York, 1975).

23. R. L. Garwin, L. M. Lederman and M. Weinrich, Phys. Rev. 105 (1957) 1415.

24. J. H. Brewer, K. M. Crowe, F. N. Gygax and A. Schenck, in: Muon Physics, Vol. 3, ed. V. W. Hughes and C. S. Wu (Academic Press, 1975).

25. D. C. Walker, J. Chem. Phys. 85 (1981) 3960.

26. V. W. Hughes, Ann. Rev. Nucl. Sci. 16 (1966) 445.

27. D. M. Garner, Ph.D. thesis, University of British Columbia (1979).

28. E. Roduner and H. Fischer, Chem. Phys. 54 (1981) 261.

29. J. H. Brewer, D. G. Fleming and P. W. Percival, in: Fourier, Hadamard, and Hilbert Transforms in Chemistry, ed. A. G. Marshall (Plenum Publishing Corporation, 1982).

30. M. Heming, E. Roduner, B. D. Patterson, H. Keller and I. M. Savic, Chem. Phys. Lett. 128 (1986) 100.

31. R. F. Kiefl, Hyperfine Interactions 32 (1986) 707.

32. T. A. Hodges, TRIUMF design note VPN-80-1 (1980).

33. TRIUMF users handbook, TRIUMF (1987).

34. J. L. Beveridge, J. Doornbos, D. M. Garner, D. J. Arseneau, I. D. Reid and M. Senba, Nucl. Instr. and Meth. A240 (1985) 316.

35. A. E. Pifer, T. Bowen and K. R. Kendall, Nucl. Instr. Meth. 135 (1976) 39.

36. J. B. Birks, Theory and practice of scintillation counting (Macmillan, 1964).

37. F. James and M. Roos, MINUIT, CERN Computer. 7600 Interim Program Library.

38. J. A. Nelder and R. Mead, Computer J. 7 (1967) 308.

39. W. C. Davidon, Computer J. 10 (1968) 406.

40. C. F. Dietrich, Uncertainty, Calibration and Probability (John Wiley & Sons, 1973).

41. T. Asano and W. J. Le Noble, Chem. Rev. 78 (1978) 407.

42. R. R. Hentz, Farhataziz, D. J. Milner and M. Burton, J. Chem. Phys. 46 (1967) 2995.

43. R. R. Hentz, Farhataziz and D. J. Milner, J. Chem. Phys. 49 (1968) 2153.

44. R. R. Hentz and C. G. Johnson Jr., J. Chem. Phys. 51 (1969) 1236.

45. R. R. Hentz and D. W. Brazier, J. Chem. Phys. 54 (1971) 2777.

46. Farhataziz, I. Mihalcea, L. J. Sharp and R. R. Hentz, J. Chem. Phys. 59 (1973) 2309.

47. J. S. Tse and M. L. Klein, J. Phys. Chem. 87 (1983) 5055.

48. B. De Raedt, M. Sprik and M. L. Klein, J. Chem. Phys. 80 (1984) 5719.

49. P. W. Percival, E. Roduner, H. Fischer, M. Camani, F. N. Gygax, and A. Schenck, H. Schilling and H. Graaf, Chem. Phys. Lett. 47 (1977) 47.

50. Y. C. Jean, D. G. Fleming, B. W. Ng and D. C. Walker, Chem. Phys. Lett. 91 (1982) 1.

51. P. W. Percival, E. Roduner, and H. Fischer, Adv. in Chem. Series 175 (1979) 335.

52. W. Kolos and L. Wolnieiwicz, Chem. Phys. Lett. 24 (1973) 457.

53. F. Franks, Water, Chapter 9, The Royal Society of Chemistry, London (1983).

54. M. Anbar, Farhataziz and A. B. Ross, Selected specific

rates of reactions of transients from water in aqueous solution. II Hydrogen Atoms, NSRDS-NBS 51 (Washington, 1975).

55. R. B. Klemm, W. A. Payne and L. J. Stief, Int. J. Chem. Kin. Symp. 1 (1975) 61.

56. R. A. Gorse and D. H. Volman, J. Photochem. 3 (1974)

57. J. F. Meagher and J. Heicklen, J. Photochem. 3 (1974/5) 455.

58. P. W. Percival, J. C. Brodovitch and K. E. Newman, NBS special publication 716, NBS, Washington (1986) 547.

59. S. Glasstone, K. J. Laidler and H. Eyring, The theory of rate processes (McGraw-Hill Book Company, Inc., New York 1941).

60. A. Maccoll, Ann. Report on the Progr. of Chem. 71 (1974) 77.

61. J. Bigeleisen, J. Chem. Phys. 17 (1949) 675

62. W. A. Van Hook, in: Isotope effects in chemical reactions, ed. C. J. Collins and N. S. Bowman (Van Nostrand Reinhold Ltd., 1970).

63. L. Melander and W. H. Saunders, Jr., Reaction rates of isotopic molecules, John Wiley & Sons, 1980.

64. O. Redlich, Z. Phys. Chem. B28 (1935) 371.

65. E. B. Wilson, Jr., J. C. Decius and P. C. Cross, Molecular Vibrations, McGraw-Hill, New York, N. Y., 1955.

66. S. Califano, Vibrational States, John Wiley & Sons, 1976.

67. *NAG, FORTRAN library numerical application group.

68. M. J. S. Dewar, J. Mol. Struct. 40 (1975) 145.

69. S. B. Brown, M. J. S. Dewar, G. P. Ford, D. J. Nelson and H. S. Rzepa, J. Am. Chem. Soc. 100 (1978) 7832.

70. J. H. Espenson, Chemical kinetics and reaction mechanism (McGraw-Hill, 1981).

71. C. Eckart, Phys. Rev. 35 (1930) 1303.

72. M. S. Child, in: Modern Gas Kinetics — Theory, Experiment and Application, ed. M. J. Pilling and I. W. M. Smith (Blackwell Scientific Publications, 1987).

73. B. C. Garrett, D. G. Truhlar and R. S. Grev, in: Potential Energy Surfaces and Dynamical Calculations, ed. D. G. Truhlar (Plenum Press, New York, 1981).

74. J. A. Pople and D. L. Beveridge, Approximate Molecular Orbital Theory, McGraw-Hill, 1970.

75. R. Daudel, G. Leroy, D. Peeters and M. Sana, Quantum Chemistry (John Wiley & Sons, 1983).

76. D. R. Hartree, Proc. Cambridge Phil. Soc. 24 (1928) 89.

77. V. Fock, Z. Physik 61 (1930) 126.

78. C. C. J. Roothaan, Rev. Mod. Phys. 23 (1951) 69.

79. J. A. Pople, D. L. Beveridge and P. A. Dobosh, J. Chem. Phys. 47 (1967) 2026.

80. R. C. Bingham, M. J. S. Dewar and D. H. Lo, J. Am. Chem. Soc. 97 (1975) 1285.

81. R. C. Bingham, M. J. S. Dewar and D. H. Lo, J. Am. Chem.

Soc. 97 (1975) 1294.

82. R. C. Bingham, M. J. S. Dewar and D. H. Lo, J. Am. Chem. Soc. 97 (1975) 1302.

83. R. C. Bingham, M. J. S. Dewar and D. H. Lo, J. Am. Chem. Soc. 97 (1975) 1307.

84. C. Heller and H. J. M. McConnell, J. Chem. Phys. 32 (1960) 1535.

85. R. W. Fessenden, J. Chem. Phys. 61 (1964) 1570.

86. E. Roduner, W. Strub, P. Burkhard, J. Hochmann, P. W. Percival, H. Fischer, M. Ramos and B. C. Webster, Chem. Phys. 67 (1982) 275.

87. S. F. J. Cox, T. A. Claxton and M. C. R. Symons, Radiat Phys. Chem. 28 (1986) 107.

88. M. J. Ramos, D. McKenna, B. C. Webster and E. Roduner, J. Chem. Soc. Faraday Trans. I, 80 (1984) 255.

89. M. J. Ramos, D. McKenna, B. C. Webster and E. Roduner, J. Chem. Soc. Faraday Trans. I, 80 (1984) 267.

90. J. K. Kochi, in: Advances in free-radical chemistry, vol. 5, ed. G. H. Williams (Academic Press, New York, 1975).

91. M. R. Imam and N. L. Allinger, J. Mol. Struct. 126 (1985) 345.

92. M. N. Paddon-Row and K. N. Houk, J. Phys. Chem. 89 (1985) 3771.

93. M. Yoshimine and J. Pacansky, J. Chem. Phys. 74 (1981) 5168.

94. M. N. Paddon-Row and K. N. Houk, J. Am. Chem. Soc. 103 (1981) 5046.

95. F. A. Houle and J. L. Beauchamp, J. Am. Chem. Soc. 101 (1979) 4067.

96. J. Pacansky and J. S. Chang, J. Chem. Phys. 74 (1981) 5539.

97. J. B. Lisle, L. F. Williams and D. E. Wood, J. Am. Chem. Soc. 98 (1976) 227.

98. D. Griller, K. U. Ingold, P. J. Krusic and H. Fischer, J. Am. Chem. Soc. 100 (1978) 6750.

99. D. E. Wood and R. F. Sprecher, Mol. Phys. 26 (1973) 1311.

100. P. J. Krusic and P. Meakin, J. Am. Chem. Soc. 98 (1976) 228.

101. I. Carmichael, J. Phys. Chem. 89 (1985) 4727.

102. J. Pacansky and M. Yoshimine, J. Phys. Chem. 90 (1986) 1980.

103. P. W. Percival, R. F. Kiefl, S. Kreitzman, D. M. Garner, S. F. J. Cox, G. M. Luke, J. H. Brewer, K. Nishiyama and K. Venkateswaran, Chem. Phys. Lett. 133 (1987) 465.

104. P. J. Krusic, P. Meakin and J. P. Jesson, J. Phys. Chem. 75 (1971) 3438.

105. D. Griller and K. U. Ingold, J. Am. Chem. Soc. 96 (1974) 6203.

106. R. W. Fessenden, J. Phys. Chem. 71 (1967) 74.

107. R. W. Fessenden and R. H. Schuler, J. Chem. Phys. 39 (1963) 2147.

108. E. Roduner and D. M. Garner, Hyperfine Interactions, 32 (1986) 733.

109. C. J. Rhodes and M. C. R. Symons, J. Chem. Soc. Faraday Trans. I 84 (1988) 1187.

110. E. Roduner, in: Muons and pions in materials research, ed. J. Chappert and R. I. Grynszpan (Elsevier, Amsterdam, 1984).

111. T. A. Claxton and A. M. Graham, J. Chem. Soc. Chem. Commun., (1987) 1167.

112. T. A. Claxton and A. M. Graham, J. Chem. Soc. Faraday Trans. II 83 (1987) 2307.

113. E. Roduner, in: Vol. 49 of lecture notes in chemistry (Springer, Heidelberg, 1988).

114. H. Paul and H. Fischer, Helv. Chim. Acta 56 (1973) 1575.

115. J. K. Kochi, J. Am. Chem. Soc. 93 (1971) 846.

116. P. W. Percival, J. C. Brodovitch, S. Leung, D. Yu, R. F. Kiefl, G. M. Luke, K. Venkateswaran and S. F. J. Cox., Chem. Phys. 127 (1988) 137.

117. D. Griller, K. U. Ingold, P. J. Krusic and H. Fischer, J. Am. Chem. Soc. 100 (1978) 6750.

118. R. W. Fessenden and R. H. Schuler, J. Chem. Phys. 38 (1963) 773.

119. W. G. Filby and K. Günther, J. Chem. Phys. 60 (1974) 3355.

120. M. Lefcourt, K. P. Madden and R. H. Schuler, J. Phys. Chem. 89 (1985) 3101.

121. J. P. Colpa and E. de Boer, Mol. Phys. 7 (1964) 333.

122. G. A. Helcke and R. Fantechi, Mol. Phys. 17 (1969) 65.

123. K. Eiben and R. H. Schuler, J. Chem. Phys. 62 (1975) 3093.

124. M. Karplus and G. K. Fraenkel, J. Chem. Phys. 35 (1961) 1312.

125. H. M. McConnell, J. Chem. Phys. 24 (1956) 764.

126. M. Kira, H. Sugiyama and H. Sakurai, J. Am. Chem. Soc. 105 (1983) 6436.

127. D. Whiffen, Mol. Phys. 6 (1963) 223.

128. M. B. Yim and D. E. Wood, J. Am. Chem. Soc. 97 (1975) 1004.

129. M. Kira and H. Sakurai, J. Am. Chem. Soc. 99 (1977) 3892.

130. QCPE Program No. 141, Quantum Chemistry Program Exchange, Department of Chemistry, Indiana University.

131. R. F. Kiefl, P. W. Percival, J. C. Brodovitch, S. K. Leung, D. Yu, K. Venkateswaran and S. F. J. Cox, Chem. Phys. Lett. 143 (1988) 613.

132. P. W. F. Louwrier, G. A. Brinkman and E. Roduner, Hyperfine Interactions 32 (1986) 831.

133. J. E. Wertz and J. R. Bolton, Electron spin resonance: elementary theory and practical applications (McGraw-Hill, New York, 1972).

134. D. M. Chipman, J. Chem. Phys. 78 (1983) 4785.

135. J. Lusztyk and K. U. Ingold, J. Phys. Chem. 89 (1985) 1865.

136. J. C. Walton, Rev. Chem. Intermed. 5 (1984) 249.